NASA Technical Paper 1718

Estimation of Wing Nonlinear Aerodynamic Characteristics at Supersonic Speeds

Harry W. Carlson and Robert J. Mack

NOVEMBER 1980

NASA

NASA Technical Paper 1718

Estimation of Wing Nonlinear Aerodynamic Characteristics at Supersonic Speeds

Harry W. Carlson and Robert J. Mack
Langley Research Center
Hampton, Virginia

National Aeronautics
and Space Administration

**Scientific and Technical
Information Branch**

1980

SUMMARY

A computational system for estimation of nonlinear aerodynamic characteristics of wings at supersonic speeds has been developed and has been incorporated in a computer program. This corrected linearized-theory method accounts for nonlinearities in the variation of basic pressure loadings with local surface slopes, predicts the degree of attainment of theoretical leading-edge thrust forces, and provides an estimate of detached leading-edge vortex loadings that result when the theoretical thrust forces are not fully realized.

Comparisons of estimates given by the present method with experimental results show significant improvements in detailed wing pressure distributions over those given by linearized theory, particularly for large angles of attack and/or for regions of the wing where the flow is highly three-dimensional. The new method also provides generally improved predictions of the wing overall force and moment coefficients. The more accurate prediction of pitching moment and the more realistic estimate of the variation of drag with camber surface severity as dictated by the design lift coefficient are particularly important. This latter capability should prove useful in the conduct of design studies aimed at aerodynamic performance optimization. The new method should also provide more realistic trade-off information for selection of wing planform geometry and airfoil section parameters.

INTRODUCTION

Linearized-theory methods for the aerodynamic design and analysis of supersonic airplane configurations (e.g., refs. 1 to 5) have proven to be very useful in the preliminary stages of aircraft design. They provide realistic estimates of aerodynamic performance for reasonably complete airplane configurations. In addition to the wing, these configurations may include a fuselage, tail or canard surfaces, and nacelles or stores. Design details such as wing twist and camber and aerodynamic interference between configuration components are also taken into account.

Linearized-theory methods, however, are impaired by their inability to account for certain nonlinear effects. One such nonlinearity occurs in regions of the wing (e.g., near the root chord) where the flow tends to be two-dimensional in character. Here, local pressures are not linear functions of the surface slope but tend to behave more in the manner of the variations predicted by two-dimensional shock-expansion theory. Another deficiency of linearized theory occurs in regions of the wing (e.g., near the leading edge and near the tip) where the flow tends to be highly three-dimensional in character. Here, conventional linearized-theory methods fail to account properly for the effect on local pressures of the large lateral velocities. Another nonlinearity is associated with the leading-edge thrust force and with the detached leading-edge vortex flow that develops when leading-edge thrust is not realized.

Often, there are compensating errors in linearized theory, and the failure to account for nonlinearities introduces little error in prediction of lift and drag. However, errors in prediction of pitching moment are common, especially for wings which depart from a delta planform. Additionally, for wings with twist and camber, appreciable errors in prediction of drag due to the surface distortion (camber drag) often occur. In particular, linearized-theory methods fail to indicate the proper selection of camber surface severity, a function of the design lift coefficient, for drag minimization.

This paper presents a corrected linearized-theory computational system intended to provide estimates of wing supersonic aerodynamic characteristics which account for these nonlinear effects. The linearized-theory solution which serves as a framework for the system is based on numerical methods presented in references 1 and 2. Additional work discussed herein has permitted an extension of the original methods to provide lateral as well as longitudinal perturbation velocities. A new pressure-coefficient formulation intended to provide more accurate estimates of detailed pressure loadings for improved stability analysis and analysis of critical structural design conditions was introduced in reference 6. The approach is based on the use of oblique-shock and Prandtl-Meyer expansion relationships for accurate representation of the variation of pressures with surface slopes in two-dimensional flow and of linearized-theory perturbation velocities for evaluation of local three-dimensional aerodynamic interference effects. The method, as presented in reference 6, was designed primarily for high supersonic Mach numbers and large angles of attack. For use in this system, it has been modified slightly to provide a more uniformly valid improvement over linearized theory for low as well as high supersonic Mach numbers and for small as well as large angles of attack. Estimation of the nonlinearities associated with leading-edge thrust and the detached leading-edge vortex flow is based on the method of reference 7 for calculation of theoretical thrust, the method of reference 8 for estimation of the fraction of the theoretical thrust actually attainable, and an improvement on the method of reference 9 for estimation of the vortex-flow induced force.

The assembled computing program is described, and a source for its procurement is given. The applicability and limitations of the system are illustrated by numerous comparisons with experimental data, both for pressure distributions and overall forces and moments.

Use of trade names or names of manufacturers in this report does not constitute an official endorsement of such products or manufacturers, either expressed or implied, by the National Aeronautics and Space Administration.

SYMBOLS

A area of wing element in program units (1.0 for all but leading- and trailing-edge elements); see figure 1

b wing span

C_A axial- or chord-force coefficient

c_a section axial- or chord-force coefficient

C_D drag coefficient

$C_{D,o}$ drag coefficient at zero lift

C_L lift coefficient

$C_{L,D}$ design lift coefficient for a twisted and cambered wing

C_m pitching-moment coefficient

$C_{m,o}$ pitching-moment coefficient at zero lift

C_N normal-force coefficient

c_n section normal-force coefficient

C_p pressure coefficient

C_p^* pressure coefficient given by present method, $C_p^* = C_{p,a}^* + C_{p,v}^*$

$C_{p,a}^*$ pressure coefficient increment due to attached flow

$C_{p,v}^*$ pressure coefficient increment due to separated vortex flow

$C_{p,\delta=90}$ pressure coefficient for the stagnation pressure behind a normal shock

C_{p,δ_s} pressure coefficient for sonic flow angle δ_s

ΔC_p lifting-pressure coefficient, lower surface minus upper surface

$\left(\Delta C_p\sqrt{x'}\right)_o$ limiting value of leading-edge singularity parameter at $x' = 0$

c local wing chord

$\bar{c}$ mean aerodynamic chord

c_{ave} average wing chord, S_{ref}/b

c_t theoretical section thrust coefficient, $(1/qc)(dt/dy)$

c_t^* attainable section thrust coefficient, $(1/qc)(dt/dy)$

c_v section vortex-force coefficient

e exponent (see eq. (25))

i,j indices used in numerical method element identification (see fig. 1)

k function of Mach number (see eqs. (21) to (24))

k_1, k_2, k_3, k_4 constants

L/D lift-drag ratio

M Mach number

M_∞ free-stream Mach number

M_i local Mach number given by adjusted linearized theory in three-dimensional flow (interference included)

M_o local Mach number given by adjusted linearized theory in two-dimensional flow (interference neglected)

q dynamic pressure

R free-stream Reynolds number based on $\bar{c}$

$\bar{R}_l$ influence function for lift (eq. (3))

$\bar{R}_t$ influence function for thickness (eq. (9))

S_{ref} wing reference area

t theoretical section leading-edge thrust

t^* attainable section leading-edge thrust

u,v nondimensional perturbation velocities in Cartesian coordinate system

$\Delta u, \Delta v$ change in nondimensional perturbation velocities across the lifting surface, upper surface minus lower surface

u_i nondimensional local longitudinal perturbation velocity given by adjusted linearized theory in three-dimensional flow (interference included)

u_o nondimensional local longitudinal perturbation velocity given by adjusted linearized theory in two-dimensional flow (interference neglected)

v_i nondimensional local lateral perturbation velocity given by linearized theory in three-dimensional flow (interference included)

x,y,z Cartesian coordinates, origin at wing apex

x' longitudinal distance behind wing leading edge

y' lateral distance from nearest leading edge

z_t thickness z-ordinate, upper surface minus lower surface

α	angle of attack, deg unless otherwise specified
α_{zt}	angle of attack for a local leading-edge thrust of zero
β	$= \sqrt{M_\infty^2 - 1}$
γ	ratio of specific heats
δ^*	effective flow deflection angle, deg
δ_s	flow deflection angle for sonic flow, deg
Λ	wing leading-edge sweep angle for delta wing, deg
Λ_{le}	local leading-edge angle, deg
λ	angle between tangent to local surface and free-stream velocity vector, deg
λ_i	equivalent turning angle due to local perturbation, deg
ν	Prandtl-Meyer expansion angle, deg
ν_i	Prandtl-Meyer expansion angle for M_i, deg
ν_o	Prandtl-Meyer expansion angle for M_o, deg
ξ,η	dummy variables of integration for x and y, respectively
ϕ	velocity potential
$\Delta\phi$	change in velocity potential

Subscripts:

c	camber surface
f	flat wing at $\alpha = 1^o$
ld	large disturbance
le	leading edge
max	maximum
sd	small disturbance
t	thickness
∞	free-stream conditions

DEVELOPMENT OF COMPUTATIONAL SYSTEM

This description of the development of the system for prediction of nonlinear supersonic aerodynamics is divided into two distinct parts. In the first part, numerical methods of implementing linearized theory to provide wing surface perturbation velocities and the full or 100-percent theoretical leading-edge thrust distribution are discussed. In the second part, semiempirical methods for estimation of pressure loadings and aerodynamic coefficients with nonlinear effects taken into account are discussed. Essentially, the nonlinear estimates are treated as corrections to the linearized solution. The assembled computational system thus incorporates the work described in both parts of the discussion. The linearized-theory solution could, however, be obtained from other numerical methods if they provide lateral as well as longitudinal perturbation velocities and if they provide a theoretical leading-edge thrust distribution.

Linearized-Theory Solution

Before corrections to account for nonlinear effects can be undertaken, linearized-theory perturbation velocities must first be evaluated. Both thickness- and lift-induced velocities must be considered, and lateral as well as longitudinal perturbation velocities must be determined. The general solution for a cambered wing with thickness at an angle of attack is built up from the separate contributions of a cambered wing with no thickness, an uncambered or flat wing of the same planform with no thickness at angle of attack, and an uncambered wing with a thickness distribution at 0° angle of attack.

Grid system used for linearized-theory solutions.- The linearized-theory solutions are obtained by numerical solutions of the linearized-theory integral equations based on a rectangular element grid system illustrated in figure 1. The wing surface is represented by an array of elements approximating the actual planform. Here, only a small number of elements are shown for the purpose of illustration; in practice several thousand elements would be employed. The employment of the β term in the lateral measurement allows the Mach line region of influence to be represented by the inclusion or rejection of whole elements. For better representation of the wing leading and trailing edges, partial elements are taken into account. A field point element (element number 30 in the illustration, fig. 1) is represented by the coordinates $x,\beta y$ and an influencing element is represented by the coordinates $\xi,\beta\eta$. The indexing notations, $i(x)$ and $j(\beta y)$, for example, are used in program identification of elements.

Lift-induced longitudinal perturbation velocity.- The method employed in the evaluation of longitudinal perturbations due to lift has been described in reference 1. Only slight modifications have been made in the present application. The primary change is in the designation of elements by a single element index number rather than by the indexing coordinates (L and N) previously employed. This permits a greater economy in provision for storage of the various parameters pertaining to a given element, since only elements within the wing planform need be considered. Perturbation velocities generated by the wing

camber surface at 0^o angle of attack and by a flat wing of the same planform at 1^o angle of attack are found by following the numerical summations:

$$\Delta u_c(x,\beta y) = \frac{-2}{\beta}\frac{\partial z}{\partial x}[i(x),j(\beta y)] + \frac{1}{\pi}\sum \bar{R}_1\, A[i(\xi),j(\beta\eta)]\, \Delta u_c[i(\xi),j(\beta\eta)] \quad (1)$$

$$\Delta u_f(x,\beta y) = \frac{-2}{\beta}\tan 1^o + \frac{1}{\pi}\sum \bar{R}_1\, A[i(\xi),j(\beta\eta)]\, \Delta u_f[i(\xi),j(\beta\eta)] \quad (2)$$

where the influence factor $\bar{R}_1$ is defined as

$$\bar{R}_1 = \frac{\sqrt{[i(x) - i(\xi) + 0.5]^2 - [j(\beta y) - j(\beta\eta) - 0.5]^2}}{[i(x) - i(\xi) + 0.5][j(\beta y) - j(\beta\eta) - 0.5]} - \frac{\sqrt{[i(x) - i(\xi) + 0.5]^2 - [j(\beta y) - j(\beta\eta) + 0.5]^2}}{[i(x) - i(\xi) + 0.5][j(\beta y) - j(\beta\eta) + 0.5]} \quad (3)$$

The summations cover only influencing elements forward of the Mach line and aft of the leading edge (the shaded area in fig. 1). Field point elements are taken in the order of increasing $i(x)$ values, so that no unknown values of Δu_c or Δu_f are encountered.

The present method also employs the aft element sensing technique described in reference 1 to provide a smoother distribution of velocities. The steps in implementation of this technique are

(a) Calculate and retain temporarily preliminary Δu values (Δu_c or Δu_f) for a given $i(x)$ row. Designate as Δu_1.

(b) Calculate and retain temporarily preliminary Δu values (Δu_c or Δu_f) for the following row, $i(x) + 1$, by using Δu_1 values obtained in the previous step. Designate as Δu_2.

(c) Calculate a final faired Δu value (Δu_c or Δu_f) for the element

$$\Delta u = \frac{1}{2}\left(1 + \frac{A}{1 + A}\right)\Delta u_1 + \frac{1}{2}\left(\frac{1}{1 + A}\right)\Delta u_2 \quad (4)$$

For all but leading-edge elements, this reduces to

$$\Delta u = \frac{3}{4}\Delta u_1 + \frac{1}{4}\Delta u_2 \quad (5)$$

Values of the perturbation velocities found by this process are assumed to act at the element midpoint.

Theoretical leading-edge thrust.- The evaluation of leading-edge thrust is discussed at this point because this force depends directly on the previously discussed lift-induced longitudinal perturbation velocities and because the corrected location of these velocities obtained in the thrust evaluation process will be used in procedures described in the following discussions. Reference 7 describes the procedures employed in much detail. The only notable difference in the present application is that no distinction is made between flat and cambered wings. For simplicity, the more general cambered wing formulation has been used exclusively.

The process described in reference 7 is used to find c_t for the cambered wing at the 0^o angle-of-attack input condition, designated $c_{t,c}$, and for the flat wing of the same planform at 1^o angle of attack, designated $c_{t,f}$. Section thrust coefficients can be found for any other angle of attack by application of the formula

$$c_t = c_{t,f}(\alpha - \alpha_{zt})^2 \tag{6}$$

where the angle of attack for zero thrust at the given span station α_{zt} is given by

$$\alpha_{zt} = \pm \sqrt{\frac{c_{t,c}}{c_{t,f}}} \tag{7}$$

in which the sign is the opposite of the sign of the cambered wing limiting thrust parameter. This expression for α_{zt} is found by solving equation (6) for α_{zt} and setting $c_t = c_{t,c}$ for $\alpha = 0^o$. Sketch (a) helps to illustrate the principle.

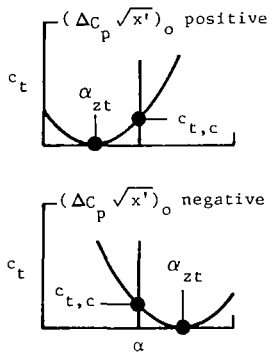

Sketch (a)

Lift-induced velocity potential.- The velocity potential is used in a subsequent evaluation of lateral velocities. It is obtained by a numerical integration of the lift-induced longitudinal perturbation velocities. For this purpose, a least-squares curve fit of an equation of the form $\Delta u = k_1 \frac{1}{\sqrt{x'}} + k_2 \pm k_3 x'$ is applied to the perturbation velocities. Since the velocity potential is the integral of the velocity $\phi = \int \Delta u = 2k_1\sqrt{x'} + k_2 x' + \frac{1}{2} k_3 (x')^2 + k_4$, this procedure provides simultaneously a smoothing of the velocities and a determination of the velocity potential. This first term of the equation represents a velocity distribution typical of the loading near the leading edge of a flat wing with a subsonic leading edge. The second term represents a uniform distribution as would be found near the leading edge of a flat wing with a supersonic leading edge, or near the leading edge of a cambered wing at design conditions. The third term provides an additional capability for the local fitting of distributions which may be rather arbitrary. The same procedure is applied to both the cambered and the flat wing; thus, Δu in the above equation for the velocity potential may represent either Δu_c or Δu_f, and ϕ may represent either ϕ_c or ϕ_f.

The number of elements used in the curve fit was chosen so as to match the smoothing to the velocity fluctuations introduced by steps in the program leading-edge definition. An example of severe fluctuations associated with a very highly swept leading edge ($\beta \cot \Lambda_{le} = 0.2$) is illustrated in sketch (b).

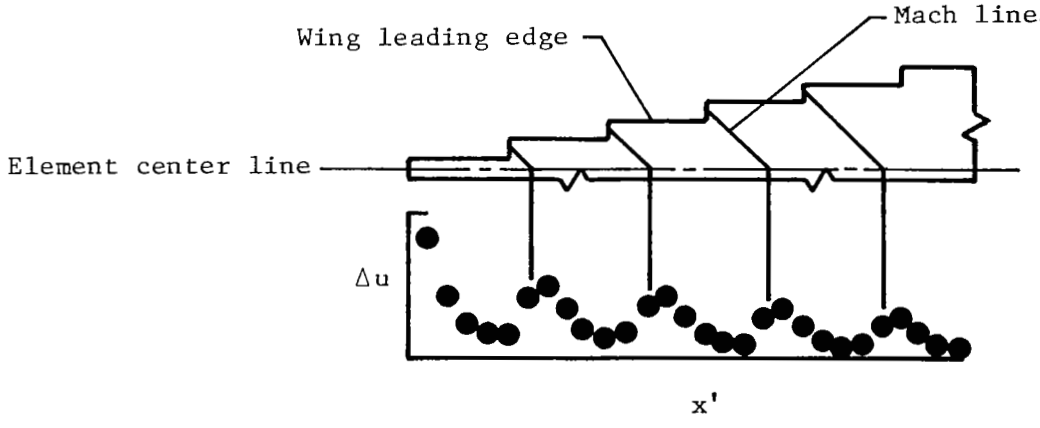

Sketch (b)

Both the magnitude and the wavelength of the oscillations have been observed to increase with increases in the leading-edge step size. The criteria adopted equated the number of elements to the integer value of $\frac{1}{\beta} \cot \Lambda_{le} + 3$. Thus, for sweep angles greater than $\beta \cot \Lambda_{le} = 0.5$,

only four elements are used. Large numbers of elements are used only for very highly swept wings.

The application of the procedure is illustrated in sketch (c). For a given element, the velocities considered include those for the element in question and

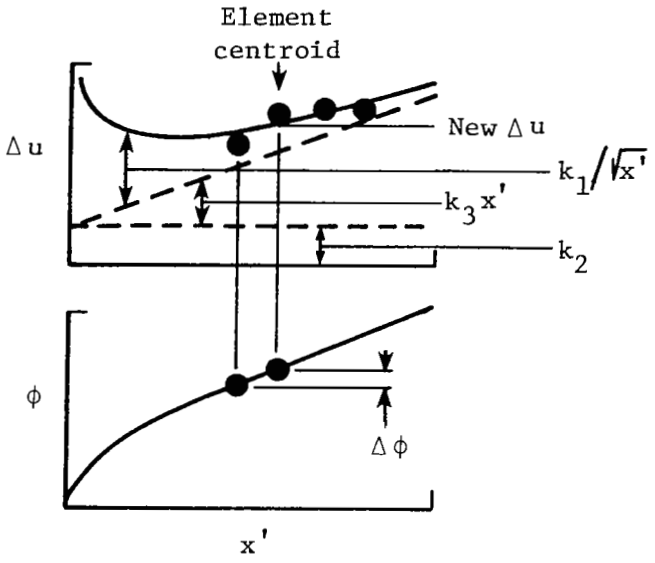

Sketch (c)

for the previous element plus those for enough following elements to provide the number specified by the previously mentioned criteria. The dashed lines in the sketch show the contributions of the three terms in the curve-fit equation. The new smoothed velocity for the element in question and the change in velocity potential from that of the previous element are also shown. The value of velocity potential for a given element is found by a summation of the changes of velocity potential from the leading edge for which ϕ is set to 0. Special provision is made for elements near the leading and trailing edges of the wing to maintain the number of elements specified by the smoothing criteria.

Thickness-induced velocity potential.- It is more convenient to adopt the method described in reference 2, which provides the thickness velocity potential distribution, than to solve for the velocities directly. The use of the velocity potential distribution to obtain longitudinal and lateral perturbation velocities due to wing thickness is described in subsequent sections of this report. Procedures for the evaluation of the thickness-induced velocity potential are similiar to those used in the definition of lift-induced velocities. The same grid system is employed (shown in fig. 1), and the summations cover the same limits. The summation equation, however, is written as

$$\phi_t = \frac{1}{\pi\beta} \sum \tilde{R}_t \, A[i(\xi), j(\beta\eta)] \frac{\partial z_t}{\partial x}[i(\xi), j(\beta\eta)] \qquad (8)$$

where the influence function is now

$$\bar{R}_t = \sin^{-1}\left[\frac{j(\beta y) - j(\beta\eta) - 0.5}{i(x) - i(\xi) + 0.5}\right] - \sin^{-1}\left[\frac{j(\beta y) - j(\beta\eta) + 0.5}{i(x) - i(\xi) + 0.5}\right] \qquad (9)$$

Evaluation of the summations provides values of ϕ at the front and back of each element. Element midpoint values are found by a simple averaging. In contrast to the lift-induced velocity potential, the thickness-induced velocity potential is not necessarily zero at the wing leading edge. A value of ϕ_t at the leading edge $\phi_{t,le}$ for each leading-edge element is found by interpolation. Application of the aft element sensing technique was not found to be necessary in the derivation of the thickness velocity potential.

Thickness-induced perturbation velocities.- To find thickness velocities, a least-squares curve fit of an equation of the form $\phi_t = k_1\sqrt{x'} + k_2x' + k_3(x')^2 + \phi_{t,le}$ is applied to the thickness-induced velocity potential described in the previous section. Since the longitudinal perturbation velocity is the derivative of the velocity potential, $u_t = \frac{\partial\phi_t}{\partial x'} = \frac{1}{2}k_1\frac{1}{\sqrt{x'}} + k_2 + 2k_3x'$. This procedure simultaneously provides a smoothing of the velocity potential and a determination of the perturbation velocity. The number of elements used in the curve fit has already been discussed in the section entitled "Lift-induced velocity potential." Application of the procedure is illustrated in sketch (d). The dashed lines show the contribution of the four terms in the curve-fit equation.

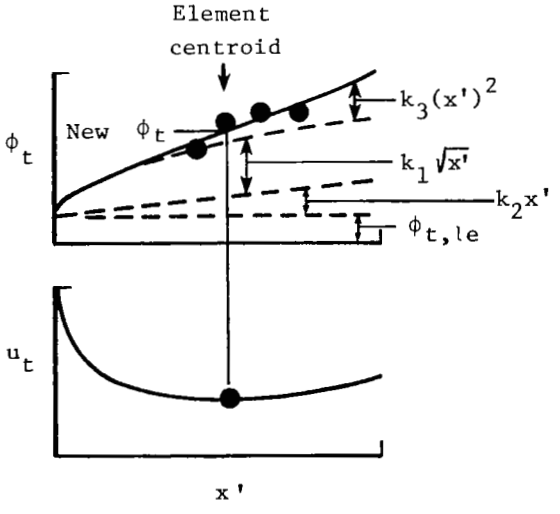

Sketch (d)

Lateral perturbation velocities.- The lateral velocity, or the sidewash, is determined by a lateral curve fit and subsequent differentiation of the velocity potential. The process is the same whether the sidewash is due to camber lift, flat-plate lift, or thickness. In the following discussion of lateral velocity evaluation, v can be considered to represent either Δv_c, Δv_f, or v_t, and ϕ can be considered to represent either ϕ_c, ϕ_f, or ϕ_t. The first step in the determination of lateral velocities is the identification of the nearest leading edge inboard or outboard of the midpoint of the element under consideration (illustrated in sketch (e)). The program contains the necessary

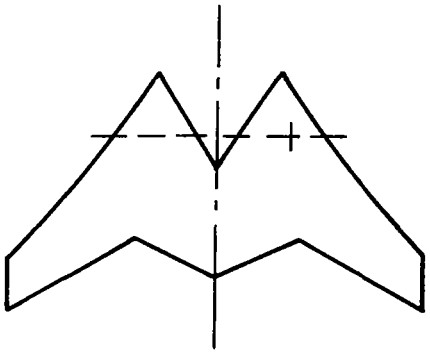

Sketch (e)

logic for identification of all intersections of the leading edge with the x = Constant line and for selection of the nearest point. When, as in sketch (e), the nearest leading-edge point lies to the right, a least-squares curve fit of an equation of the form $\phi = \phi_{le} + k_1\sqrt{y'} + k_2 y' + k_3(y')^2$ can be applied to the velocity potential data, and the lateral velocity is found from the derivative equation

$$v = \frac{\partial \phi}{\partial y} = \frac{1}{2}\frac{k_1}{\sqrt{y'}} + k_2 + 2k_3 y'$$

A typical application is illustrated in sketch (f). Normally five points are used in the curve fit: the element in question and two on each side. Special provisions are made when there are less than five full elements within the wing planform limits. For example, when a leading-edge element is included, its midpoint ϕ value is excluded, and the local leading-edge ϕ value and its y' position are substituted. The curve fit just described is applicable for three or more points; when only two points are available, a linear equation curve fit is imposed. In the very special case, where only a single leading-edge element is present (as in the apex region of a wing with a highly swept leading edge), the lateral velocity may be approximated as $u/\cot \Lambda_{le}$. When the nearest leading-edge point lies to the left, the process is the same except for the change in direction of the y' measurement.

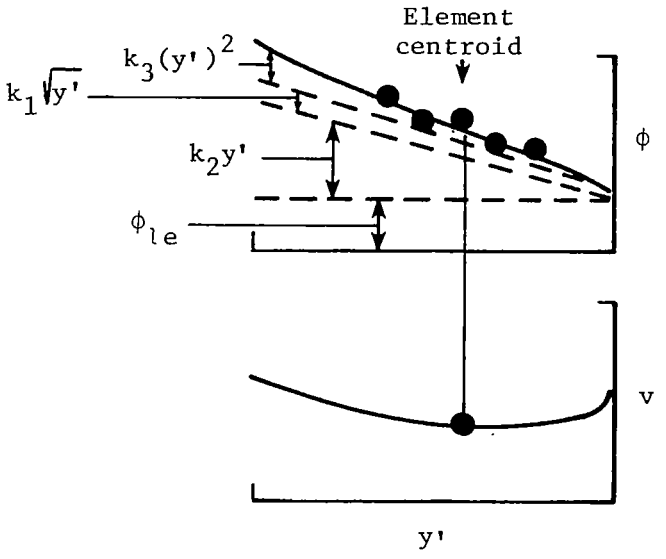

Sketch (f)

Combination of separate contributions.- Local velocities on the wing surface can be found by direct addition of the velocity contributions:

Upper surface	Lower surface	
$u = u_t + \frac{\Delta u_c}{2} + \frac{\Delta u_f}{2}\alpha$	$u = u_t - \frac{\Delta u_c}{2} - \frac{\Delta u_f}{2}\alpha$	(10)
$v = v_t + \frac{\Delta v_c}{2} + \frac{\Delta v_f}{2}\alpha$	$v = v_t - \frac{\Delta v_c}{2} - \frac{\Delta v_f}{2}\alpha$	(11)

Linearized-theory local pressure coefficients are evaluated by the simple formula $C_p = -2u$.[1]

Wing overall forces and moments could be found by suitable numerical integrations performed separately for each angle of attack under consideration. It is more economical, however, to use the linear nature of the solution in compu-

[1]Other more complex linearized-theory formulations involving both u and v perturbation velocities offer no advantage over the simpler approach. Some examples are shown in reference 6. Many linearized-theory numerical methods, in fact, do not provide for evaluation of lateral velocities.

tation of mutual interference drag coefficients between the cambered and flat surfaces (discussed in ref. 1, for example).

Estimation of Nonlinear Effects

In development of this system for estimation of nonlinear supersonic aerodynamics, an attempt has been made to correct for the major deficiencies of linearized-theory methods. The first deficiency is in the prediction of basic attached-flow pressure distributions. Generally, linearized-theory methods tend to underestimate loadings in the region of the wing root and to overestimate loadings near the wing tip. Another source of error is the inability of linearized-theory methods to provide realistic estimates of either the leading-edge thrust forces that may actually be realized or of the vortex forces that appear when thrust is not developed. Methods of correcting linearized-theory solutions to account for these nonlinear effects are discussed next.

Nonlinear pressures in attached flow.- The method employed here for the estimation of pressure loading nonlinearities is basically that presented in reference 6. There are, however, some significant differences that should be discussed. For completeness, the whole process is outlined.

This method uses a pressure-coefficient formulation which combines the more exact, two-dimensional, interference-free prediction capabilities of the shock-expansion relationships with the linearized-theory capabilities for handling of three-dimensional interference effects. In brief, a local pressure coefficient $C^*_{p,a}$ is calculated in accordance with the shock-expansion relationships for an effective deflection angle δ^*. This effective deflection angle includes a purely geometric component (based on the local surface slope relative to the free stream) and an aerodynamic interference component (based on local interference velocities evaluated by linearized-theory methods).

A typical variation of the pressure coefficient $C^*_{p,a}$ with the effective deflection angle δ^* is shown in sketch (g). The pertinent equations are

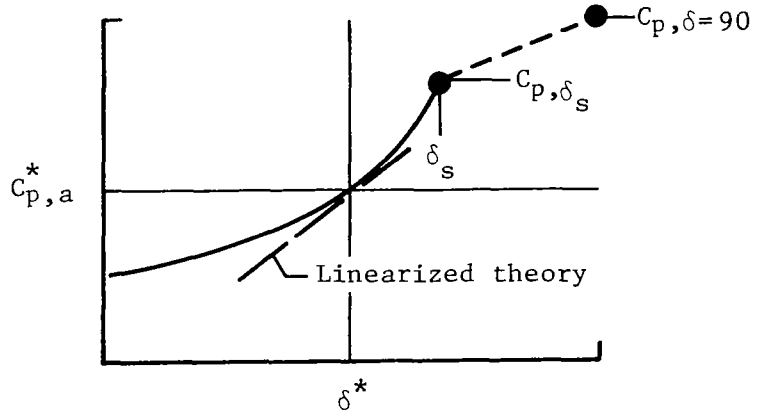

Sketch (g)

given in the appendix of reference 6. At the point labeled δ_s, the flow on the deflected surface becomes sonic.[2] For δ^* values greater than δ_s, no valid solution can be found because the problem then involves a mixed supersonic and subsonic flow, and neither supersonic linearized-theory nor shock-expansion relationships are applicable. Because only a small portion of the flow may be affected in many cases, calculations for the examples shown in this report were not terminated when δ^* became larger than δ_s. Instead, an arbitrary linear fairing between the pressure coefficient for sonic flow C_{p,δ_s} and the pressure coefficient corresponding to the stagnation pressure behind a normal shock $C_{p,\delta=90}$ was introduced. Thus, present method solutions for cases in which the local surface angles exceed the sonic flow deflection angle over an appreciable portion of the wing may be suspect.

In order to determine the effective deflection angle, a local linearized-theory Mach number M_i, which includes interference effects, and a local linearized-theory Mach number M_o, which would be generated on a two-dimensional surface having the same slope, must be defined. The difference between these two Mach numbers provides a measure of the magnitude of three-dimensional interference effects given by the linearized-theory solution. The local Mach numbers are determined from the linearized-theory perturbation velocities:

$$M_o = M_\infty(1 + u_o)$$

$$M_i = M_\infty(1 + u_i)\sqrt{1 + v^2}$$

Linearized-theory longitudinal perturbation velocities may range from positive to negative infinities. Since local Mach numbers could realistically become very large, the positive infinity limit is acceptable. However, local Mach numbers less than 0 are believed to be unrealistic; therefore, negative longitudinal perturbation velocities are adjusted to give a lower limit of -1 corresponding to a local Mach number of 0. The adjustment is illustrated in sketch (h). The velocities u_i and u_o are the corrected values used in local Mach number definition, and the velocity u is the nonadjusted value given by linearized theory. For positive values of u, u_i or $u_o = u$. For negative values of u,

$$u_i \text{ or } u_o = 1 - \frac{2}{\left(\frac{1}{1 - u}\right)^2 + 1} \tag{12}$$

---

[2]In reference 6, this point was labeled δ_d and described as the angle for shock detachment; however, the equation given in that report is actually that for sonic flow. The sonic flow condition is probably a better indication of the limit of solution validity than is the shock detachment angle. Therefore, the sonic flow point δ_s is adopted for the present method, and the incorrectly labeled equation from reference 6 is retained. The sonic flow angles are less than the shock detachment angle, but the differences are small.

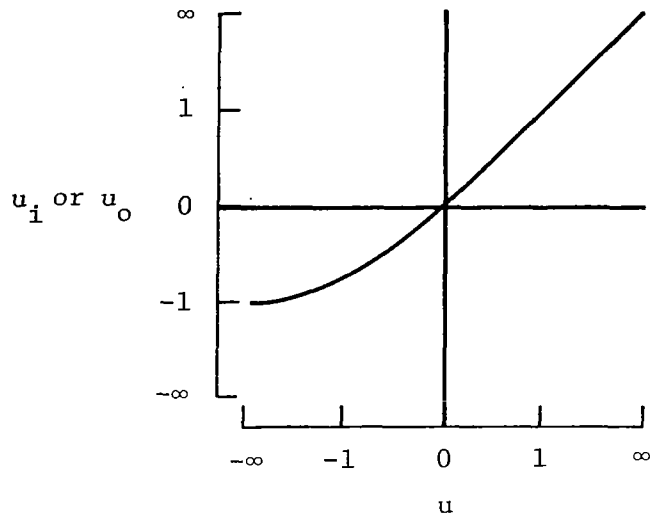

Sketch (h)

For all values of v, $v_i = v$. In determination of u_i and M_i, u and v values are those provided by the linearized-theory wing program. In determination of u_o and M_o, u is given by the linearized-theory two-dimensional expression:

$$u = \frac{-\lambda}{\beta} \frac{\pi}{180} \tag{13}$$

The aerodynamic interference component of the effective deflection angle is determined from the Prandtl-Meyer expansion relationship between the expansion angle and the local Mach number:

$$\nu = \sqrt{6} \tan^{-1} \sqrt{\frac{M^2 - 1}{6}} - \cos^{-1} \left(\frac{1}{M} \right) \tag{14}$$

For the expansion angle ν_i corresponding to the local flow solution with interference, M_i is used as M in equation (14). For the interference-free expansion angle ν_o, M_o is used. The aerodynamic interference component of the effective deflection angle λ_i is then simply $\nu_o - \nu_i$. The determination of λ_i for a sample case is illustrated in sketch (i).

When the local Mach numbers M_o or M_i become less than 1, the Prandtl-Meyer expansion equations are no longer applicable; and without special provisions, the whole calculation process would have to be terminated. Therefore,

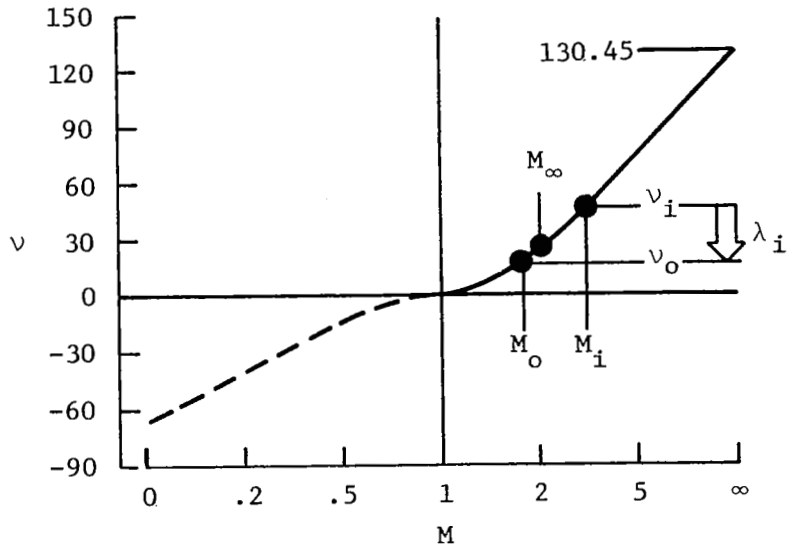

Sketch (i)

provision has been made to provide fictitious expansion angles for local Mach numbers less than 1 so that the process may continue. For M_o and M_i less than 1, the expansion angles are defined by

$$\nu = (\nu_\infty - 90)(1 - M)^2 \tag{15}$$

Normally, this provision is not employed unless the local surface slope exceeds by an appreciable margin the sonic flow angle δ_s for the free-stream Mach number. The assumed relationship for local Mach numbers less than 1 is shown as a dashed line in sketch (i).

As just described, the interference component of the effective deflection is added to the purely geometric component to find the complete effective deflection angle:

$$\delta^* = \lambda + \lambda_i = \lambda + \nu_o - \nu_i \tag{16}$$

where λ is the angle in the x-z plane between a tangent to the local surface and the free-stream velocity vector. As noted previously, this effective deflection angle is then used in shock expansion expressions to define a pressure coefficient $\Delta C_{p,a}^*$ which has been corrected for nonlinear effects. This completes the description of the method as presented in reference 6.

Correlations of the corrected pressure coefficient with experimental data presented in reference 6 showed that the corrected pressure coefficient provided a much improved prediction of local pressure distributions at high super-

sonic Mach numbers and large angles of attack. For low supersonic Mach numbers and moderate angles of attack, the differences between the new method and conventional linearized-theory results were relatively small. Contrary to expectations, however, it was found that the smaller the magnitude of the pressure coefficient, the more likely that conventional linearized theory would give a better prediction. Therefore, in order to provide a more uniformly valid improvement over linearized theory, a modification to the method of reference 6 has been introduced. The objective is to provide a better merging of the two methods.

As shown in sketch (g), $C^*_{p,a} = 0$ for δ^* of zero. In addition, the derivative $\partial C^*_{p,a}/\partial\delta^*$ at $\delta^* = 0$ is equal to the linearized-theory value of $2\pi/180\beta$. However, the variation of ν with M as depicted in sketch (j)

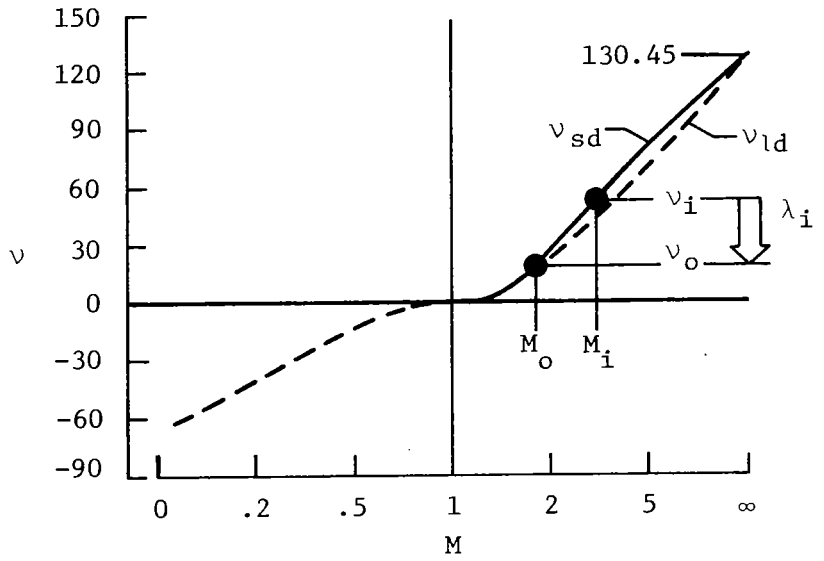

Sketch (j)

also influences the merging of the two methods. The present method results converge with linearized-theory results for small values of the perturbation velocities only if M_i equals M_o (the two-dimensional case) or if the derivative $\partial\nu/\partial M$ satisfies the linearized-theory condition

$$\frac{\partial\nu}{\partial M} = \frac{\beta}{M_\infty}\frac{180}{\pi} \tag{17}$$

This consideration led to the development of what has been termed a small-disturbance formulation of the nonlinear method. (The previously described method taken from ref. 6 is considered the large-disturbance formulation.)

A modified variation of the expansion angle ν with the local Mach number to be used in the small-disturbance formulation is illustrated in sketch (j). For M greater than M_O the curve has the following form:

$$\nu = 130.45 + k_1\left(\frac{1}{1 + M}\right) + k_2\left(\frac{1}{1 + M}\right)^2 \tag{18}$$

For M less than M_O, the curve has the form

$$\nu = k_1\left(\frac{1}{2} - \frac{1}{1 + M}\right)^2 + k_2\left(\frac{1}{2} - \frac{1}{1 + M}\right)^3 \tag{19}$$

The constants are selected to pass the curve through the point at M_O with the linearized-theory slope. The small-disturbance formulation pressure coefficient is obtained when this curve, rather than that depicted in sketch (i), is used to define λ_i. For comparison, the large-disturbance formulation from sketch (i) is shown as a dashed line in sketch (j).

In the final formulation for the pressure coefficient used in the present method, a compromise has been made between the small- and large-disturbance formulations. The compromise provides a weighting toward the small-angle formulation when the local surface angle is small (when M_O approaches M_∞) and when the interference effects are small (M_i approaches M_O). For this purpose, the expansion angle is defined as

$$\nu = \nu_{ld} + k(M)(\nu_{sd} - \nu_{ld}) \tag{20}$$

where

$$k(M) = k(M_O)\ k(M_i)$$

The form of the expressions for $k(M_O)$ and $k(M_i)$ are shown in sketch (k) on page 20.

For M_O less than M_∞,

$$k(M_O) = \cos^2\left[90^o\left(\frac{\frac{1}{1 + M_O} - \frac{1}{1 + M_\infty}}{\frac{1}{2} - \frac{1}{1 + M_\infty}}\right)^e\right] \tag{21}$$

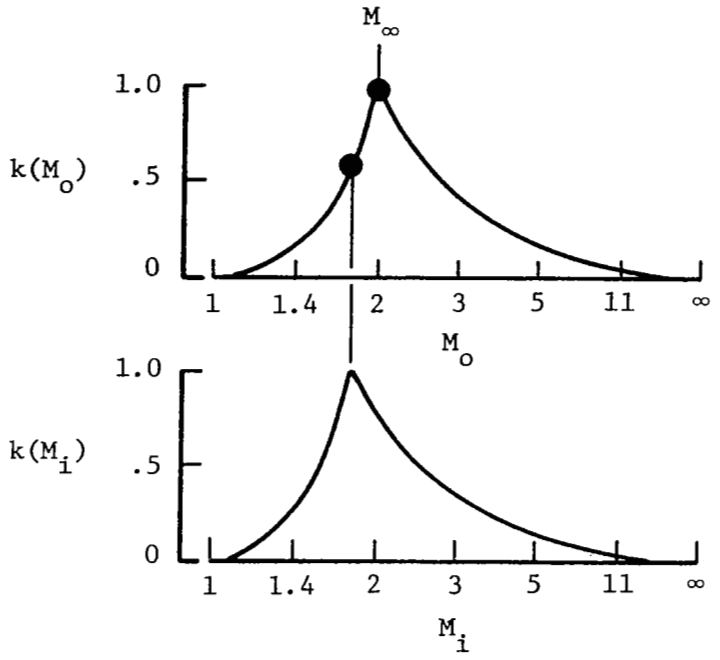

Sketch (k)

For M_o greater than M_∞,

$$k(M_o) = \cos^2 \left[90^o \left(\frac{\frac{1}{1 + M_\infty} - \frac{1}{1 + M_o}}{\frac{1}{1 + M_\infty}} \right)^e \right] \tag{22}$$

For M_1 less than M_o,

$$k(M_i) = \cos^2 \left[90^o \left(\frac{\frac{1}{1 + M_i} - \frac{1}{1 + M_o}}{\frac{1}{2} - \frac{1}{1 + M_o}} \right)^e \right] \tag{23}$$

For M_i greater than M_o,

$$k(M_1) = \cos^2\left[90^o\left(\frac{\frac{1}{1+M_o} - \frac{1}{1+M_i}}{\frac{1}{1+M_o}}\right)^e\right] \tag{24}$$

An example of the final compromise form of the expansion angle dependence on local Mach numbers is depicted in sketch (1). The expression used for ν in

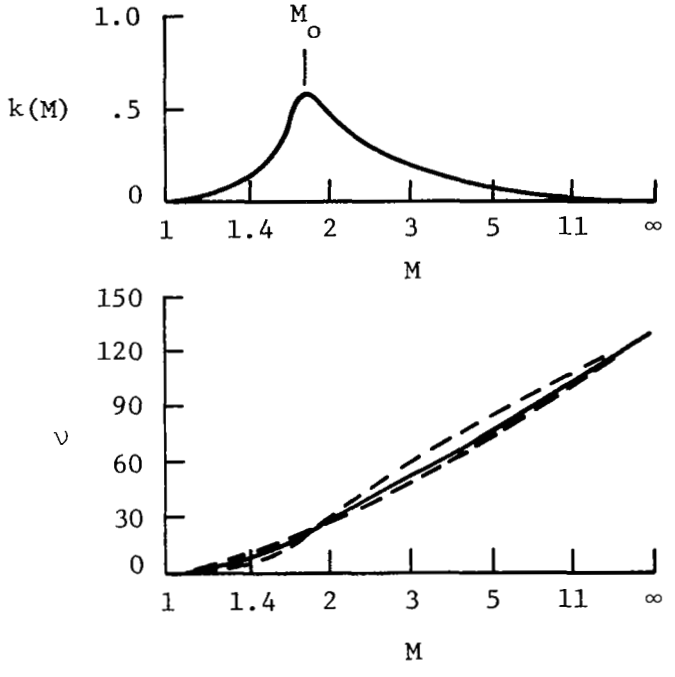

Sketch (1)

the present system, the solid line, is compared with the small- and large-disturbance limits represented by the dashed lines. The exponent e in equations (21) to (24) was determined by trial and error in comparisons of predictions with experimental data. The value of the exponent used is given by

$$e = \frac{0.45}{\sqrt{M_\infty}} + \frac{7}{\left(M_\infty^2 - 1\right)^4} \tag{25}$$

As might be expected, the final solution is not overly sensitive to variations in the value of e. However, it was found to be important that e approach infinity as the Mach number approached 1 so that the solution would tend toward the small-disturbance formulation.

Nonlinear pressures in vortex flow.- An additional source of nonlinearities is associated with the phenomena of leading-edge thrust and the detached leading-edge vortex system that forms when leading-edge thrust fails to develop. Prediction of theoretical leading-edge thrust c_t is discussed in an earlier section of this paper. A method for estimating the portion of this thrust that actually may be attained c_t^* is described in references 8 and 9. This method has been incorporated in the present system but will not be presented here because it is covered in much detail in the references cited.

For wings with sharp leading edges, for which no leading-edge thrust is assumed to develop, Polhamus (ref. 10) established a relationship between the normal force induced by the separated vortex flow and the theoretical leading-edge thrust. According to the Polhamus suction analogy, the suction vector $c_t/\cos \Lambda_{le}$ is assumed to rotate to a position normal to the wing surface, where it affects the normal force rather than the chord force. Because the present method treats a partially developed leading-edge thrust, it seems logical to consider a partial development of the vortex force. The simplest approach is to equate the vortex force with the undeveloped thrust:

$$c_v = \frac{c_t - c_t^*}{\cos \Lambda_{le}} \tag{26}$$

This treatment differs from the approach of reference 8, which postulates a gradual rotation of the thrust vector. The present scheme provides a simpler way of handling thrust and vortex forces for wings with twist and camber.

The suction analogy provides no information on the point of application of the vortex force vector. There is an implied assumption that it acts just behind the leading edge. Since the vortex flow field can act at locations which under some conditions may be far removed from the leading edge, accurate estimates of the vortex-induced normal force, and particularly of the pitching moment, can be made only with some knowledge of the location of the vortex flow field.

For the special case of wings designed for supersonic cruise and operating at supersonic speeds, a simple empirical relationship (shown in fig. 2) may be used to provide an approximate location for the vortex action line. This case is simplified because wings designed for supersonic cruise tend to approach delta planforms and because delta wings at supersonic speeds display a conical flow field. Delta wing data from references 11 and 12 were used to define the location of the vortex center. The data provided no discernible evidence of trends with the other parameters - Mach number and sweep angle. However, the

data exhibited a considerable amount of scatter, indicating an obvious need for an improved correlation based on a larger amount of more accurate experimental data. The curve fit shown in the figure is given by

$$\frac{\cot \Lambda_v}{\cot \Lambda_{le}} = \frac{1}{1 + 2.7 \tan \alpha} \tag{27}$$

A very simplified approach has been used to provide an approximation for the vortex force distribution (illustrated in sketch (m)). At a given wing

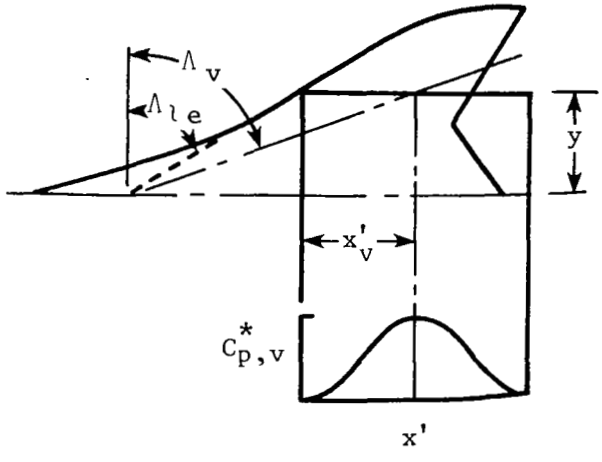

Sketch (m)

spanwise station, the local leading-edge sweep angle is defined by a line tangent to the leading edge. The center of the vortex field is assumed to be above the point

$$x'_v = \frac{y}{\cot \Lambda_{le}} \left(\frac{\cot \Lambda_{le}}{\cot \Lambda_v} - 1 \right) = \frac{y}{\cot \Lambda_{le}} (2.7 \tan \alpha) \tag{28}$$

The pressure distribution supporting the vortex force is assumed to have the form shown in the sketch and to be represented by the equation

$$\Delta C_{p,v} = c_v \frac{c_{ave}}{x'_v} \cos^2 \left[90^\circ \left(1 + \frac{x'}{x'_v} \right) \right] \tag{29}$$

This provision allows the vortex force to be represented by an incremental pressure distribution to be added directly to the basic attached-flow pressure distributions. In this way, any loss in vortex force due to vortex field location behind the wing trailing edge or due to local pressures exceeding the vacuum limit may be taken into account.

The present method for estimation of attainable leading-edge thrust has been developed for flat wings with symmetrical sections. However, the method is adaptable to wings with limited twist and camber when it is coupled with lifting-surface programs capable of providing accurate theoretical leading-edge thrust distributions. Sketch (n) illustrates this application. Since the air-

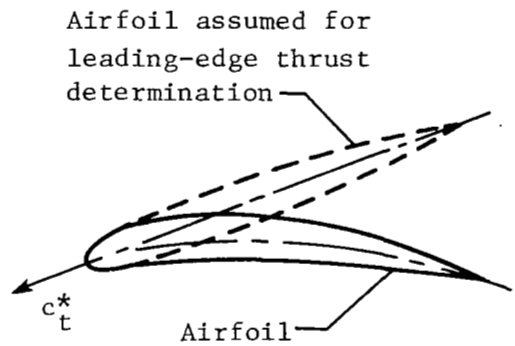

Sketch (n)

foil profile in the immediate vicinity of the leading edge has a dominant influence on the thrust characteristics, the attainable thrust may be analyzed by calculations for a comparable symmetric wing section. This section has a plane of symmetry which is tangent to the mean camber surface of the nonsymmetrical section at the leading edge. The superimposed symmetrical section is assumed to have the same thickness ratio, leading-edge radius, and location of maximum thickness as the cambered section. The thrust vector is assumed to act at an angle with respect to the wing-chord plane defined by the tangent to the camber surface at the leading edge. The vortex force is assumed to act on the surface of the airfoil section in accordance with the pressure distribution previously discussed. Thus, for a cambered wing, the vortex force could contribute to the chord force as well as to the normal force and pitching moment. For the cambered wing section, x_v' is defined as

$$x_v' = \frac{y}{\cot \Lambda_{le}}[2.7 \tan (\alpha - \alpha_{zt})] \tag{30}$$

If α is less than α_{zt}, the vortex pressures are allowed to act on the lower rather than on the upper surface of the airfoil section.

Because of limitations in the generality of this empirical method for handling vortex-induced pressures, it cannot be used with any confidence for wings which depart substantially from delta planforms[3] nor for wings which employ more than a modest degree of twist and camber.

Computer Program

A computer program entitled "Supersonic Wing Nonlinear Aerodynamics," which combines the linearized-theory wing solution with the methods for estimation of nonlinear effects presented here, may be obtained at a nominal fee from

Computer Software Management and Information Center (COSMIC)
112 Barrow Hall
University of Georgia
Athens, Georgia 30602
(404)542-3265

Request the program by the designation LAI 12788. The program is written in FORTRAN IV for use on the Control Data 6600 series of computers and requires approximately 130 000 octal locations of core storage.

Data are input in namelist form under the code INPT1. The wing planform information is specified by a series of leading- and trailing-edge breakpoints. Up to 21 pairs of coordinates may be used to describe the leading edge and up to 21 pairs to describe the trailing edge. The planform input data in program terminology are

NLEY — number of leading-edge breakpoints (limit of 20)

TBLEY — table of leading-edge y-values in increasing order of y from wing root to wing tip

TBLEX — table of leading-edge x-values corresponding to the TBLEY table

NTEY — number of trailing-edge breakpoints (limit of 20)

TBTEY — table of trailing-edge y-values in increasing order of y from wing root to wing tip

TBTEX — table of trailing-edge x-values corresponding to the TBTEY table

XMAX — largest x-ordinate occurring anywhere on the planform

---

[3]For wings which depart drastically from a delta planform (swept-forward wings, for example), only the vortex loadings are improperly treated; all other loadings, including the leading-edge thrust, are handled properly. Program data provide sufficient information so that the vortex flow increments may be excluded from the pressure distributions and overall forces and moments, if desired.

SREF wing reference area for use in aerodynamic force and moment coefficients

CBAR wing reference chord for use in aerodynamic moment coefficients

XMC x-location of moment reference center

The size of the wing in program dimensions is controlled by the entry:

JBYMAX integer designating the number of elements in the spanwise direction (see fig. 1) (limit of 101)

The necessary scaling is done within the program by use of a scale factor $2(JBYMAX - 0.5)/(SPAN \times BETA)$. The number of elements N corresponding to a given JBYMAX or the value of JBYMAX corresponding to a given number of elements may be approximated as

$$JBYMAX = (\sqrt{1 + 4AN} - 1)/2A$$

$$N = A \times JBYMAX^2 + JBYMAX$$

where

$$A = \frac{2\ SREF}{SPAN^2\ BETA}$$

The program has been written to accommodate 2000 elements. Except in very special cases the JBYMAX integer will be much less than the limit of 101. The normal range is 30 to 40. If the selected JBYMAX is too large for the allowable 2000 elements, program logic will determine the largest usable value and make a substitution.

The wing section mean camber surface and the wing section thickness must be specified by exactly 26 chordwise ordinates at up to 21 span stations. When fewer than 26 camber or thickness coordinates are used to define the sections, the ordinate tables must be filled with enough zeros to complete the list of 26. The camber and thickness spanwise location of sections need not be the same. The necessary section information is

NYC number of spanwise stations at which chordwise sections are used to define the mean and camber surface (limit of 21)

TBYC table of y-values for the chordwise camber surface sections, increasing order of y from root to tip

NPCTC number of chordwise stations used in mean camber surface definition (limit of 26)

TBPCTC table of chordwise stations, in percent of chord, at which mean camber surface ordinates are defined; in increasing order from leading to trailing edge

TZORDC table of mean camber surface z-ordinates corresponding to the TBPCTC table; the full 26 values for the root chord (including zeros for values in excess of NPCTC) are given first, followed by similar information for all spanwise stations in increasing order of y

NYT number of spanwise stations at which chordwise sections are used to define the thickness distribution (limit of 21)

TBYT table of y-values for the chordwise thickness distribution sections, increasing order of y from root to tip

NPCTT number of chordwise stations used in thickness distribution definition (limit of 26)

TBPCTT table of chordwise stations, in percent of chord, at which thickness distribution ordinates are defined; increasing order from leading to trailing edge

TZORDT table of thickness distribution z-ordinates as a fraction of local chord (full, not half-thickness) corresponding to the TBPCTT table; the full 26 values for the root chord (including zeros for values in excess of NPCTT) are given first, followed by similar information for all spanwise stations in increasing order of y

The TZORDC table may be multiplied by a scale factor TZSCALE if desired. This may be useful if the original tabulated ordinates are nondimensionalized with respect to a single measurement (the wing root chord, for example) or if it is necessary to evaluate the effect of a change in camber surface severity.

The following wing section information is required for the calculation of attainable leading-edge thrust. Data are required for the same span stations TBYT used in definition of the wing section thickness distribution

TBTOC table of airfoil maximum thickness as a fraction of the chord

TBETA table of η, the section location of maximum thickness as a fraction of the chord

TBROC table of the leading-edge radius as a fraction of the chord

For wing sections with theoretically sharp leading edges (circular-arc sections, for example), it may be desirable to estimate a leading-edge radius which is constant along the entire leading edge. In this case, a single entry RLE is

made, and the TBROC table is preempted. The test or flight conditions are specified as

XM free-stream Mach number

RN free-stream Reynolds number (based on $\bar{c}$) in millions, $R/10^6$

NALPHA number of angles of attack to be calculated (limit of 20)

TALPHA table of angles of attack to be calculated

One of three options for printing results may be selected by choice of the IPRINT entry:

IPRINT = 1 only the overall force and moment coefficients are printed

IPRINT = 2 in addition to the overall force and moment coefficients, section coefficient distributions are printed for a selected series of angles of attack

IPRINT = 3 in addition to the overall force and moment coefficients, pressure distributions are given for selected angles of attack (as in IPRINT = 2) and for specified span stations

NALPHP number of angles (limit of 20)

TALPHP table of angles (must correspond to TALPHA entries)

NJBYP number of span stations

JBYP table of span stations identified by integers from 1 to JBYMAX

$$\frac{y}{b/2} = \frac{JBYP - 1}{JBYMAX - 0.5}$$

COMPARISONS WITH EXPERIMENTAL DATA

The applicability of the present method to practical problems (the estimation of pressure loadings and aerodynamic force and moment coefficients, for example) can be assessed by means of a series of comparisons of predictions with the experimental measurements presented in figures 3 to 16. In these figures, the curves labeled "Present method" have been obtained by use of the computer program described in the section of this paper entitled "Computer Program." The computer program is based on theoretical concepts discussed in the section "Development of Computational System." Estimates based on conventional linearized theory are also shown for comparison. Linearized-theory results were obtained from the same computer program.

Since the present method provides detailed thickness pressure distributions over the surface of the wing, the wave drag contribution to $C_{D,o}$ for an uncambered wing at 0° angle of attack could be found by integration. However, for

wings with rounded leading-edge sections, this numerical method may not provide a sufficiently accurate estimate of this drag for a normal grid size (number of elements) to give a reasonably accurate prediction of lift effects. Furthermore, the present method does not account for the contribution to $C_{D,o}$ of other configuration components and their mutual interference. Therefore, a general practice of combining estimates of lift-generated characteristics given by the present method with estimates of thickness-generated characteristics given by other methods (refs. 2 to 4, for example) is recommended. For the comparisons with experimental data shown in this report, experimental values of $C_{D,o}$ were used in place of the program-generated $C_{D,o}$. Where comparisons were made for a series of twisted and cambered wings, $C_{D,o}$ was determined from experimental data for the flat wing only, so that predictions of drag variations with camber surface severity or design lift coefficient are those given by the present method.

A comparison of predicted and measured pressure distributions (refs. 13 and 14) for an uncambered semispan delta wing of aspect ratio 2 is shown in figure 3. First, note the data for $M = 1.45$. For this Mach number, the deflection angle for sonic flow is 10.37°; thus the 20° angle of attack is far too large for a reasonable expectation of good agreement between prediction and measurement. For all of the wing lower surface ahead of the break in the present method curve, local Mach numbers M_i of less than 1 are indicated. Of course, the presence of such a large region of subsonic flow invalidates any solution given by methods which assume all supersonic flow. This is really a mixed or transonic flow problem. The present method prediction ahead of the breakpoint results from an arbitrary description of C_p^* vs δ^* as discussed in the section entitled "Development of Computational System." For $M = 1.97$, the sonic flow angle is 22.17°; thus, the 20° angle-of-attack data (shown in fig. 3(b)) are near the upper limit of applicability.

Within the range of applicability, data for all the Mach numbers described by figure 3 indicate that a generally improved prediction of wing pressure distribution is offered by the present method. Improvements in prediction of loadings on the wing undersurface near the root chord are particularly noticeable. The new method also tends to avoid the overestimation of pressure loadings in the wing leading-edge and tip regions. And, although agreement is far from exact, the program-predicted incremental loading due to the detached vortex flow field does appear to provide a better estimate of upper surface loadings than does the linearized theory. Of particular significance is the provision within the present method for the loss in suction force when the vortex core nears and moves behind the wing trailing edge. Note the changing patterns of the upper surface pressure distributions of a given angle of attack as the span station increases. The suction force would tend to increase linearly with increasing span position if the spreading of the pressure distribution increments were not taken into account.

Data from references 13 and 14 were used in a "calibration" of the present method. In the section "Development of Computational System," two formulations of the present method were discussed. The large-disturbance formulation is identical to that of reference 6. The small-disturbance formulation was introduced to provide a better estimate for small angles of attack and low supersonic Mach numbers. For very small disturbances, the small-disturbance formulation

gives results identical to those provided by linearized theory. The present method uses a mixture of small- and large-disturbance formulations to provide a transition from linearized-theory estimates to those given by the large-disturbance formulation of reference 6, as the Mach number and the local disturbance effects increase. The small- and large-disturbance limits and the chosen transition are illustrated in figure 4. Wing lower surface pressures are shown as a function of angle of attack for several representative locations. In view of the relatively small differences between the limits, the process resembles a "fine tuning" operation. At $M_\infty = 1.45$, the small-disturbance formulation predominates. At the highest Mach number, the large-disturbance formulation is favored. This figure depicts quite clearly the nonlinear nature of supersonic wing pressure variations with angle of attack.

Pressure data (ref. 15) for an uncambered delta wing with a leading-edge sweep angle of 76° are shown in figure 5. The model from which the experimental data were obtained had a small fuselage which served as a balance housing. For this analysis, wing section ordinates in the vicinity of the root chord were altered to approximate the fuselage area distribution. Generally, the new method works as well for this wing as it did for the aspect-ratio-2 wing with its 63.43° leading-edge sweep. Data for this wing at $M_\infty = 2.3$ and $\alpha = 19.94^\circ$ illustrate how the vacuum limit in addition to the pressure distribution spreading tends to limit the vortex contribution. The present method predicts pressures which approach the vacuum pressure limit $-2/\gamma M^2$ for the leading edge of both lower and upper surface at $M_\infty = 2.3$ and $M_\infty = 3.5$. This indicates the large influence of the wing sidewash for wings with subsonic leading edges, an effect which seems to be overestimated at the largest angle of attack.

Force data for the 76° swept leading-edge wing (from ref. 15) are shown in figure 6. As mentioned previously, the theoretical drag coefficients (and axial-force coefficients) are matched to the experimental data at $\alpha = 0^\circ$. For all the coefficients, differences among linearized-theory results, the present method, and the experimental data are small. For uncambered delta wings, linearized theory has been observed to provide reasonable estimates of overall forces and moments in spite of occasional large discrepancies in local loadings. Where differences between linearized theory and the present method occur, the present method is generally in better agreement with the experimental data.

The next set of data to be examined is for a series of arrow wings with differing degrees of camber surface severity. The arrow-wing planform offers an opportunity to compare experiment and theory for a case in which linearized theory fails in pitching-moment prediction. The camber surface or design lift-coefficient series offers an opportunity to explore a situation in which the linearized theory fails to assess the drag penalties associated with camber surfaces having large variations in local slope.

Pressure data (ref. 16) for a series of 70° swept leading-edge arrow wings with design lift coefficients of 0, 0.08, and 0.16 for $M_\infty = 2.05$ are shown in figure 7. The angle-of-attack range covered by these data is small compared with that of the previous data, and thus, significant differences between the present method and linearized theory occur primarily at the outboard wing stations. There, the prediction given by the new method provides a better estimate of the pressure loadings than does the linearized theory.

Force data (ref. 17) for the same series of wings are shown in figure 8. For the uncambered wing (fig. 8(a)), the present system provides a better estimate of the axial force, the normal force, and the pitching moment. Somewhat surprisingly, this does not result in a necessarily improved prediction of the drag or the lift-drag ratio. However, the differences between the linearized theory, the present method, and the experimental data are small. For the cambered wings, and particularly for the $C_{L,D} = 0.16$ wing, the present method provides an improvement in prediction of all the coefficients, except possibly C_A. In assessment of the apparent C_A discrepancies, possible experimental sources of error must be considered. The test models were half-span wings mounted on a boundary-layer-bypass plate with a gap between the plate and the wing except at the point of attachment to the balance. Because of the nature of the force distribution, as indicated by sketch (o), a leakage through the

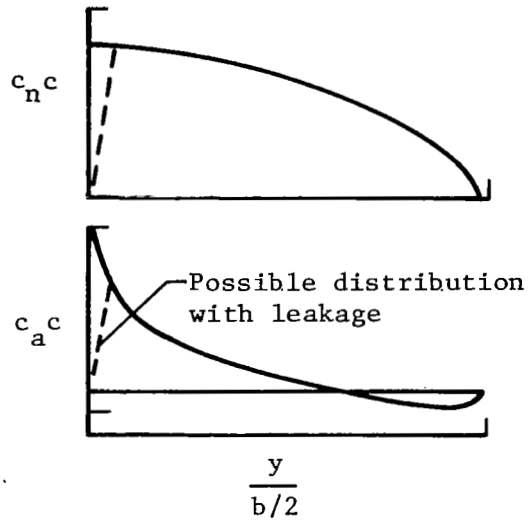

Sketch (o)

gap could cause a sizable decrease in axial force without an appreciable effect on the normal force. Some simple calculations in which such a loss in axial force is assumed to be concentrated at the root chord show a negligible effect on the lift-drag polar and the lift-drag ratio. The lift-drag polars and the lift-drag ratio plots in the three parts of figure 8 show the capability of the new method to predict with reasonable accuracy the drag penalties of increasing camber surface severity. Thus, this system could be used in design by iteration procedures to select optimum design coefficients, information heretofore available only through wind-tunnel experimentation.

In spite of the theoretically sharp leading edges of these wings (3-percent-circular-arc sections), there is evidence of a small amount of leading-edge thrust. An assumed leading-edge radius of 0.06 mm (0.4 percent of the wing root chord maximum thickness) along the entire leading edge was found to be sufficient to explain the difference between the experimental and theoretical axial forces

for the flat wing. Estimation of effective leading-edge radii for theoretically sharp leading-edge wing sections poses a difficult problem.

Data from reference 18 for a series of twisted and cambered wings covering a range of leading-edge sweep angles are shown in figures 9 to 11. Generally, the present method gives an improved prediction over linearized theory for all the aerodynamic force and moment coefficients. The new method shows poorest performance for the highly twisted and cambered wing with the 75.96° swept leading edge, where the axial force is uniformly overestimated by about 0.0015 (fig. 9(c)).

Figure 12 permits a comparison of the predicted and measured variation of the maximum lift-drag ratio and the pitching-moment coefficient at zero lift with the wing design lift coefficient. These data illustrate the use of the newer system in the selection of design lift coefficient (camber surface severity) for maximization of performance benefits. Only for the 75.96° swept wing ($\beta \cot \Lambda = 0.6$) is the present method misleading. Here an optimum design lift coefficient of about 0.03 or 0.04 is indicated, whereas the experimental optimum is probably about 0.06.

The effect of camber surface severity on the aerodynamic performance of a 70° swept leading-edge arrow wing and a 75° swept leading-edge arrow wing is shown in figures 13 and 14. The data for the design condition $M_\infty = 2.05$ are taken from reference 17. The data for the off-design Mach numbers of 1.61 and 2.20 are from reference 19. The differences between the maximum lift-drag ratios predicted by the linearized theory and those predicted by the present method are shown to be quite large; in general, the present method predicts the measured variation with design lift coefficient reasonably well.

A similar plot for data from reference 15 is shown in figure 15. Here, the design condition is $M_\infty = 3.5$ and the off-design conditions are $M_\infty = 2.3$ and $M_\infty = 4.6$. For the design condition and for the higher Mach number, wing twist and camber offers little or no benefit except as a means of moment control. For the lower Mach number, there is a small improvement in $(L/D)_{max}$ for $C_{L,D} = 0.05$. These trends are shown to be represented with reasonable accuracy by the present method. The experimental pitching moment for the 0.05 design lift-coefficient wing at all three Mach numbers is believed to be an error.

Taken as a whole, the data of figures 12 to 15 illustrate the decreasing effectiveness of twist and camber in aerodynamic performance optimization as the Mach number increases. These data also demonstrate the inability of basic linearized-theory methods to provide valid information for the selection of the design parameters, a need which is met to a much higher degree by the present method.

Force coefficient data from reference 20 for a wing-body configuration which displays evidence of appreciable leading-edge thrust are shown in figure 16. The aspect-ratio-2 uncambered wing has a 5-percent-thick NACA 0005-63 section with a leading-edge radius of 5.6 percent of the section maximum thickness. The amount of leading-edge thrust achieved, as indicated by the axial-force coefficient, is predicted with reasonable accuracy by the present method.

The present-method curve labeled "No thrust" indicates the axial force predicted by the present method when the leading-edge thrust force is ignored, and C_A is determined only from program-calculated pressures acting on the wing upper and lower surfaces. Results from linearized theory for full thrust and no thrust show the large theoretical performance differences due to the thrust phenomenon. The present-method curves for C_A, C_D, and L/D indicate a gradual transition from nearly full thrust below about 3^o to smaller and smaller fractions of the full thrust as angle of attack increases. The $M_\infty = 1.3$ data are at about the lower Mach number limit for practical application of the method. Here, the deflection angle for sonic flow is 6.32^o.

In the next comparison of theory and experiment, a very generalized case is treated. The wing for this example had an arbitrary planform with a curved leading edge and employed a twisted and cambered mean lifting surface. In addition, the wing sections had a rounded leading edge, so that some degree of leading-edge thrust could be expected where the local leading edge is subsonic. In figure 17, experimental data for this wing (ref. 21) are compared with predictions given by the present method. Generally, the nonlinear prediction method agrees well with the experimental data. Of particular interest are the nonlinearities in the axial force and the pitching moment. As indicated by the axial force, this model displays significant leading-edge thrust, somewhat more than is predicted by the present method. The implications of this phenomenon for the design of high-performance wings for supersonic cruise are discussed in reference 22.

The final comparison of theory and experiment is for a high-efficiency supersonic cruise configuration that has been seriously considered in the National Supersonic Transport Program. Data from reference 23 for a wing-body version of this configuration are shown in figure 18. For the program representation, the fuselage and the wing were considered as a single unit. As shown in the schematic semispan representation in sketch (p), the fuselage, as well as

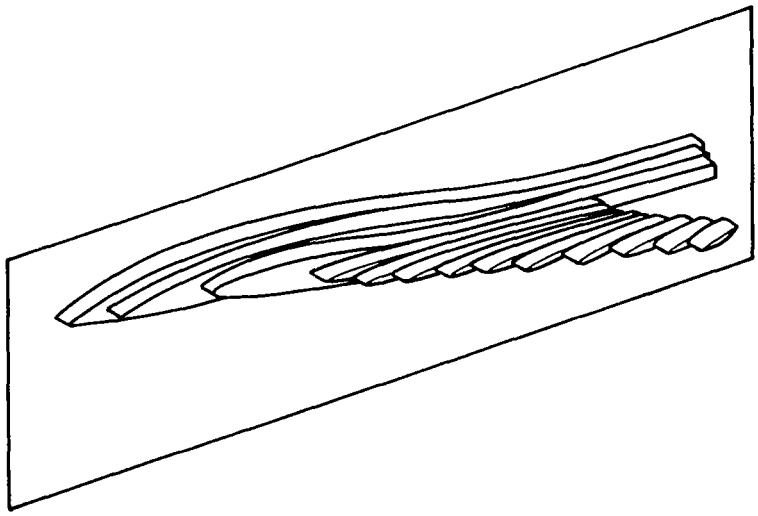

Sketch (p)

the wing, was used in definition of the wing planform and the chordwise thickness and camber distributions. In this comparison, $C_{D,o}$ (0.0074) was estimated by the linearized-theory methods of reference 2, and if that value is correct, this example provides a test of the ability of the present method to predict camber drag. As shown in figure 18, the present method gives a much improved estimate of the moment characteristics relative to linearized theory; however, the estimate of the drag and the lift-drag ratio leave something to be desired. The error is clearly due to the axial-force estimate, in which the camber drag is overestimated. This configuration is a quite complex wing-fuselage arrangement with a considerable amount of favorable mutual interaction for both volume and lift. The geometry used in the analysis (sketch (q)) may

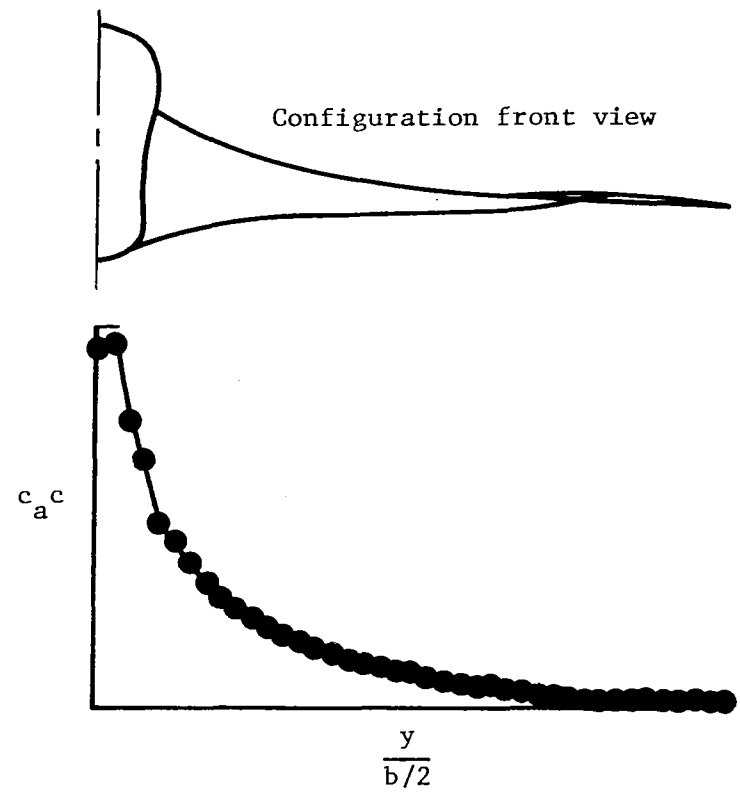

Sketch (q)

be incapable of adequately accounting for some of the design subtleties. For this configuration, with a fuselage extending well forward and aft of the wing itself, the strategy of considering wing and fuselage as a unit did, however, offer some improvements over a wing-alone treatment (not shown here), a better moment correlation, and a 0.13 increase in $(L/D)_{max}$, for example. The dominance of fuselage and wing-root-chord region in the axial-force distribution for 0° angle of attack is shown in sketch (q). The use of the present-method correction schemes in conjunction with the more accurate surface panel linearized-theory methods now being developed might offer a solution to this

problem. For such an application, it might be necessary to base the pressure correction for the fuselage on a tangent conical surface rather than on the tangent plane surface as used here for the wing.

The present study has led to some observations on wing design philosophy. It has been the practice to design wing lifting surfaces by use of linearized-theory methods such as those of reference 1. Some allowance is usually made for the inability of linearized theory to assess camber surface drag penalties adequately. For example, a design lift coefficient of about eight-tenths of the estimated cruise lift coefficient was used for the configuration of figure 18. However, no rational basis other than "rule of thumb" for selection of camber surface severity for performance optimization exists. In addition, it has been the practice to discount the possibility of any attainment of leading-edge thrust, a factor which also has a bearing on the choice of design lift coefficient.

Figure 19 helps to illustrate how the present method of estimation can be used as an aid in the choice of the camber surface. Maximum lift-drag ratios are shown as a function of design lift coefficient for both wind-tunnel and assumed flight conditions. Linearized-theory estimates are shown at the top of the figure and present-method estimates at the center and bottom.

If only linearized theory were available as a guide for selection of the design parameter, the choice would clearly be a design lift coefficient equal to the cruise lift coefficient. Only rules of thumb based on wind-tunnel experience give lower values which may approach the real optimum. The present method, on the other hand, indicates a design lift coefficient of about 0.04 to 0.05 for optimization of cruise efficiency if leading-edge thrust is discounted and a value of about 0.02 to 0.03 for the estimated attainable thrust. It also predicts a much less sensitive dependence of the maximum lift-drag ratio on the design lift coefficient. Both a more realistic estimate of the camber drag penalties and a consideration of attainable thrust benefits tend to favor milder camber surfaces approaching the uncambered or flat wing.

Now, given the situation in which some limited experimental data are available, as in the case here, the present-method camber surface penalties for this configuration are shown to be too severe. The present-method curve, however, may be useful in providing an estimate of the variation of the actual lift-drag ratio (assumed to be represented by the experimental data and an extrapolation thereof) with the camber surface severity. First, it is assumed that the maximum lift-drag ratio for the flat wing ($C_{L,D} = 0$) is predicted with reasonable accuracy. Then, a reasonable estimate of the variation between these points may be made by adjusting or rotating the present-method curve to pass through both points. This adjustment appears to be justified by an examination of the experimental theoretical correlations of figures 12 to 15. This estimated variation of attainable lift-drag ratio with design lift coefficient indicates that an improvement in $(L/D)_{max}$ of 0.12 in the wind tunnel and 0.20 in flight could result from a reduction in design lift coefficient from 0.08 to about 0.04 to 0.05. The maximum lift-drag ratio for this milder camber surface occurs at a lift coefficient very close to the anticipated cruise lift coefficient of 0.10. The resultant reduction in root chord angle of attack and cabin floor angle would also be beneficial. Trim drag considerations, however, might prevent

taking full advantage of the reduced camber surface severity. In consideration of the moment characteristics in trade-off studies, the present method, with its improved estimates of pitching moments, would obviously be helpful.

Although a fuselage may be treated as part of a more generalized wing shape, the method as formulated here is basically a wing-alone program. For more complete configurations, results from this method must be combined with results from established linearized-theory methods (refs. 2 to 5, for example). The substitution of an uncambered configuration $C_{D,o}$ evaluated by other methods for the $C_{D,o}$ given by the present method has already been discussed. This substitution permits an account of the contribution to $C_{D,o}$ of the thickness drag of other components and the skin friction drag as well. For configurations with secondary lifting surfaces (horizontal tails and canards) another adjustment could be made. Incremental changes to C_L, C_D, and C_m for each angle of attack could be evaluated as the difference between linearized-theory solutions for complete configurations and a wing-alone configuration. This difference could then be added to the nonlinear results.

CONCLUDING REMARKS

A computational system for estimation of nonlinear aerodynamic characteristics of wings at supersonic speeds has been developed and has been implemented in a computer program entitled "Supersonic Wing Nonlinear Aerodynamics" described more fully in the section "Computer Program." The corrected linearized-theory method accounts for nonlinearities in the variation of basic pressure loadings with local surface slopes, predicts the degree of attainment of theoretical leading-edge thrust forces, and provides an estimate of detached leading-edge vortex loadings that result when the theoretical thrust forces are not fully realized.

Comparisons of estimates given by the present method with experimental results show significant improvements in detailed wing pressure distributions over those given by linearized theory, particularly for large angles of attack and for regions of the wing where the flow is highly three-dimensional. The new method also provides generally improved predictions of the wing overall force and moment coefficients. Of particular importance are the more accurate prediction of pitching moment and the more realistic estimate of the variation of drag with camber surface severity as dictated by the design lift coefficient. This latter capability should prove useful in the conduct of design studies aimed at aerodynamic performance optimization. The new method should also provide more realistic trade-off information for selection of wing planform geometry and airfoil section parameters.

Langley Research Center
National Aeronautics and Space Administration
Hampton, VA 23665
August 22, 1980

REFERENCES

1. Carlson, Harry W.; and Miller, David S.: Numerical Methods for the Design and Analysis of Wings at Supersonic Speeds. NASA TN D-7713, 1974.

2. Middleton, W. D.; and Lundry, J. L.: A Computational System for Aerodynamic Design and Analysis of Supersonic Aircraft. Part 1 - General Description and Theoretical Development. NASA CR-2715, 1976.

3. Middleton, W. D.; Lundry, J. L.; and Coleman, R. G.: A Computational System for Aerodynamic Design and Analysis of Supersonic Aircraft. Part 2 - User's Manual. NASA CR-2716, 1976.

4. Middleton, W. D.; Lundry, J. L.; and Coleman, R. G.: A Computational System for Aerodynamic Design and Analysis of Supersonic Aircraft. Part 3 - Computer Program Description. NASA CR-2717, 1976.

5. Woodward, F. A.: An Improved Method for the Aerodynamic Analysis of Wing-Body-Tail Configurations in Subsonic and Supersonic Flow. NASA CR-2228, Pts. I and II, 1973.
   Part I - Theory and Application.
   Part II - Computer Program Description.

6. Carlson, Harry W.: A Modification to Linearized Theory for Prediction of Pressure Loadings on Lifting Surfaces at High Supersonic Mach Numbers and Large Angles of Attack. NASA TP-1406, 1979.

7. Carlson, Harry W.; and Mack, Robert J.: Estimation of Leading-Edge Thrust for Supersonic Wings of Arbitrary Planform. NASA TP-1270, 1978.

8. Carlson, Harry W.; Mack, Robert J.; and Barger, Raymond L.: Estimation of Attainable Leading-Edge Thrust for Wings at Subsonic and Supersonic Speeds. NASA TP-1500, 1979.

9. Carlson, Harry W.; and Mack, Robert J.: Studies of Leading-Edge Thrust Phenomena. AIAA-80-0325, Jan. 1980.

10. Polhamus, Edward C.: Predictions of Vortex-Lift Characteristics by a Leading-Edge Suction Analogy. J. Aircr., vol. 8, no. 4, Apr. 1971, pp. 193-199.

11. Boatright, William B.: Experimental Study and Analysis of Loading and Pressure Distributions on Delta Wings Due to Thickness and to Angle of Attack at Supersonic Speeds. NACA RM L56I14, 1956.

12. Michael, William H., Jr.: Flow Studies on Drooped-Leading-Edge Delta Wings at Supersonic Speed. NACA TN 3614, 1956.

13. Kaattari, George E.: Pressure Distributions on Triangular and Rectangular Wings to High Angles of Attack - Mach Numbers 1.45 to 1.97. NACA RM A54D19, 1954.

14. Kaattari, George E.: Pressure Distributions on Triangular and Rectangular Wings to High Angles of Attack - Mach Numbers 2.46 and 3.36. NACA RM A54J12, 1955.

15. Sorrells, Russell B., III; and Landrum, Emma Jean: Theoretical and Experimental Study of Twisted and Cambered Delta Wings Designed for a Mach Number of 3.5. NASA TN D-8247, 1976.

16. Carlson, Harry W.: Pressure Distributions at Mach Number 2.05 on a Series of Highly Swept Arrow Wings Employing Various Degrees of Twist and Camber. NASA TN D-1264, 1962.

17. Carlson, Harry W.: Aerodynamic Characteristics at Mach Number 2.05 of a Series of Highly Swept Arrow Wings Employing Various Degrees of Twist and Camber. NASA TM X-332, 1960.

18. Mack, Robert J.: Effects of Leading-Edge Sweep Angle and Design Lift Coefficient on Performance of a Modified Arrow Wing at a Design Mach Number of 2.6. NASA TN D-7753, 1974.

19. Middleton, Wilbur D.; and Sorrells, Russell B.: Off-Design Aerodynamic Characteristics at Mach Numbers 1.61 and 2.20 of a Series of Highly Swept Arrow Wings Designed for Mach Number 2.0 Employing Various Degrees of Twist and Camber. NASA TN D-1630, 1963.

20. Hall, Charles F.: Lift, Drag, and Pitching Moment of Low-Aspect-Ratio Wings at Subsonic and Supersonic Speeds. NACA RM A53A30, 1953.

21. Robins, A. Warner; Lamb, Milton; and Miller, David S.: Aerodynamic Characteristics at Mach Numbers of 1.5, 1.8, and 2.0 of a Blended Wing-Body Configuration With and Without Integral Canards. NASA TP-1427, 1979.

22. Robins, A. Warner; and Carlson, Harry W.: High-Performance Wings With Significant Leading-Edge Thrust at Supersonic Speeds. AIAA Paper 79-1871, Aug. 1979.

23. Morris, Odell A.; Fuller, Dennis E.; and Watson, Carolyn B.: Aerodynamic Characteristics of a Fixed Arrow-Wing Supersonic Cruise Aircraft at Mach Numbers of 2.30, 2.70, and 2.95. NASA TM-78706, 1978.

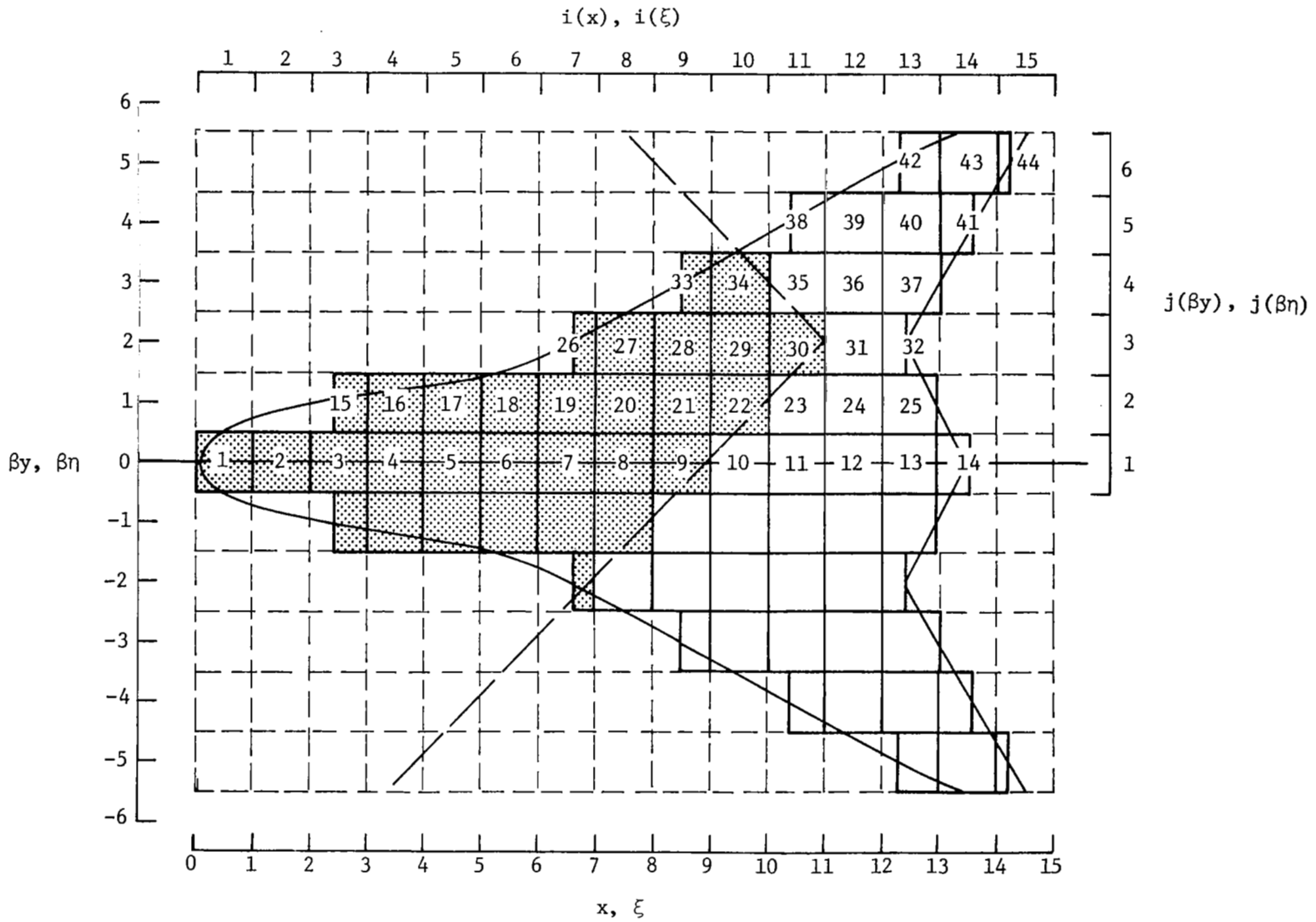

Figure 1.- Grid system used in numerical solution of linearized theory.

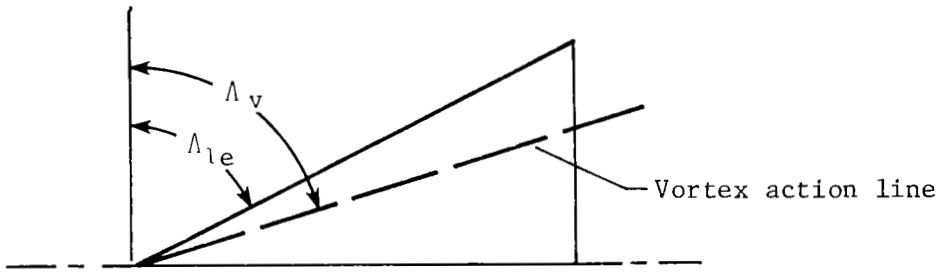

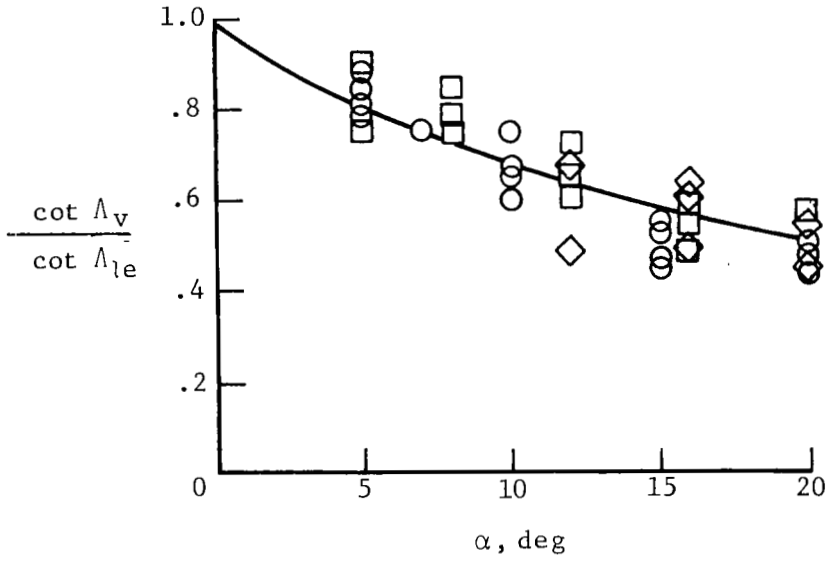

○ Flat delta wings, C_p data, ref. 11
M_∞ = 1.62 to 2.41
$\beta \cot \Lambda_{le}$ = 0.55 to 0.96

□ Drooped leading-edge delta wings, C_p data, ref. 12
M_∞ = 1.9
$\beta \cot \Lambda_{le}$ = 0.43 to 1.0

◇ Drooped leading-edge delta wings, vapor screen data, ref. 12
M_∞ = 1.9
$\beta \cot \Lambda_{le}$ = 0.43 to 1.0

——— Curve fit

Figure 2.- Experimental location of vortex action line for delta wings.

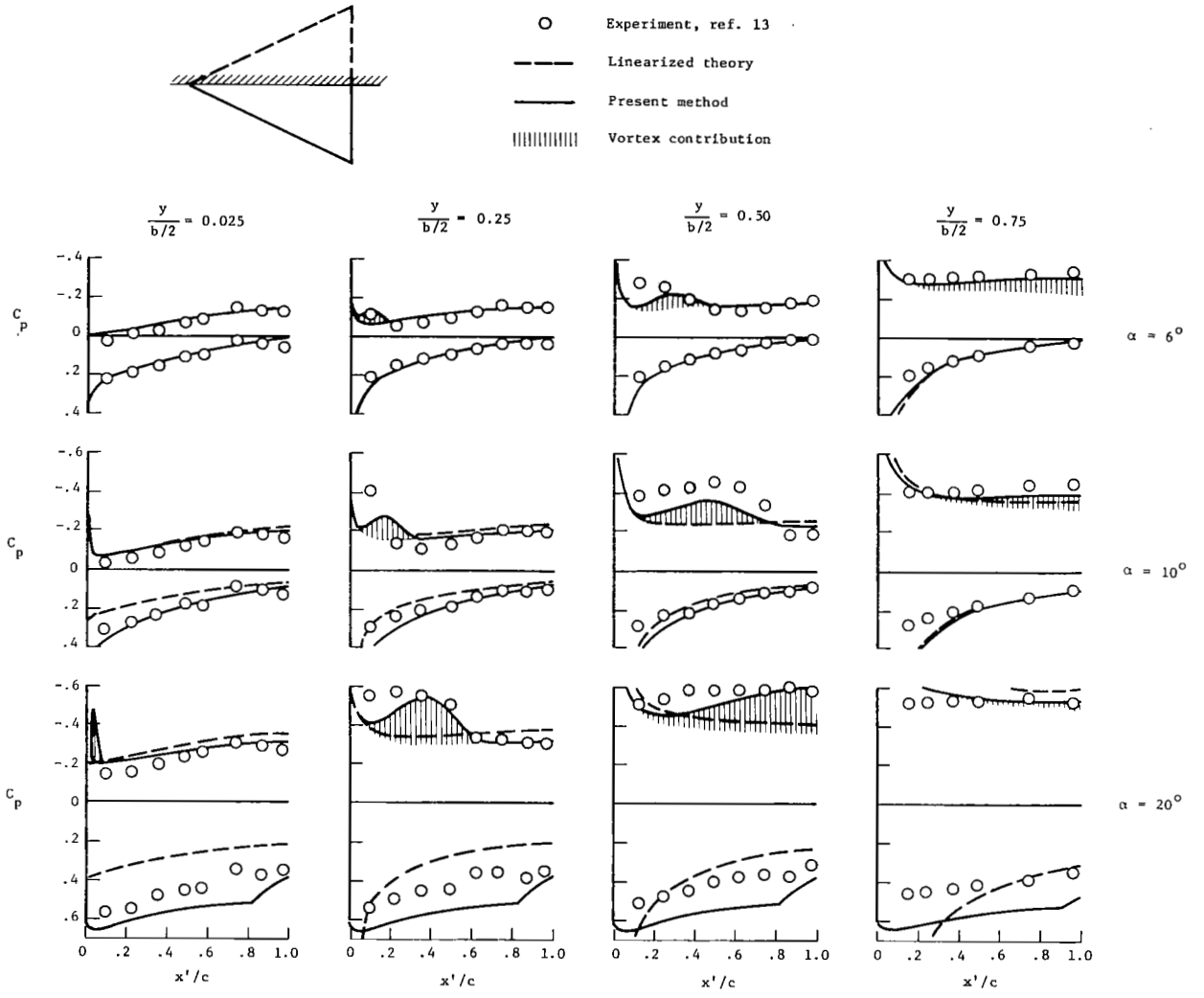

(a) $M_\infty = 1.45$.

Figure 3.- Comparison of predicted and measured pressure distributions for uncambered delta wing of aspect ratio 2.

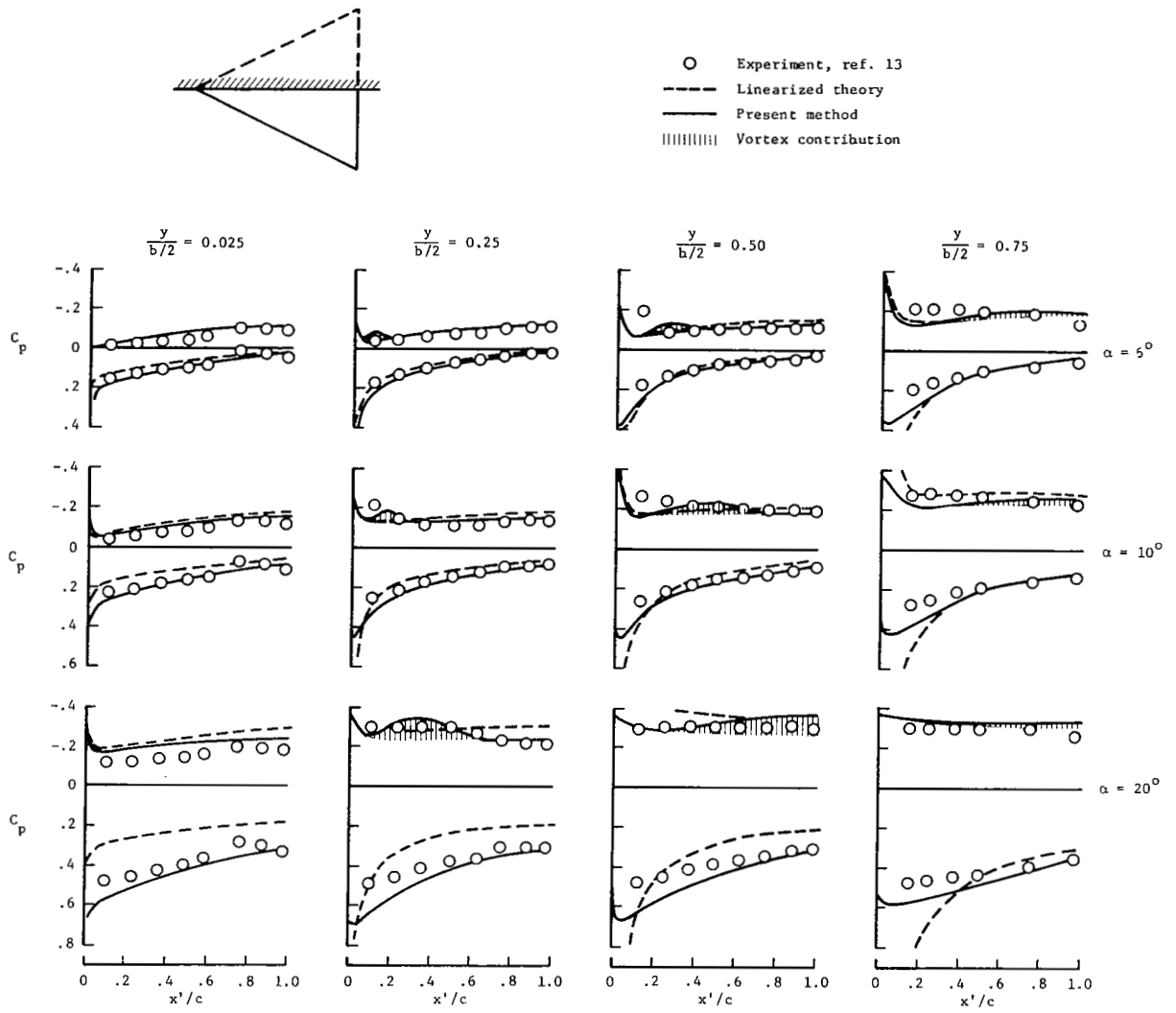

(b) $M_\infty = 1.97$.

Figure 3.- Continued.

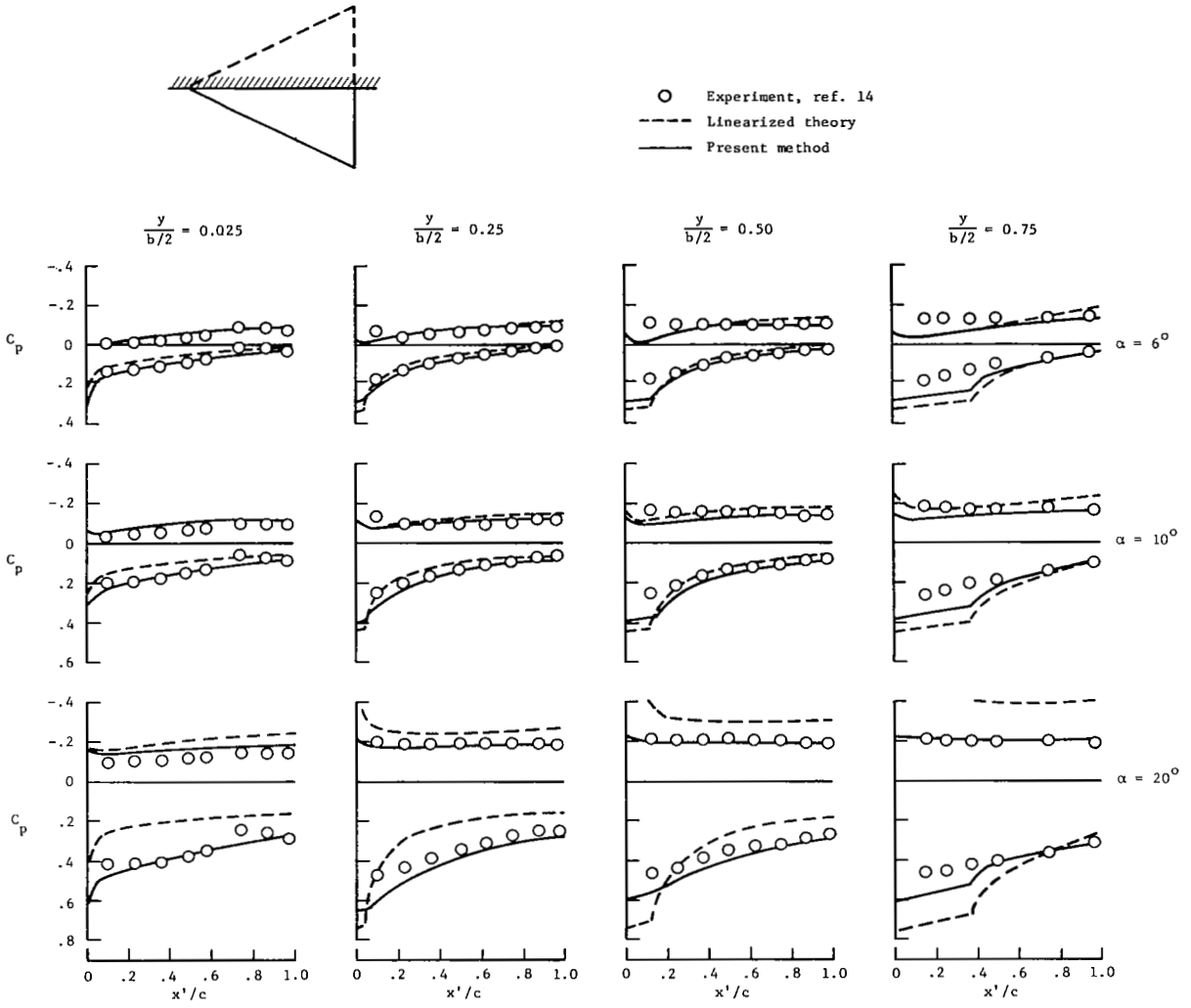

(c) $M_\infty = 2.46$.

Figure 3.- Continued.

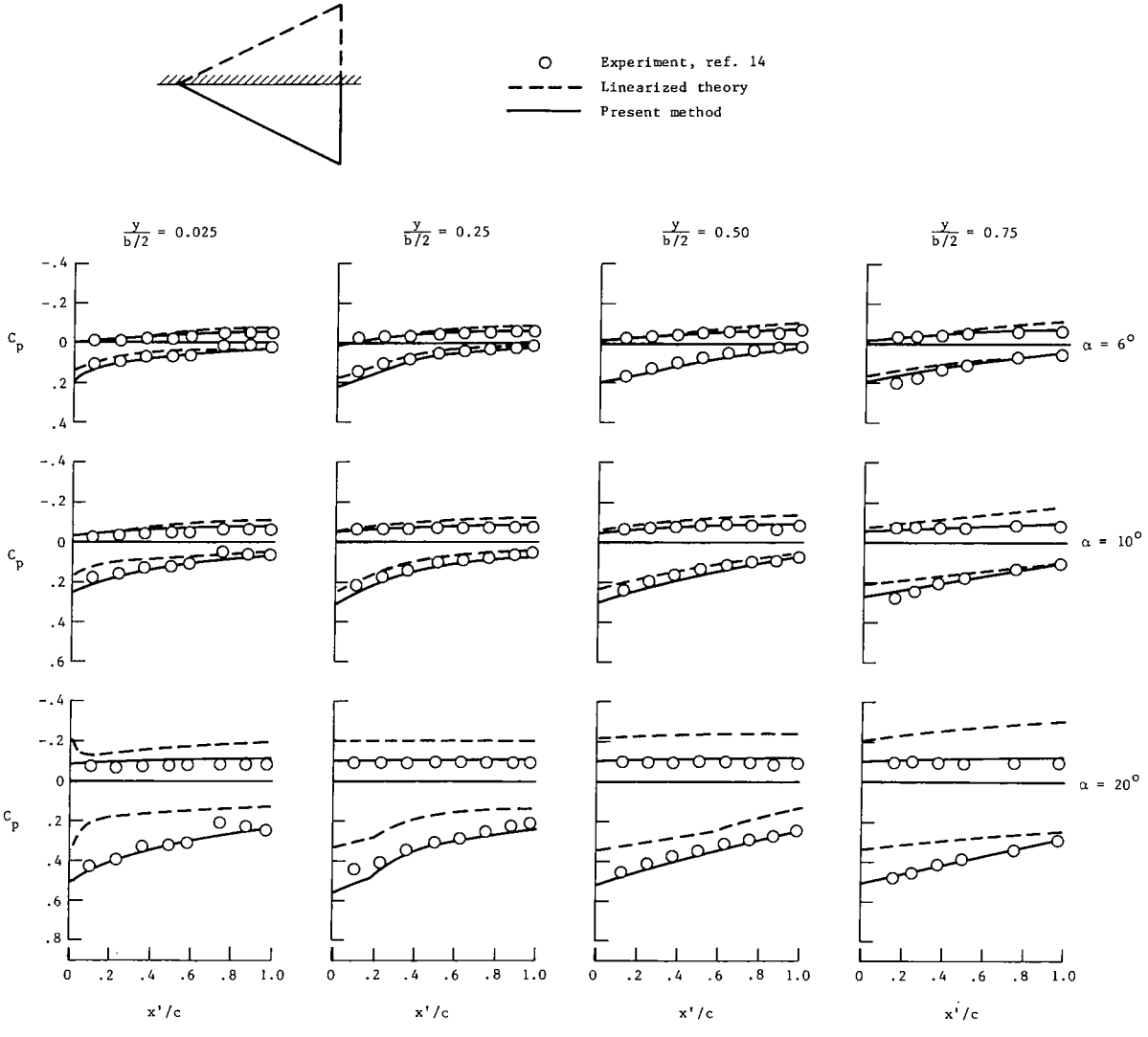

(d) $M_\infty = 3.36$.

Figure 3.- Concluded.

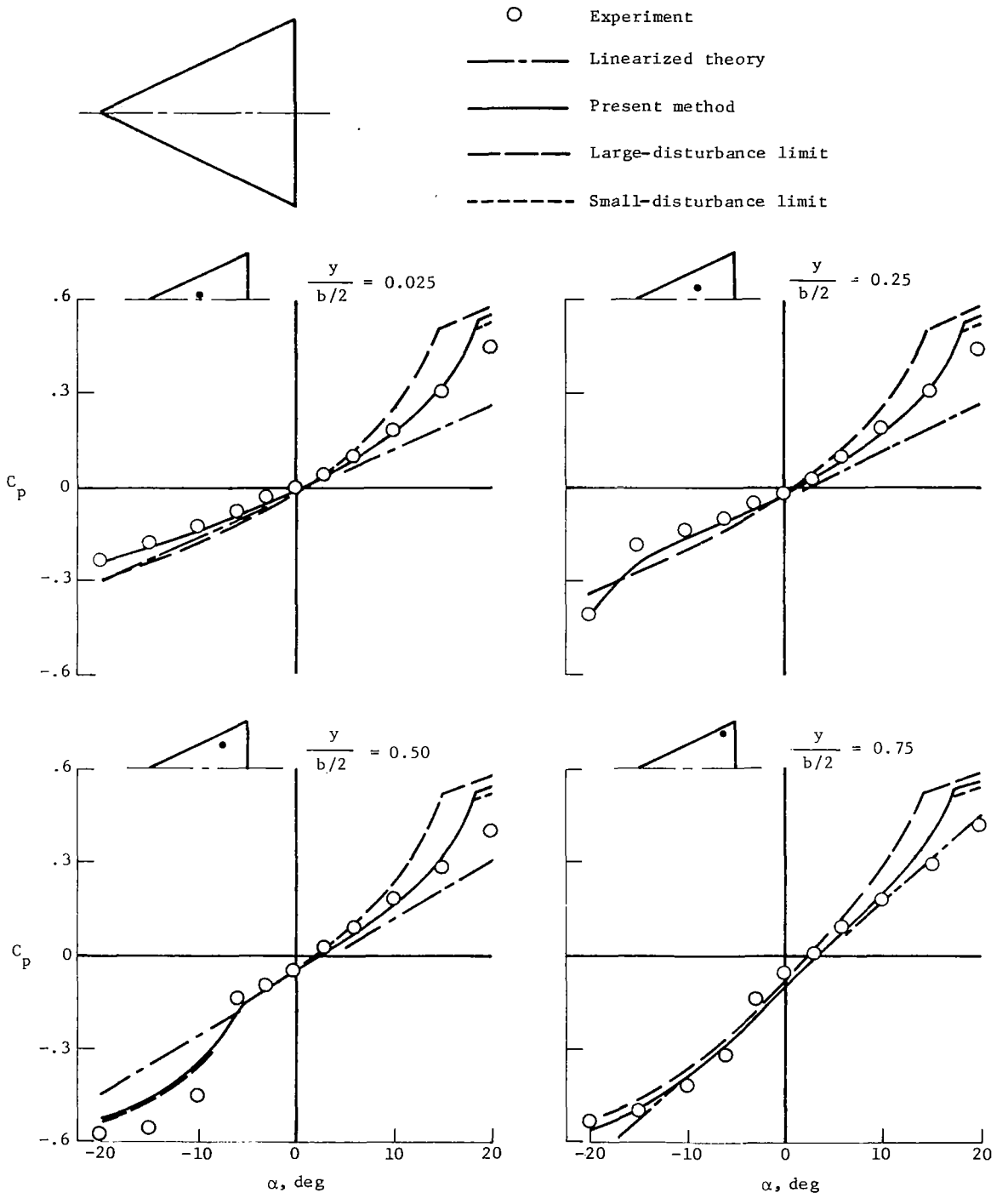

(a) $M_\infty = 1.45$.

Figure 4.- Boundaries of present method imposed by small- and large-disturbance formulations.

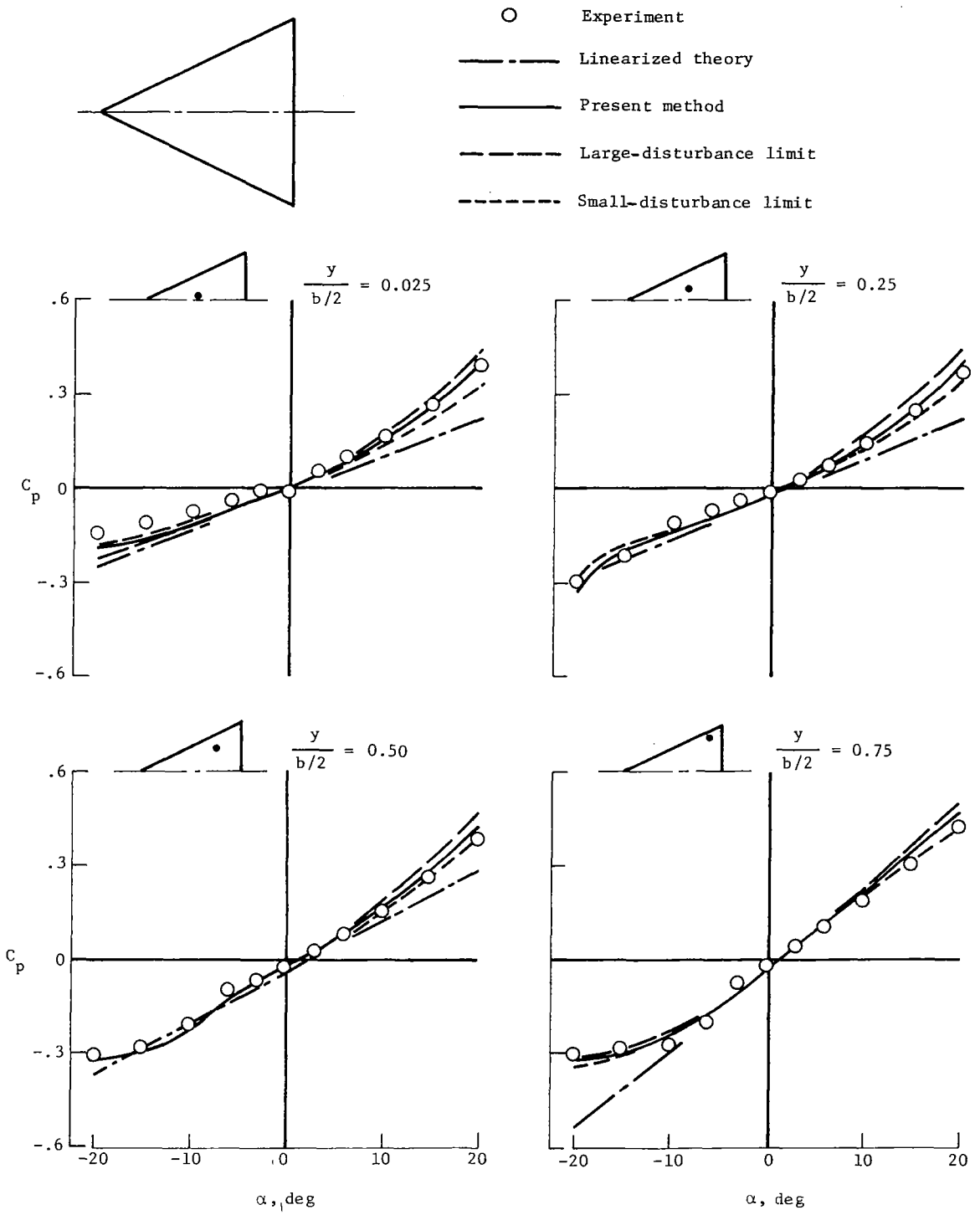

(b) $M_\infty = 1.97$.

Figure 4.- Continued.

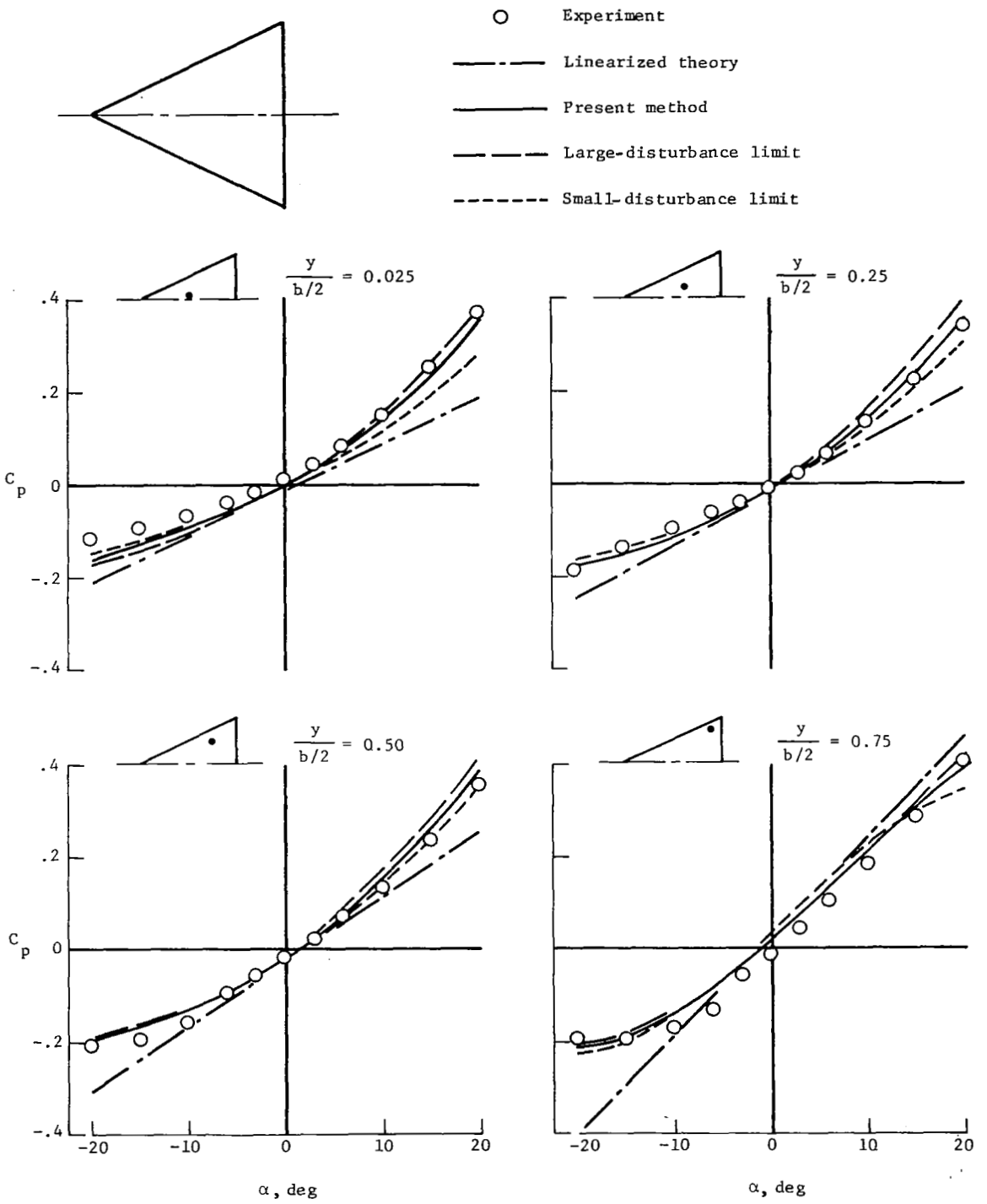

(c) $M_\infty = 2.46$.

Figure 4.- Continued.

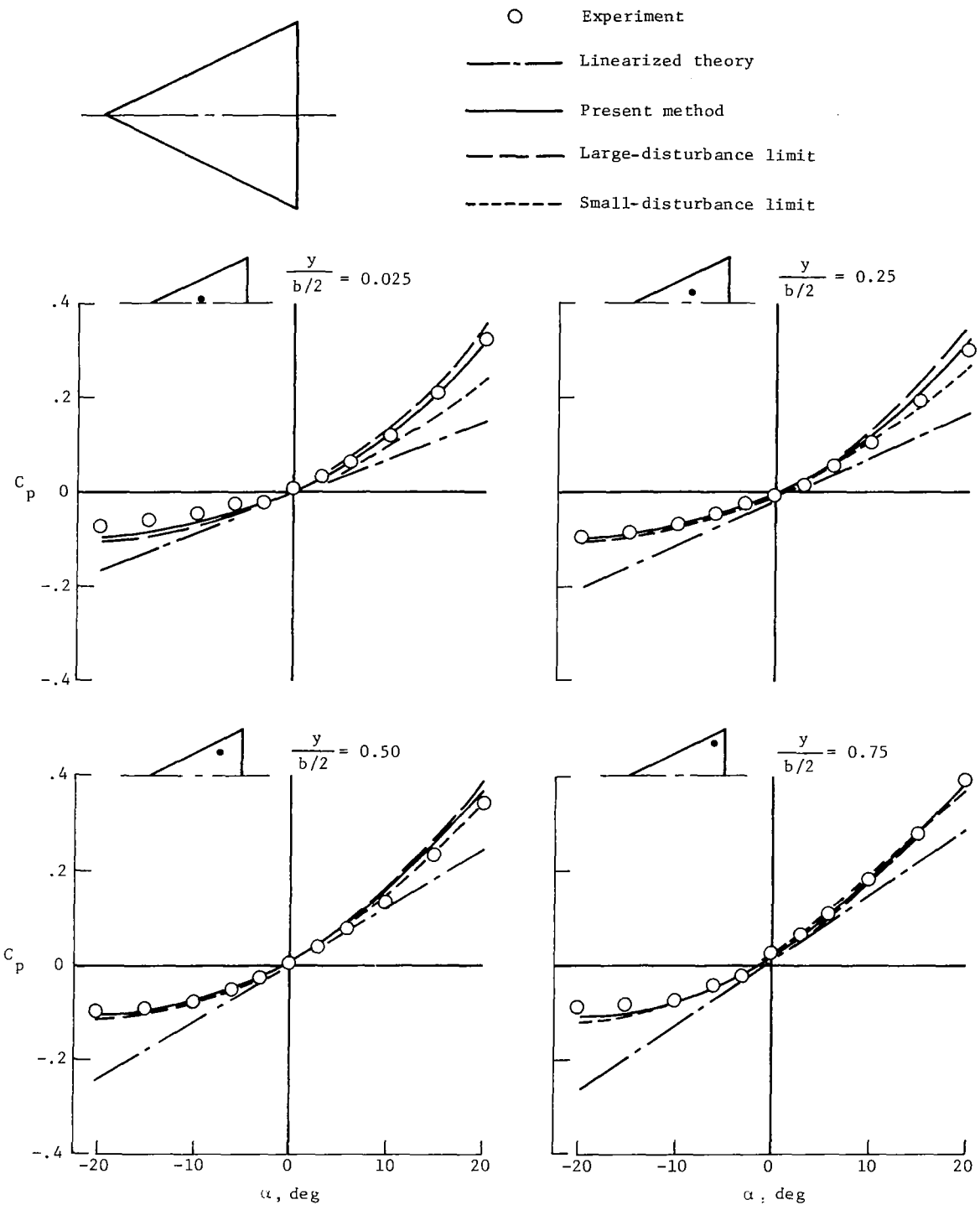

(d) $M_\infty = 3.36$.

Figure 4.- Concluded.

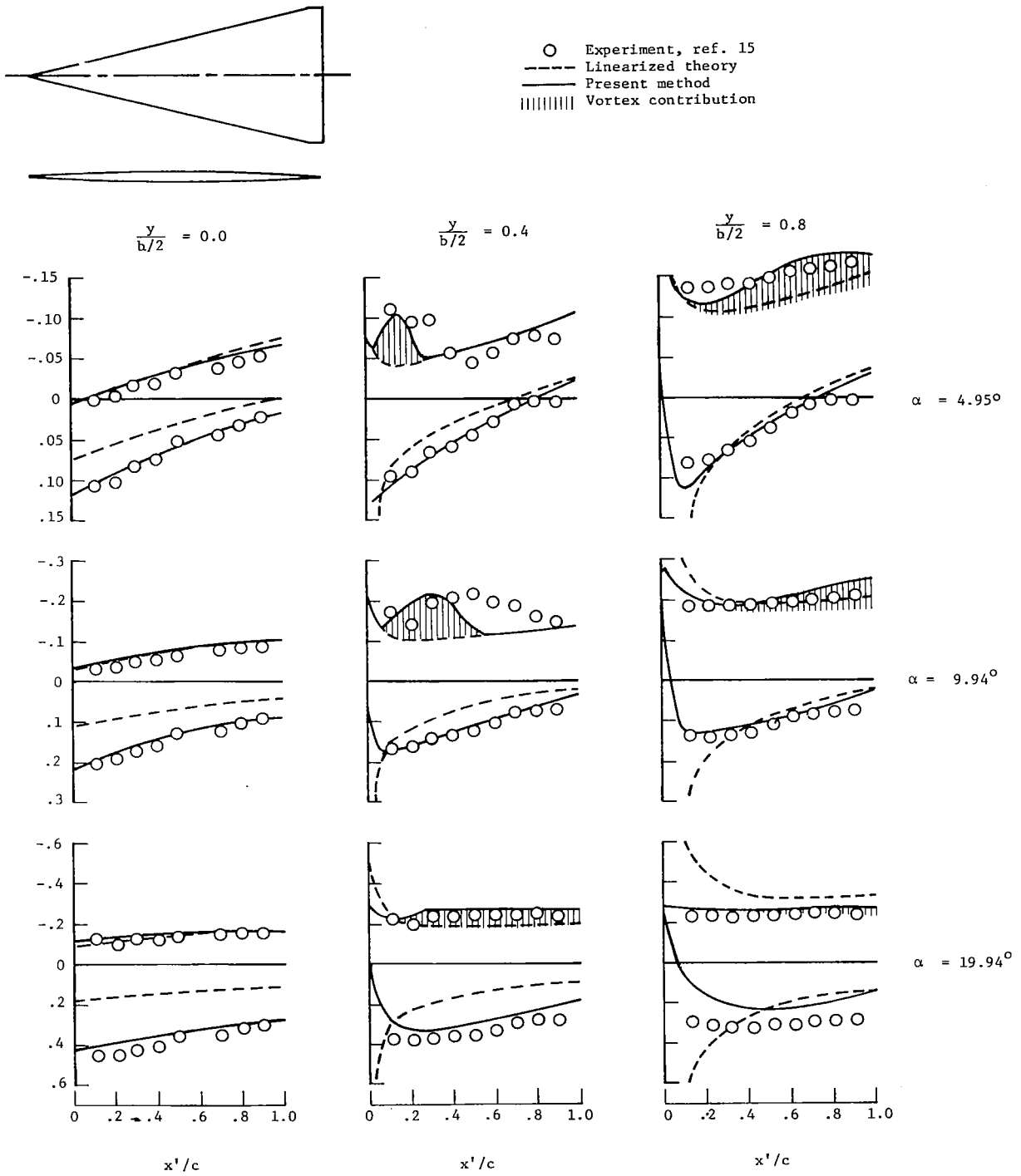

(a) $M_\infty = 2.3$.

Figure 5.- Comparison of predicted and measured pressure distributions for uncambered 76° swept leading-edge delta wing.

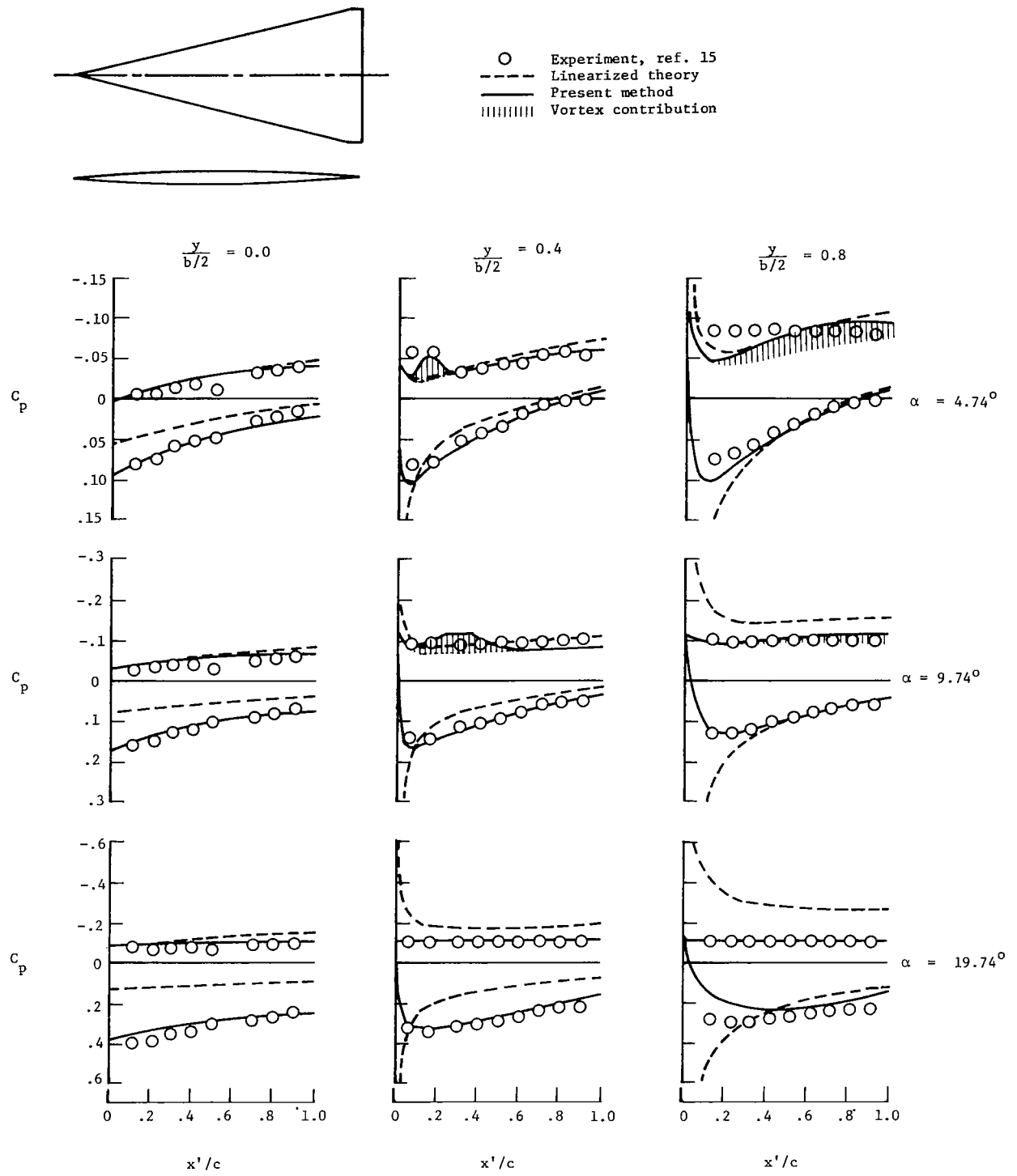

(b) $M_\infty = 3.5$.

Figure 5.- Continued.

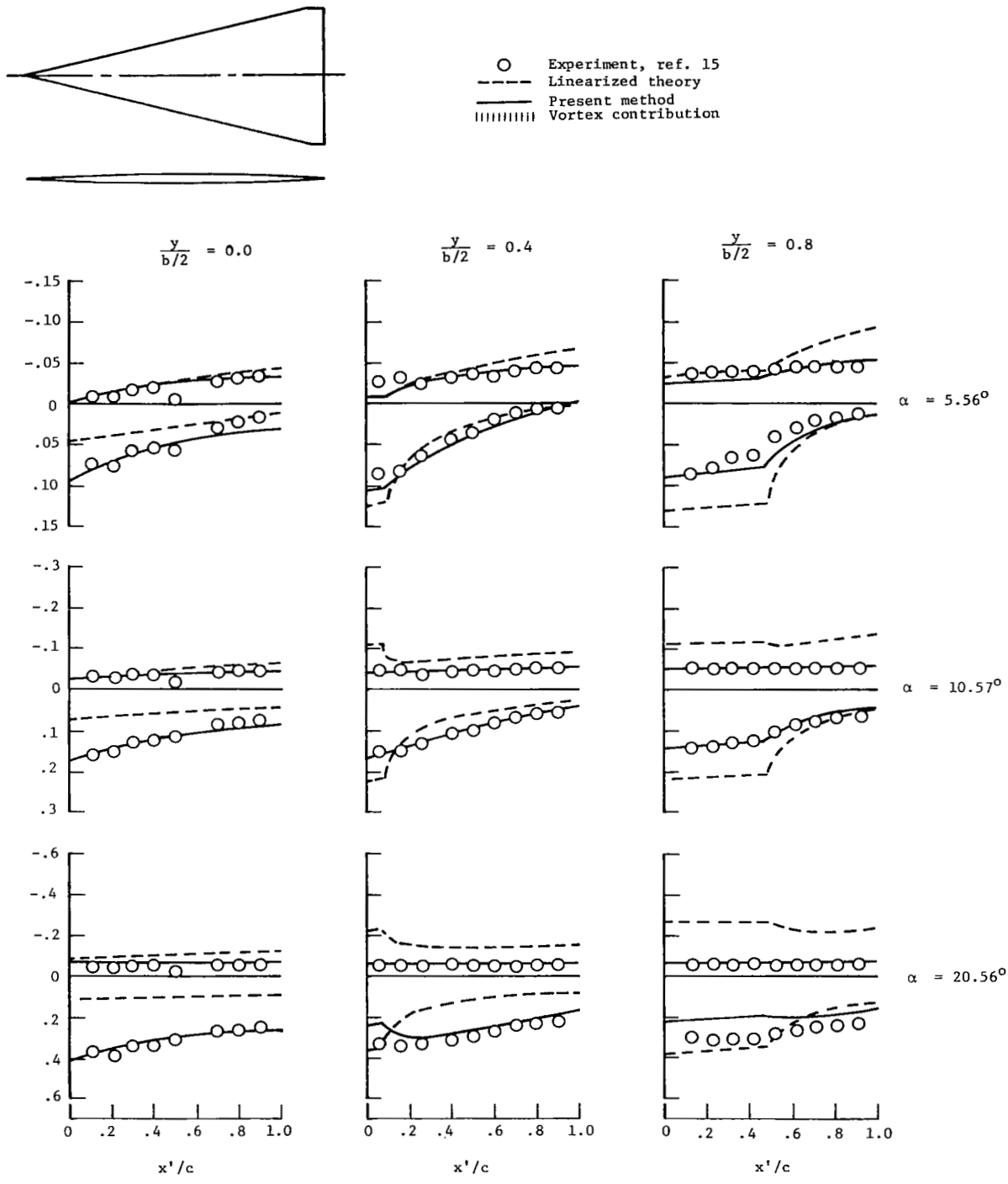

(c) $M_\infty = 4.6$.

Figure 5.- Concluded.

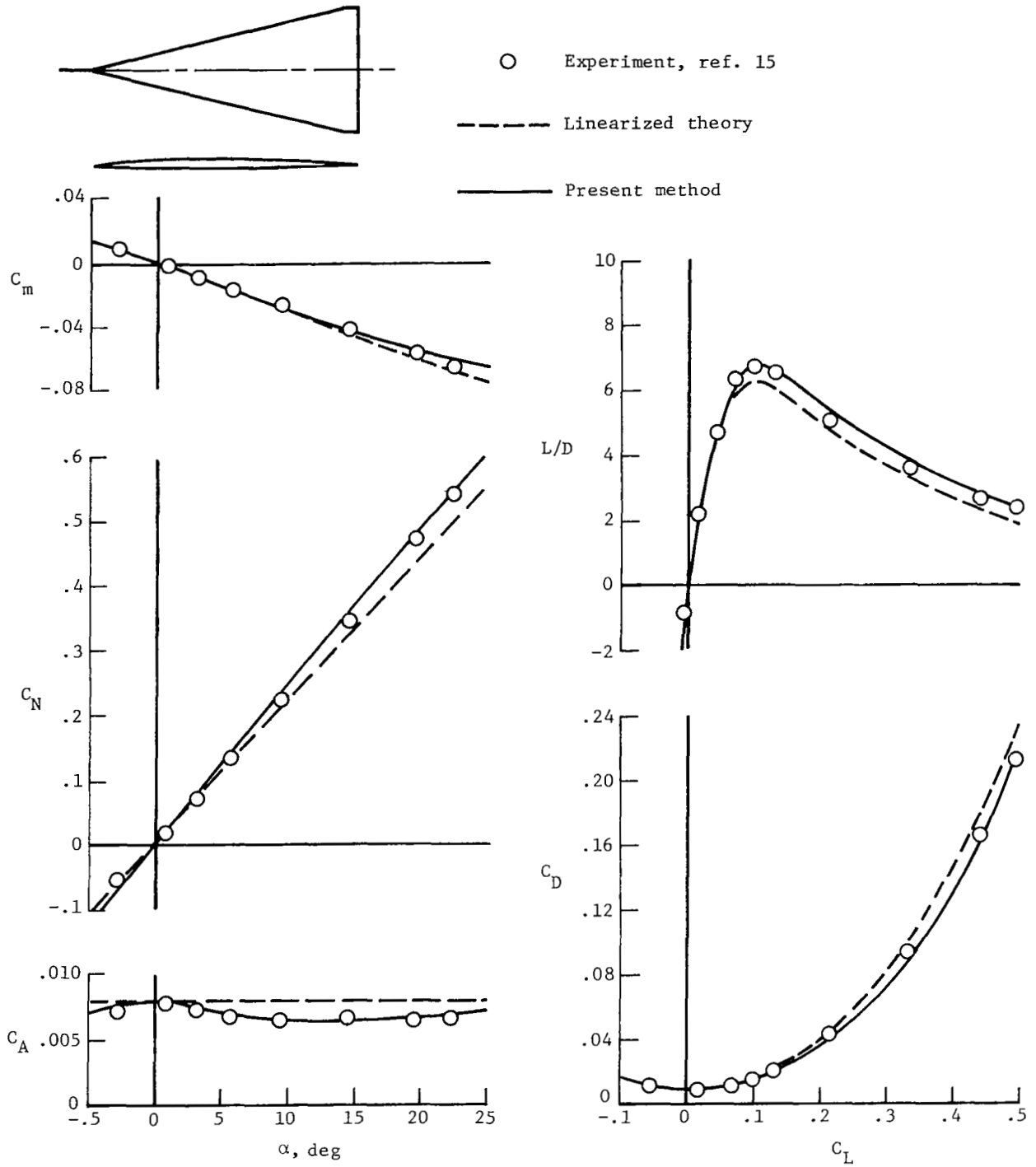

(a) $M_\infty = 2.3$.

Figure 6.- Comparison of predicted and measured forces and moments for uncambered 76° swept leading-edge delta wing.

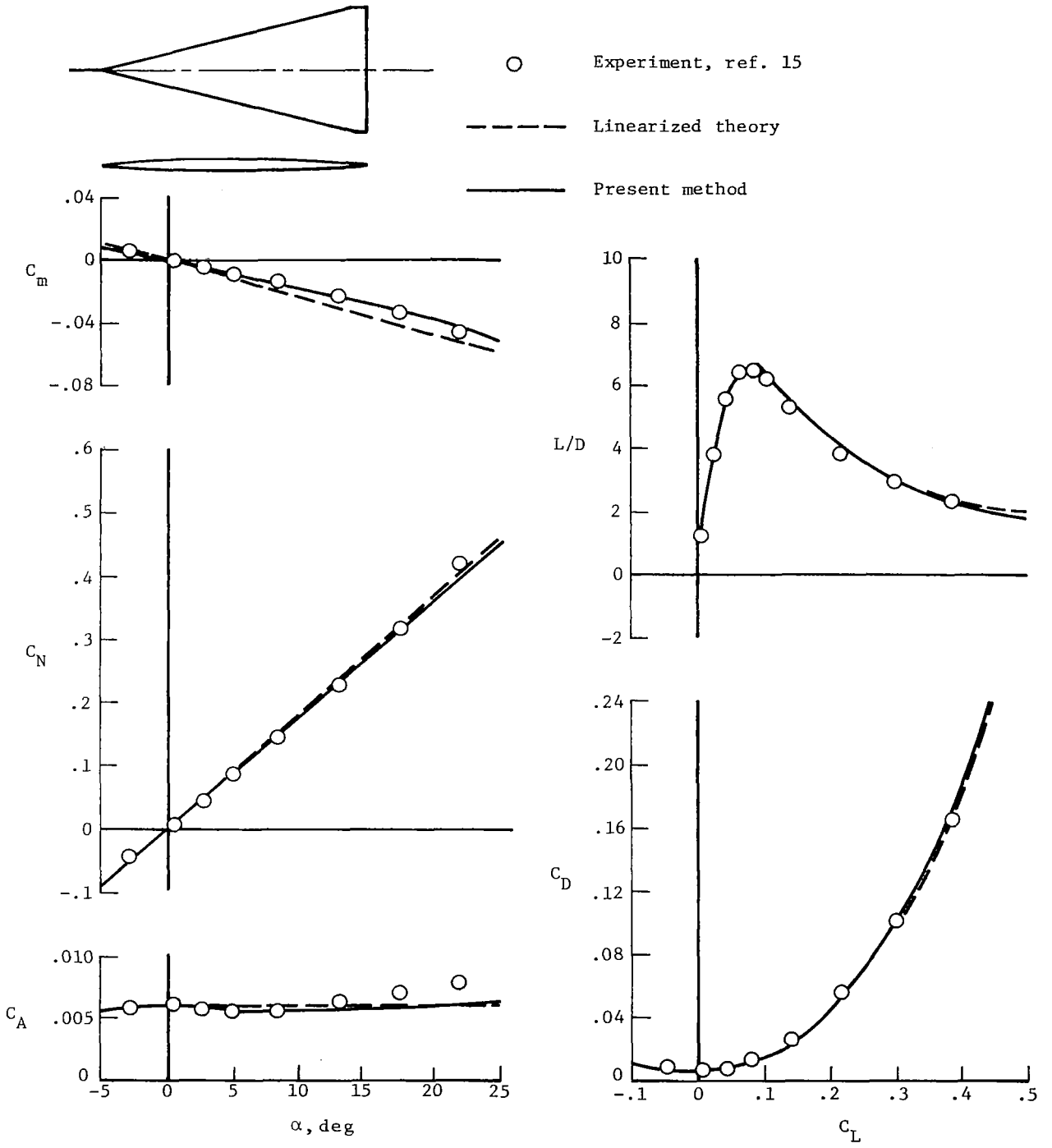

(b) $M_\infty = 3.5$.

Figure 6.- Continued.

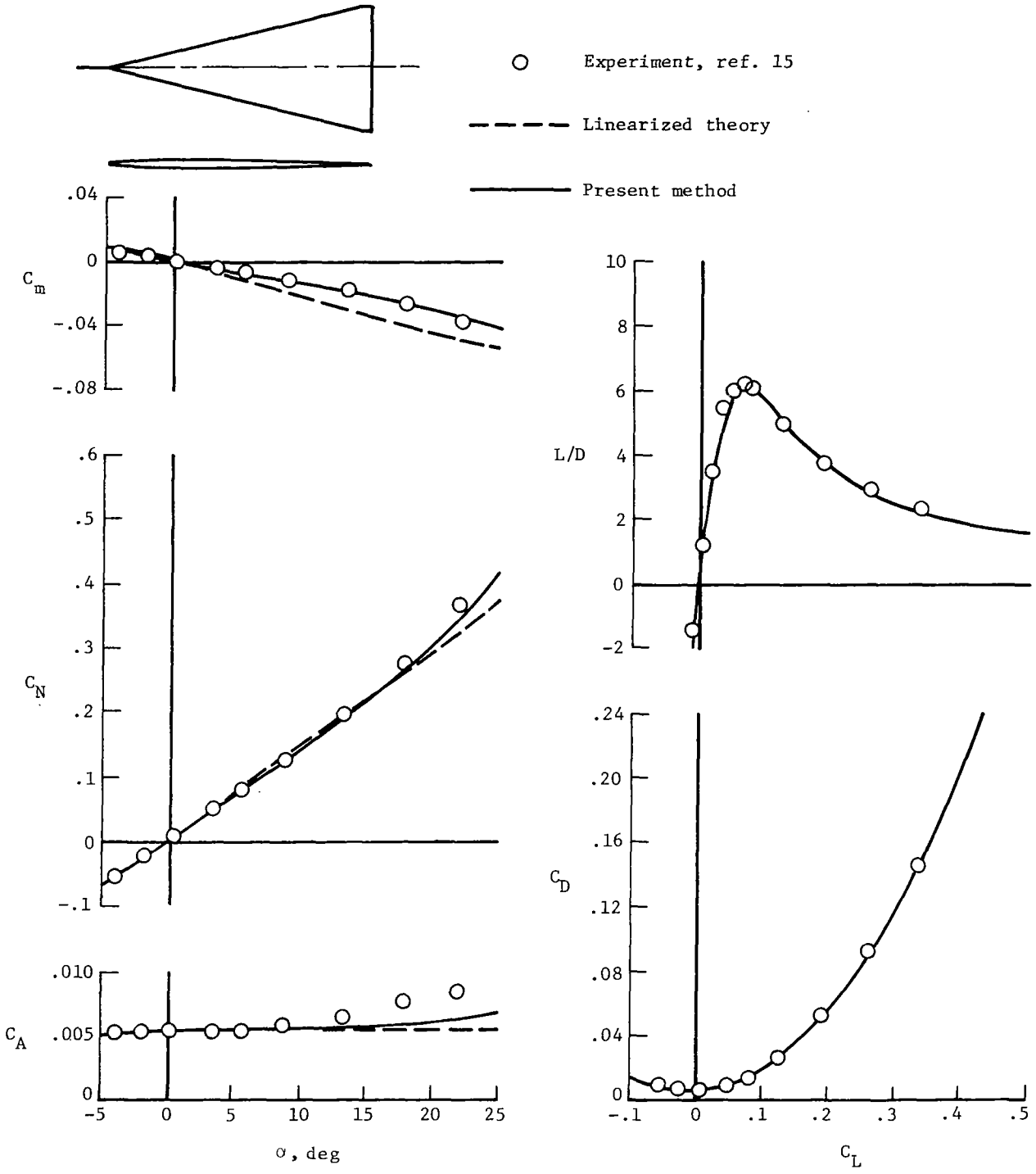

(c) $M_\infty = 4.6$.

Figure 6.- Concluded.

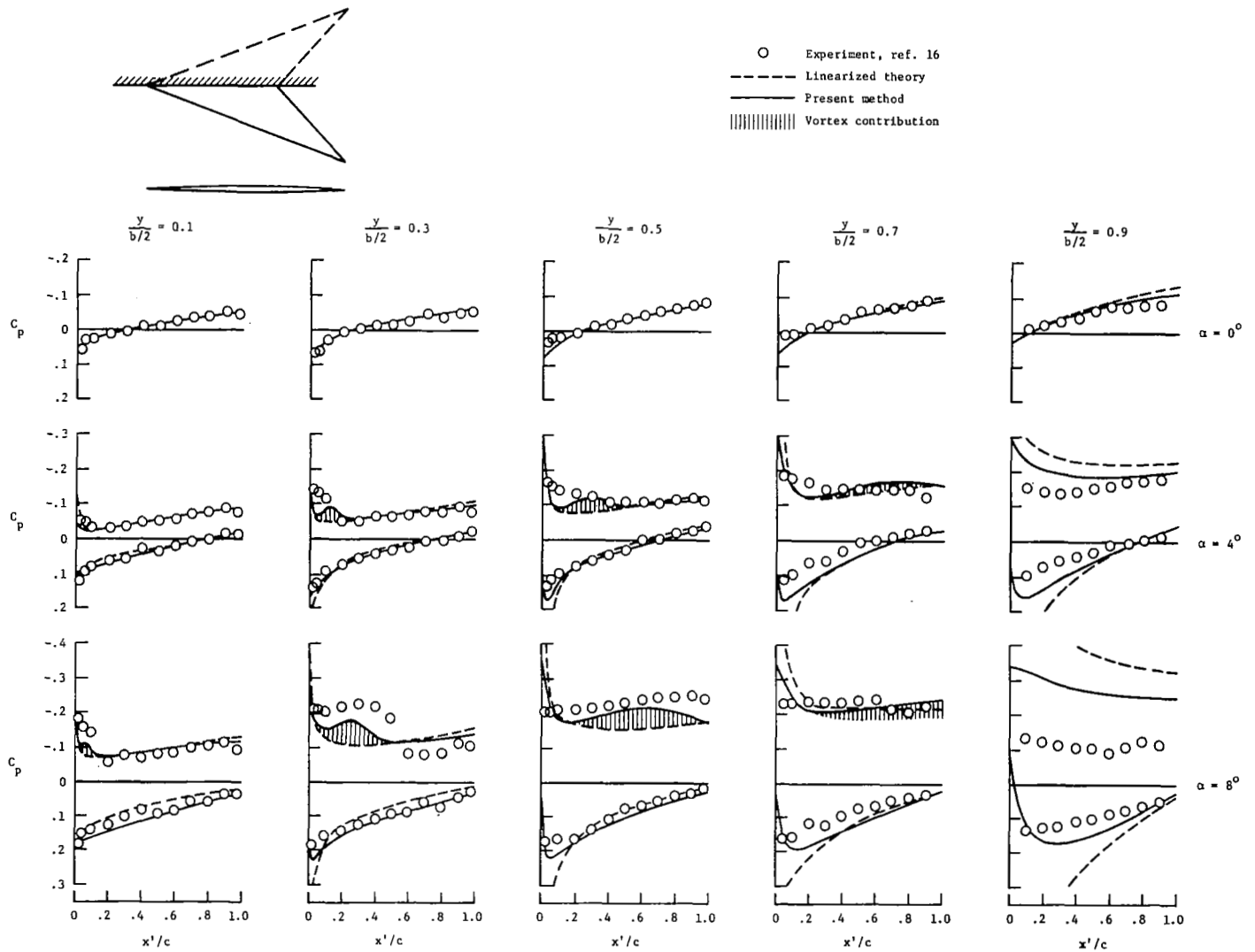

(a) $C_{L,D} = 0.$

Figure 7.- Comparison of predicted and measured pressure distributions for 70° swept leading-edge arrow wing with various degrees of twist and camber. $M_\infty = 2.05$.

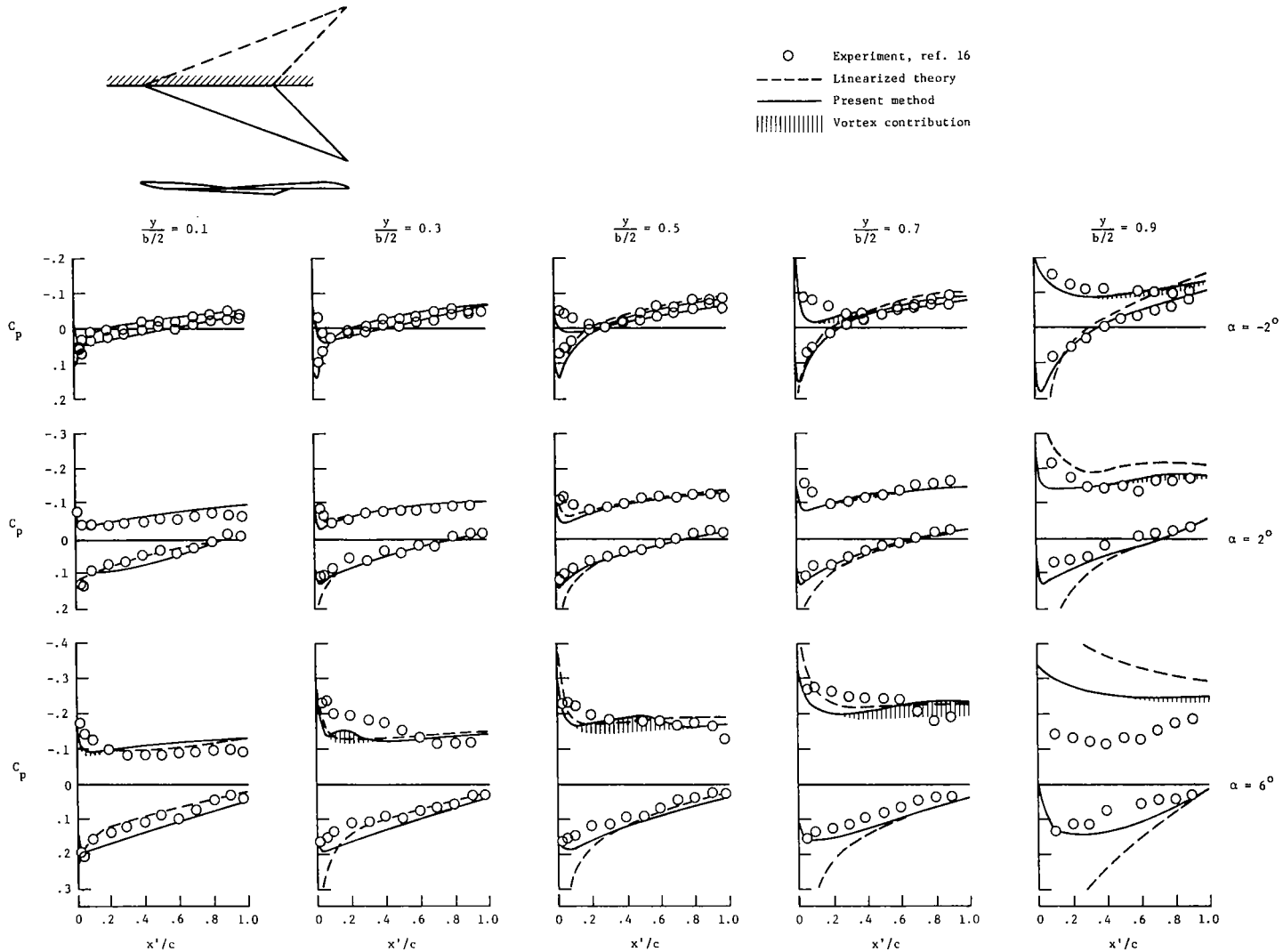

(b) $C_{L,D} = 0.08$.

Figure 7.- Continued.

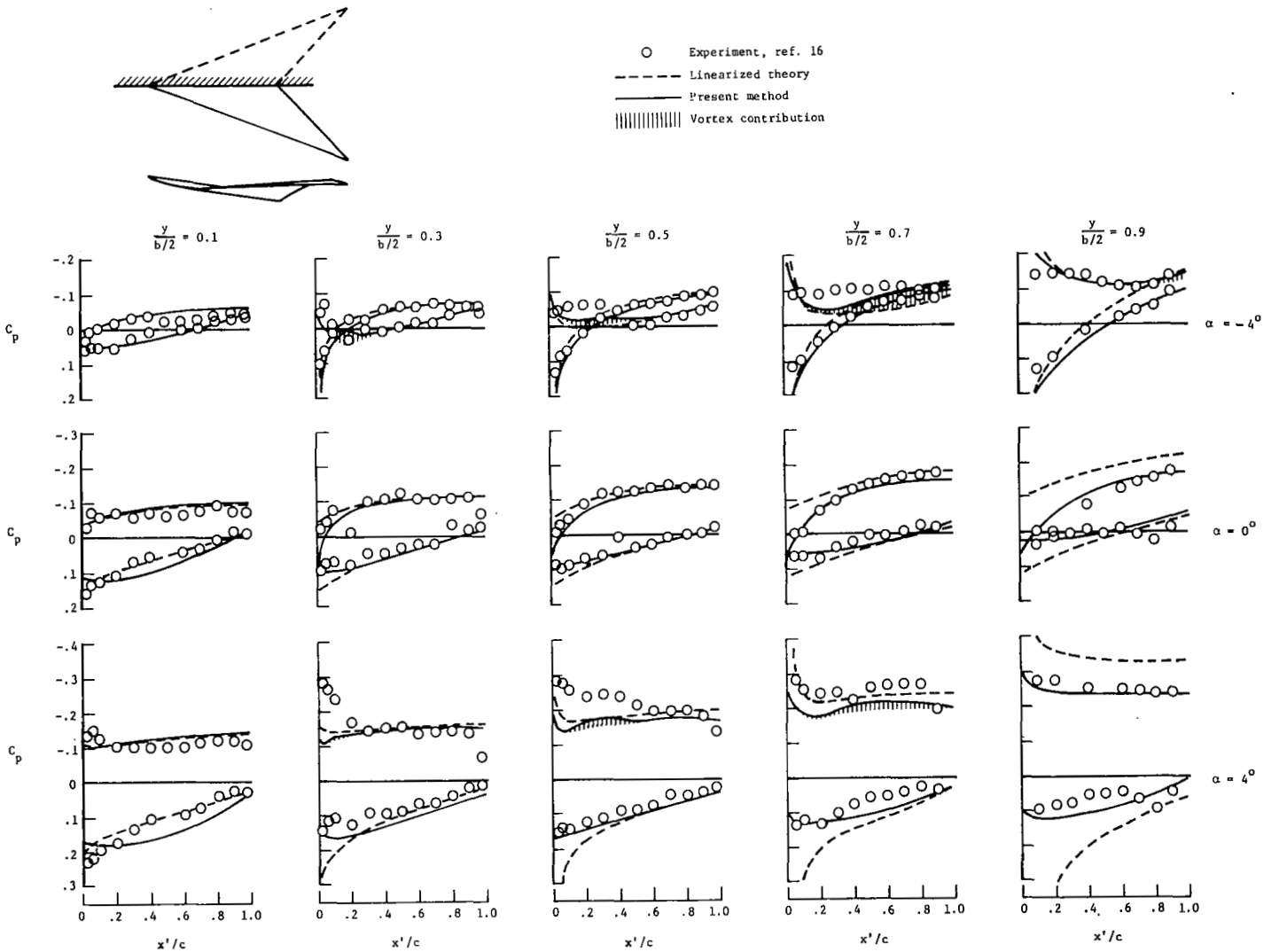

(c) $C_{L,D} = 0.16$.

Figure 7.- Concluded.

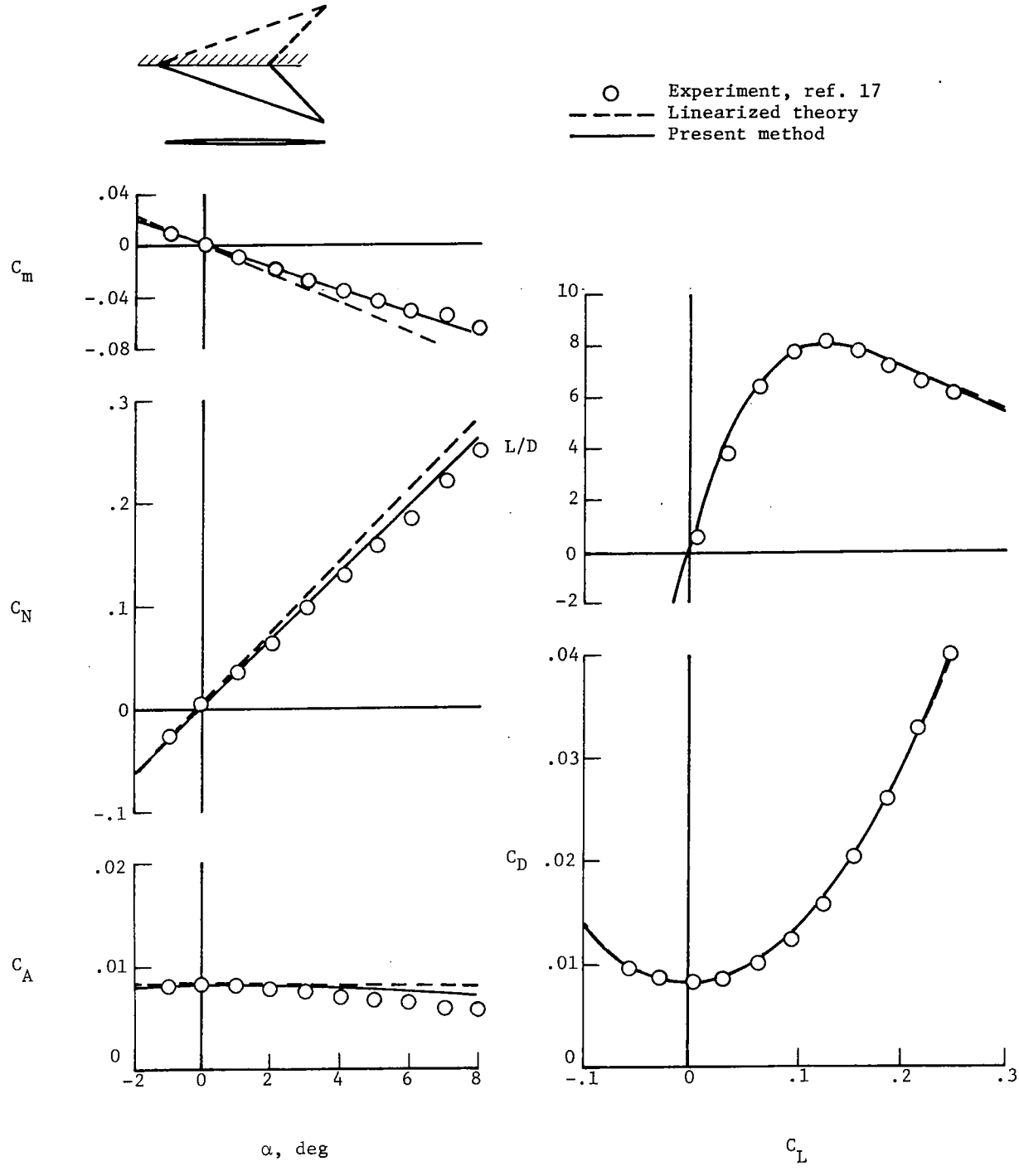

(a) $C_{L,D} = 0.$

Figure 8.- Comparison of predicted and measured forces and moments for 70° swept leading-edge arrow wing with various degrees of twist and camber. $M_\infty = 2.05$.

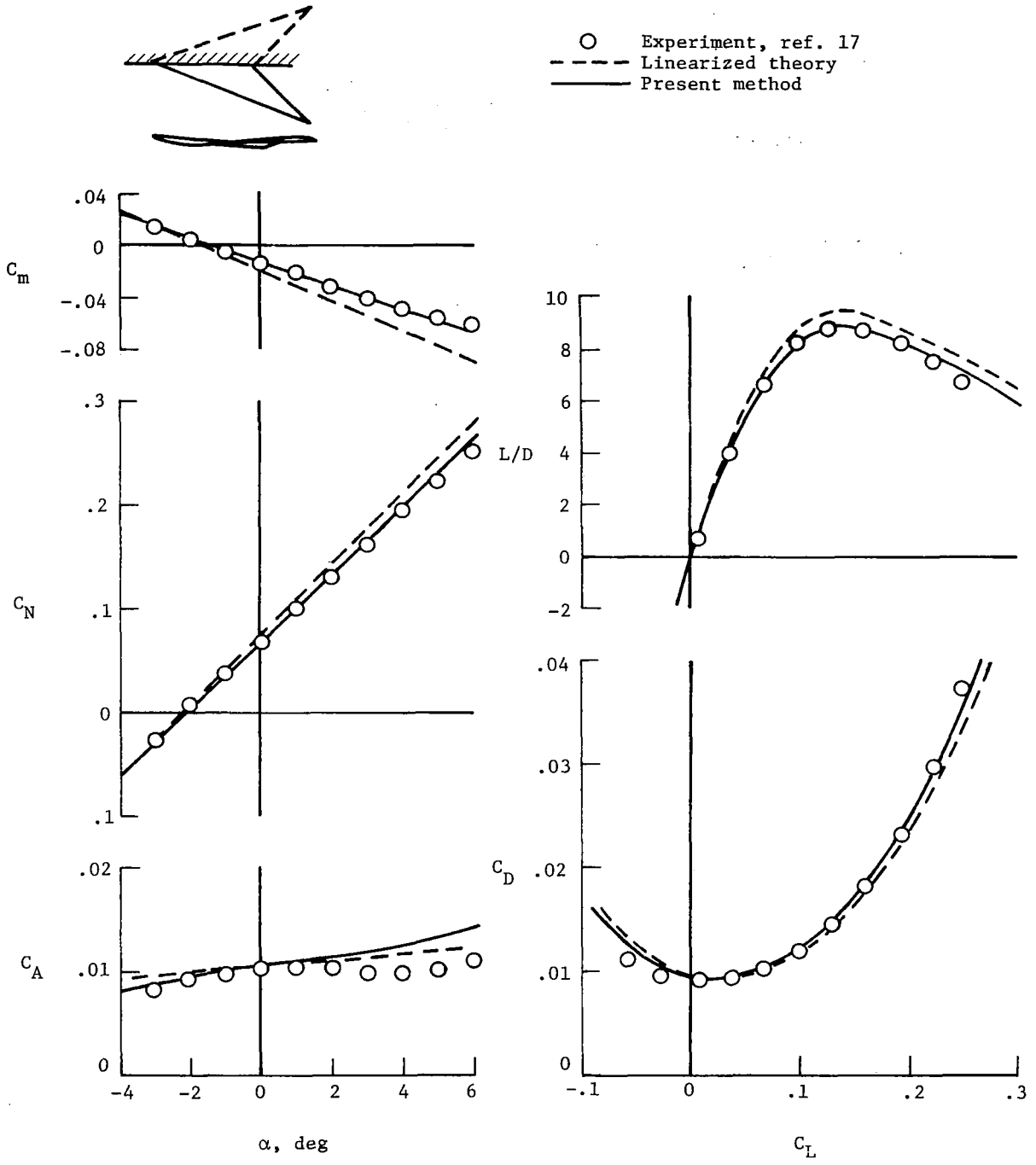

(b) $C_{L,D} = 0.08$.

Figure 8.- Continued.

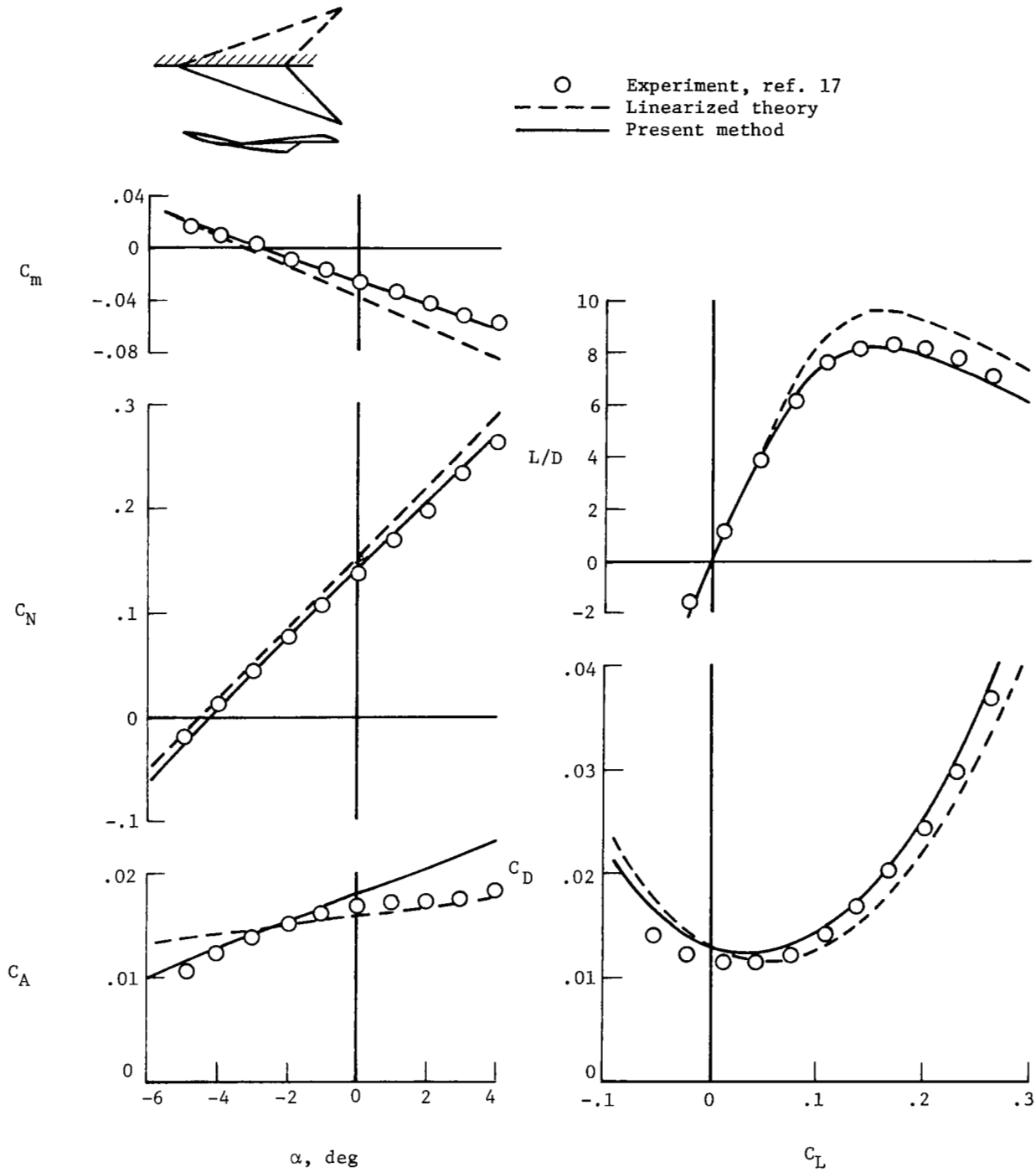

(c) $C_{L,D} = 0.16$.

Figure 8.- Concluded.

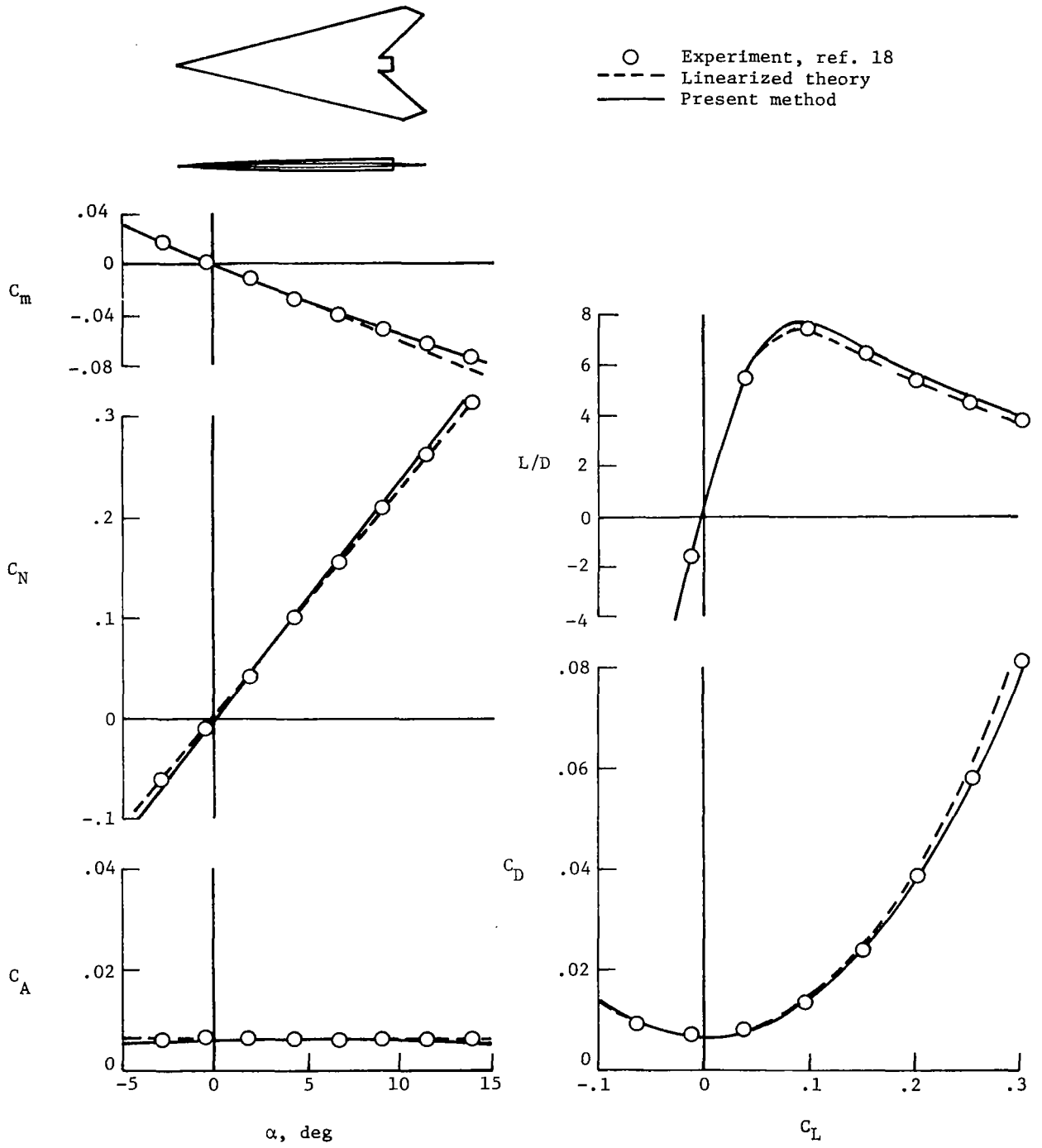

(a) $C_{L,D} = 0$.

Figure 9.- Comparison of predicted and measured forces and moments for 75.96° swept leading-edge arrow wing with various degrees of twist and camber. $M_\infty = 2.6$.

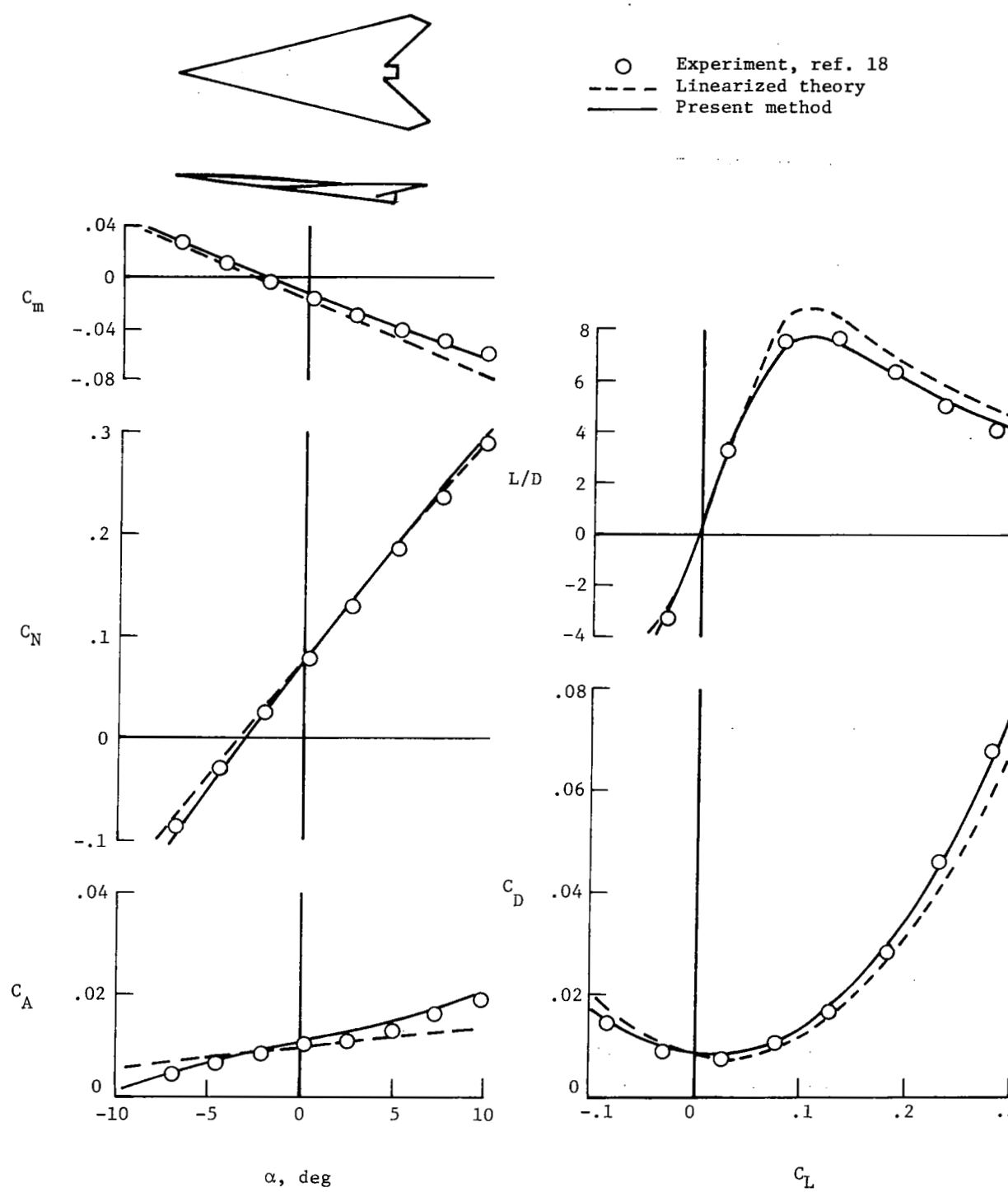

(b) $C_{L,D} = 0.08$.

Figure 9.- Continued.

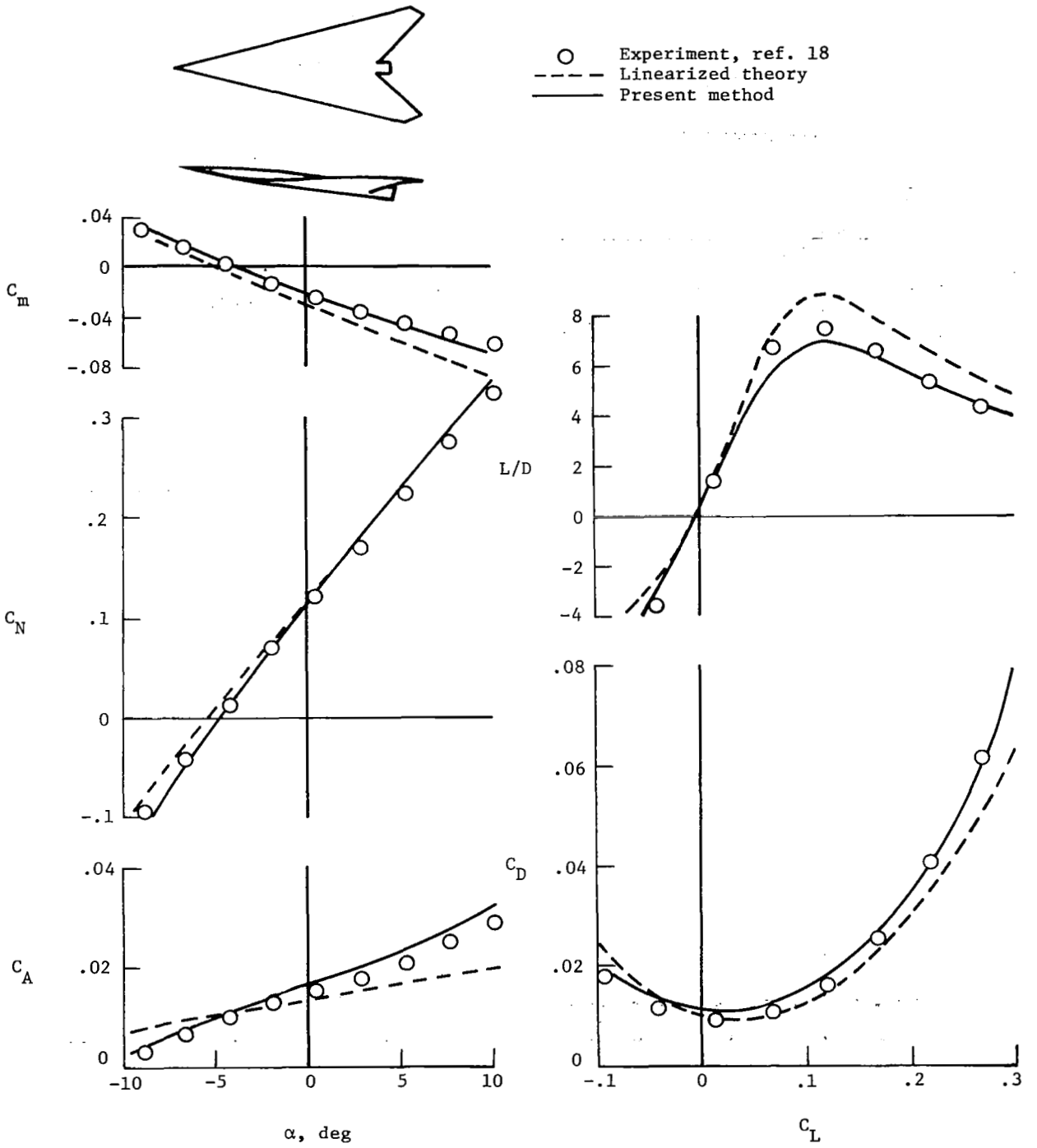

(c) $C_{L,D} = 0.12$.

Figure 9.- Concluded.

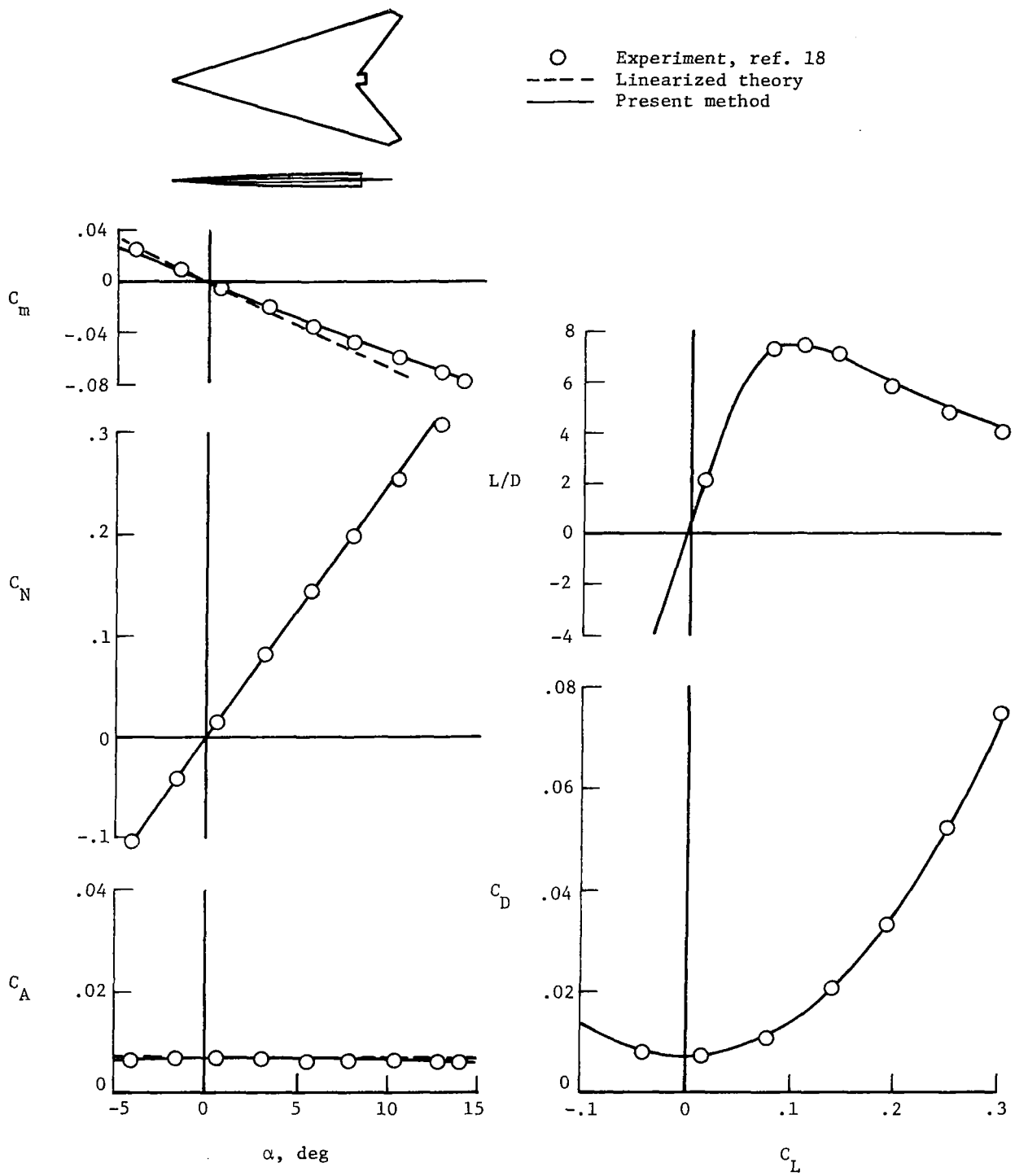

(a) $C_{L,D} = 0$.

Figure 10.- Comparison of predicted and measured forces and moments for 72.65° swept leading-edge arrow wing with various degrees of twist and camber. $M_\infty = 2.6$.

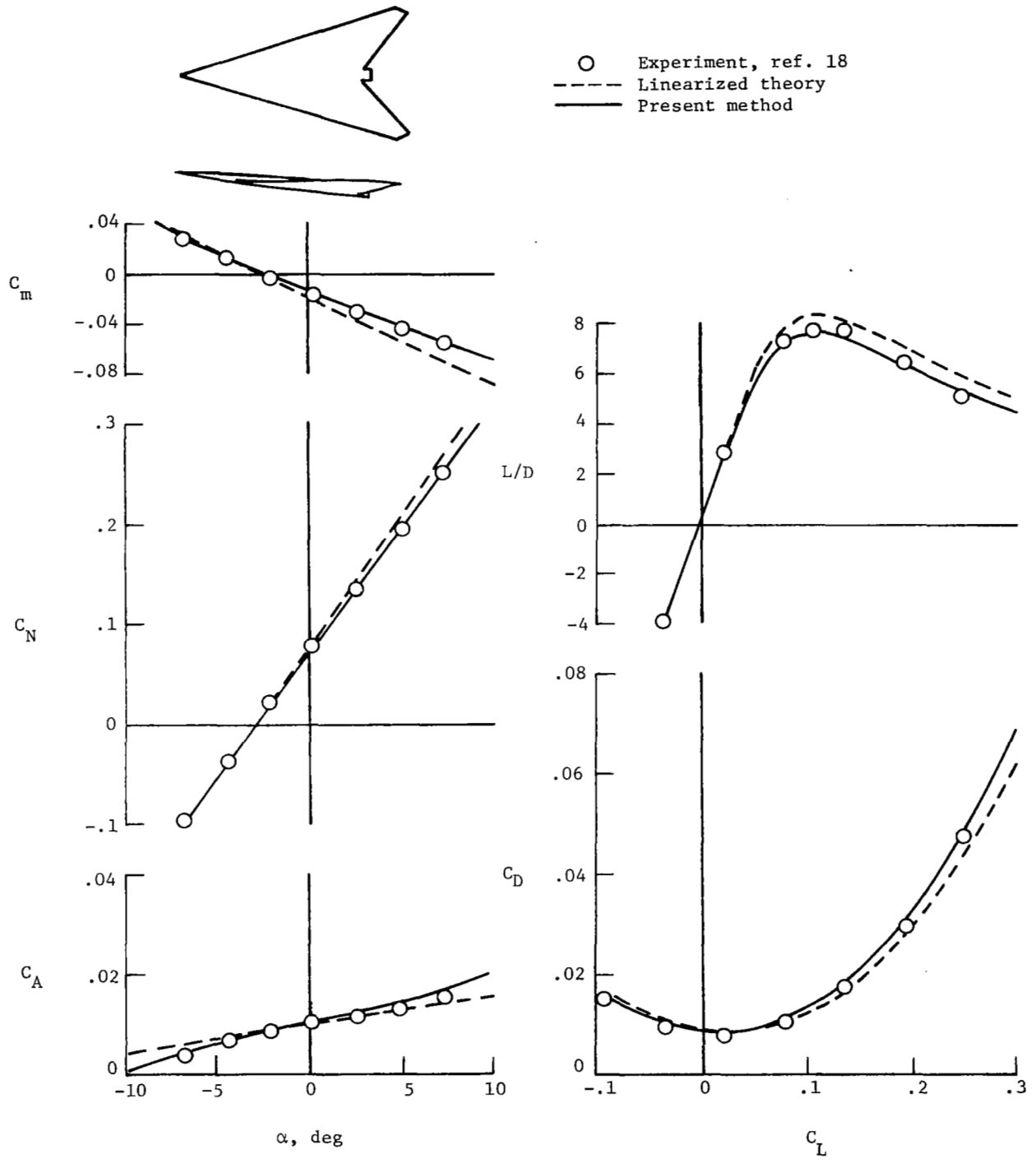

(b) $C_{L,D} = 0.08$.

Figure 10.- Continued.

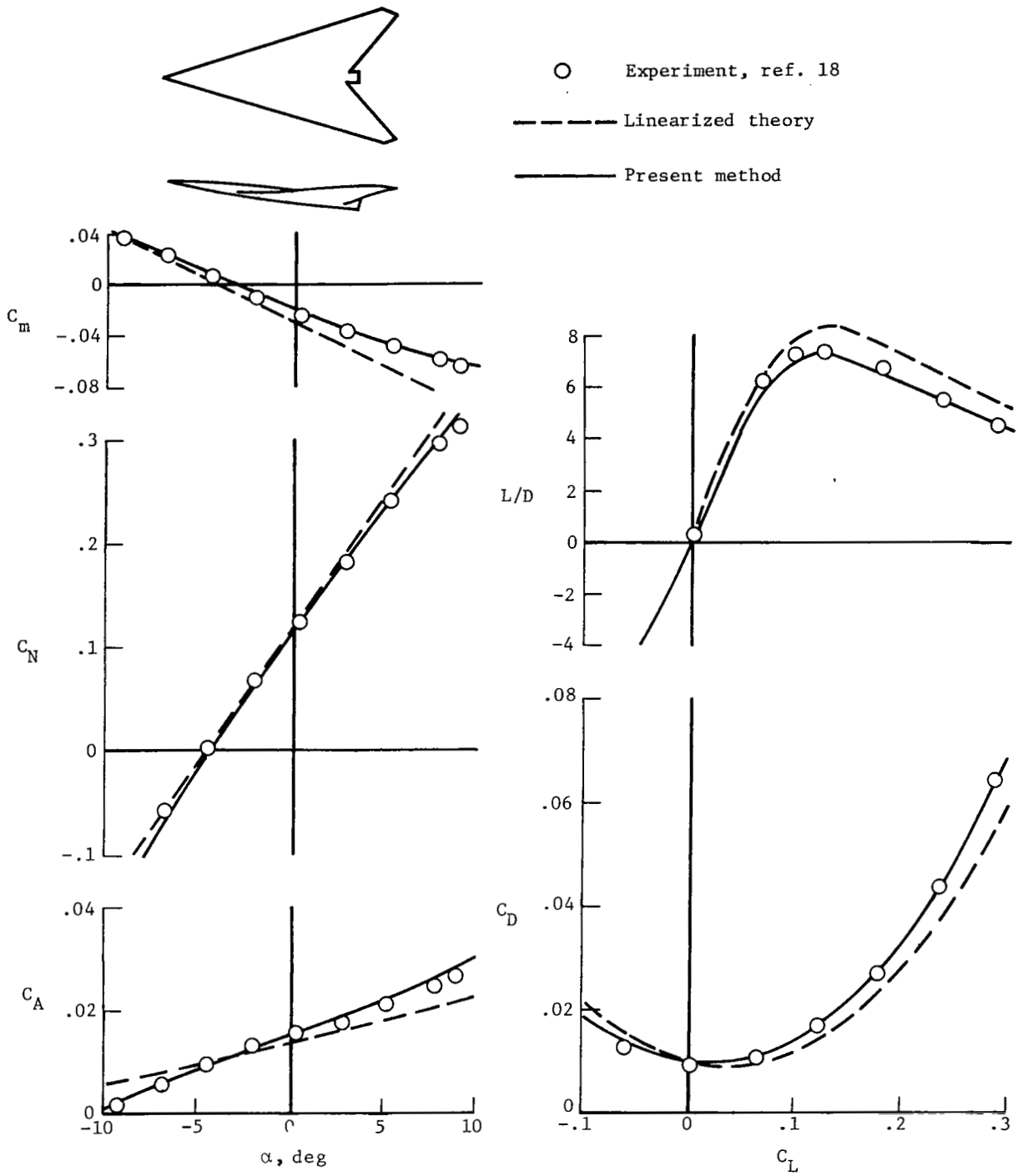

(c) $C_{L,D} = 0.12$.

Figure 10.- Concluded.

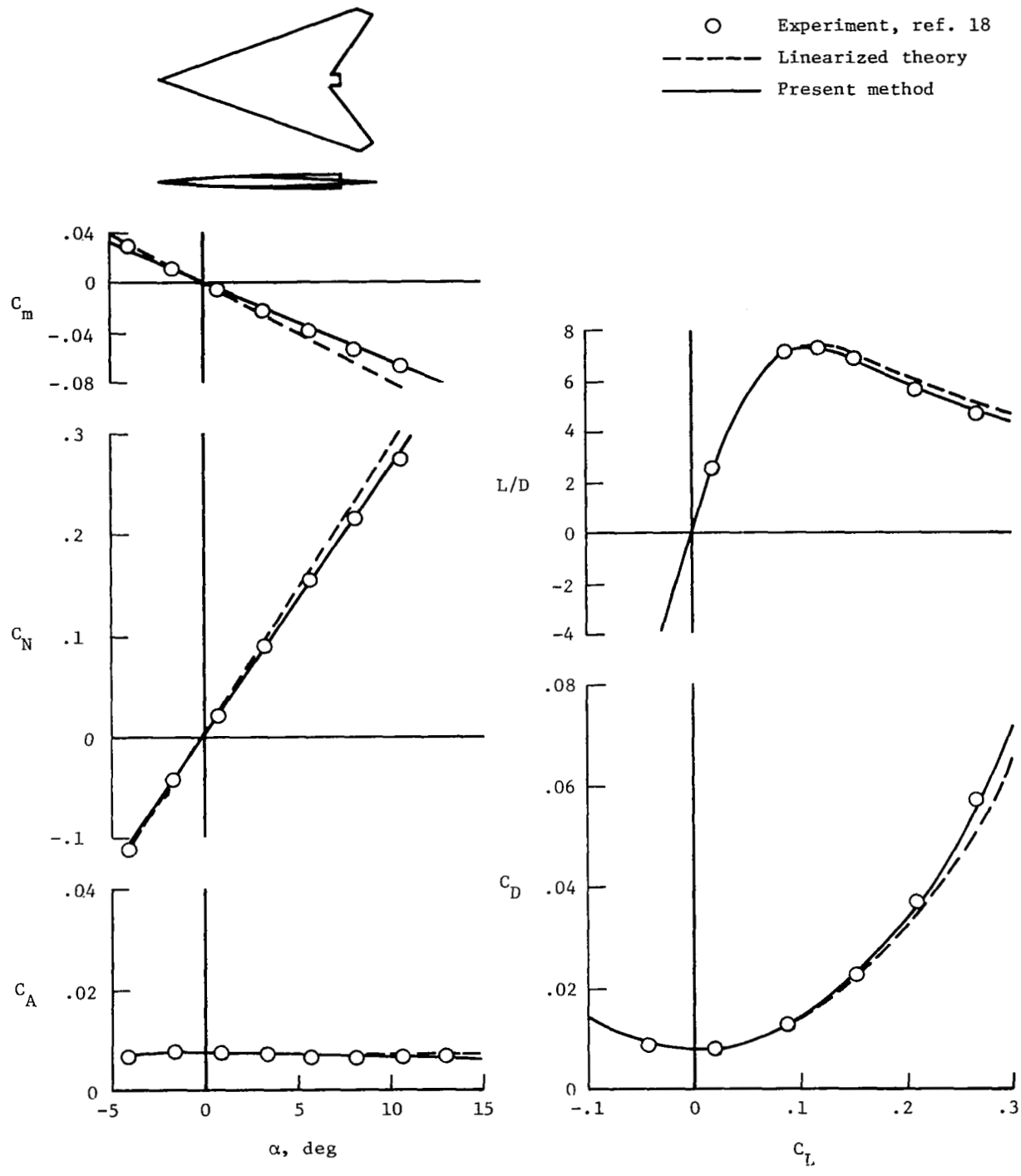

(a) $C_{L,D} = 0.$

Figure 11.- Comparison of predicted and measured forces and moments for 69.44° swept leading-edge arrow wing with various degrees of twist and camber. $M_\infty = 2.6$.

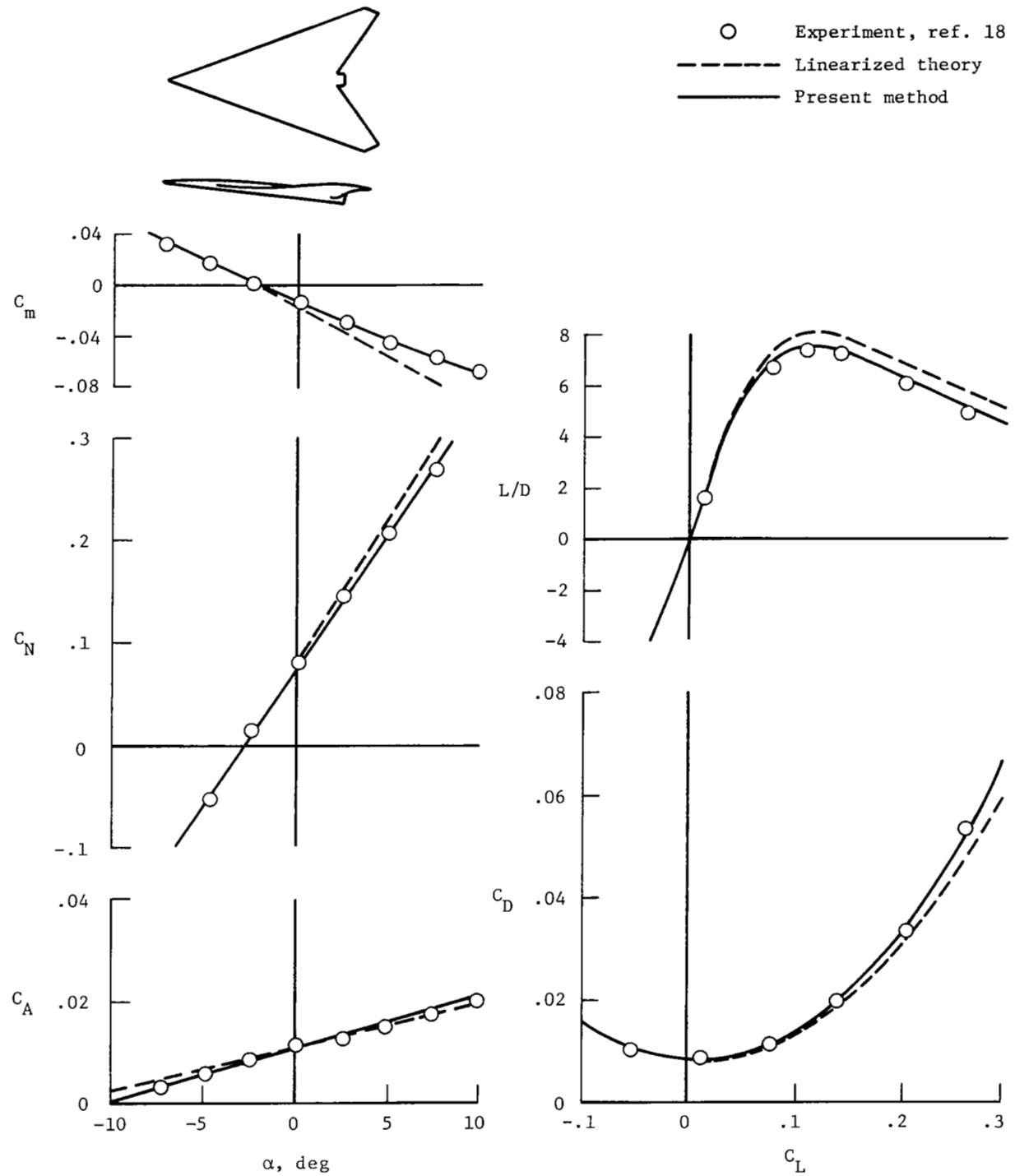

(b) $C_{L,D} = 0.08$.

Figure 11.- Continued.

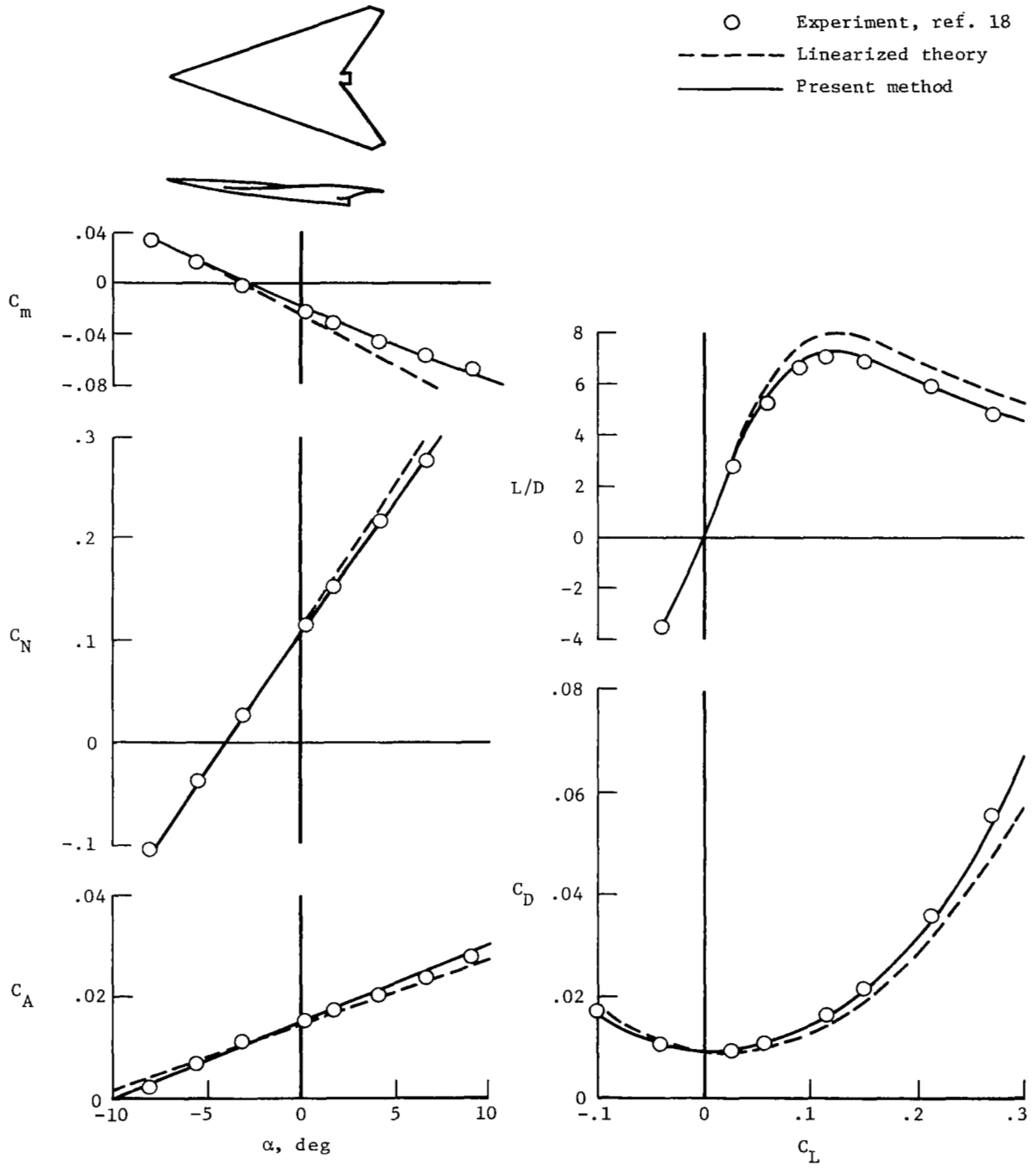

(c) $C_{L,D} = 0.12$.

Figure 11.- Concluded.

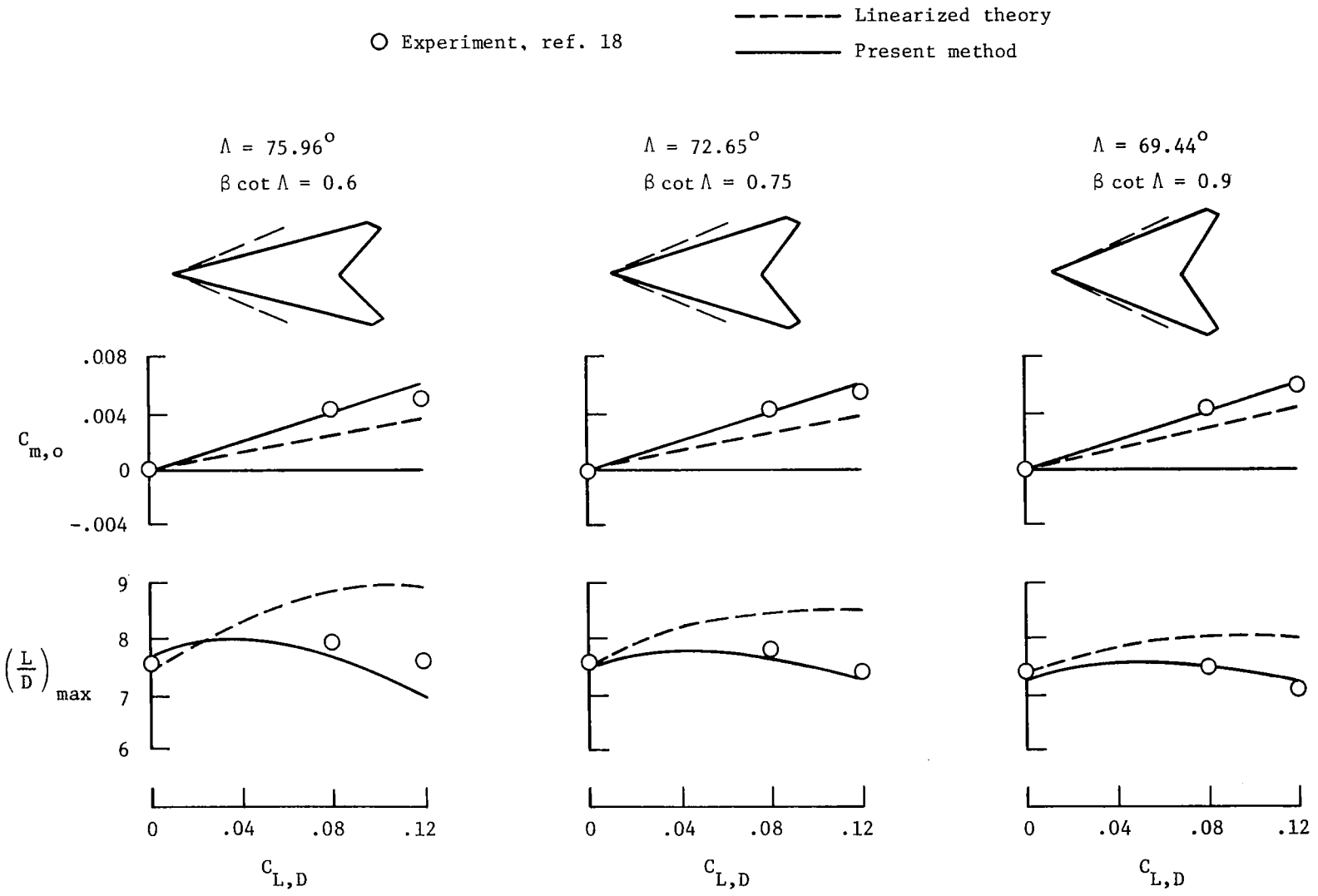

Figure 12.- Comparison of predicted and measured variation of key aerodynamic parameters with camber surface severity for set of arrow wings. $M_\infty = 2.6$.

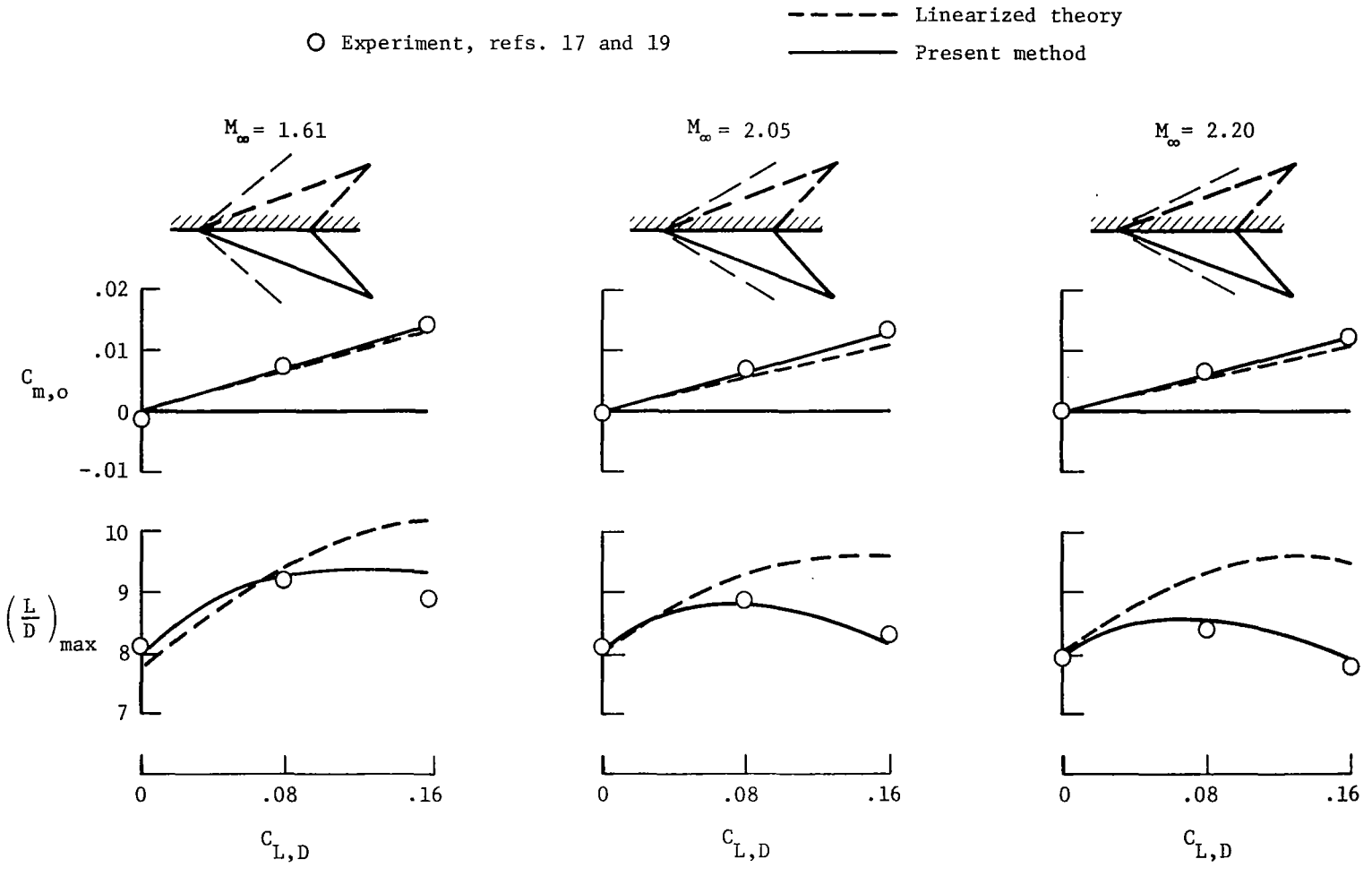

Figure 13.- Comparison of predicted and measured variation of key aerodynamic parameters with camber surface severity for 70° swept leading-edge arrow wing.

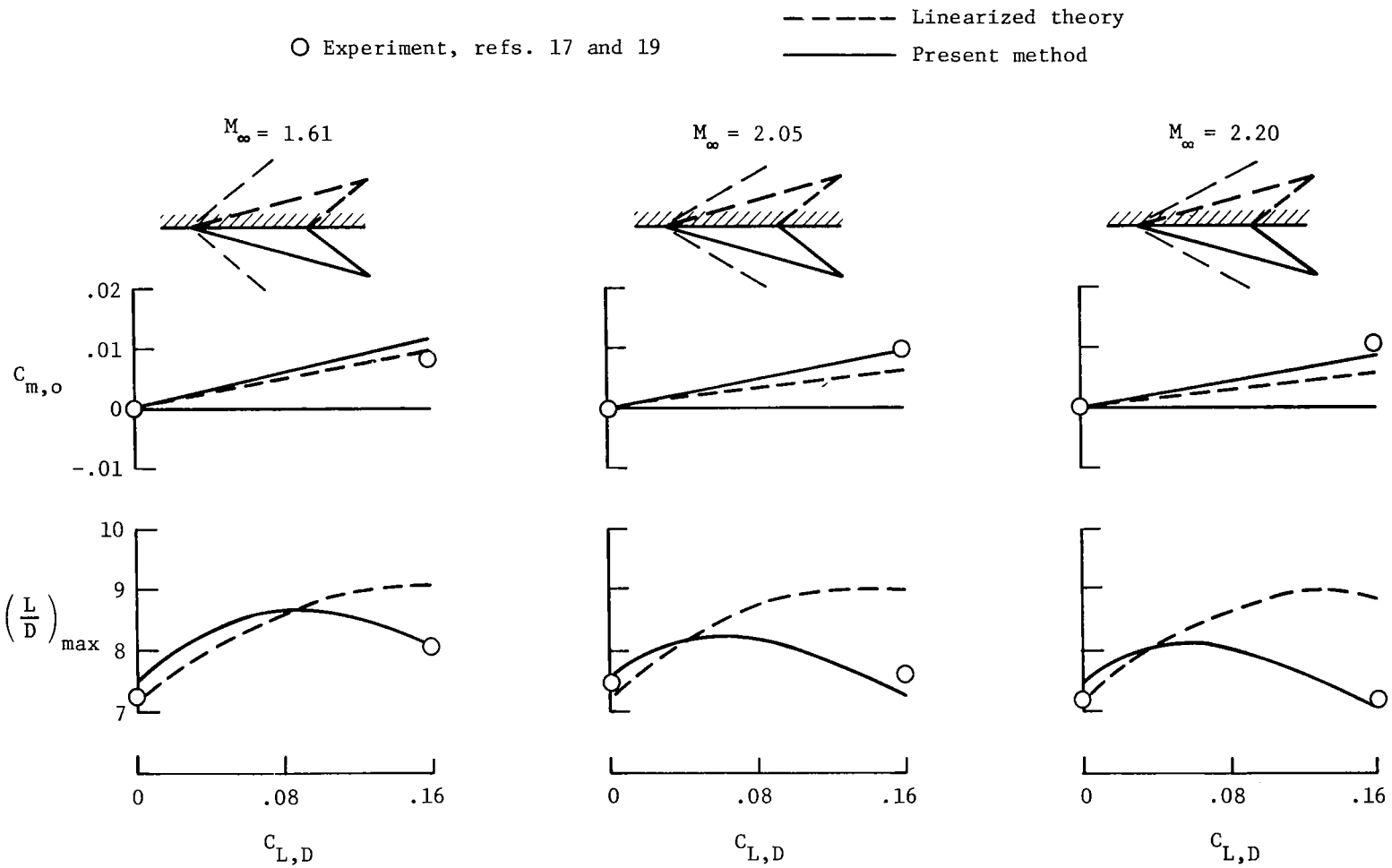

Figure 14.- Comparison of predicted and measured variation of key aerodynamic parameters with camber surface severity for 75° swept leading-edge arrow wing.

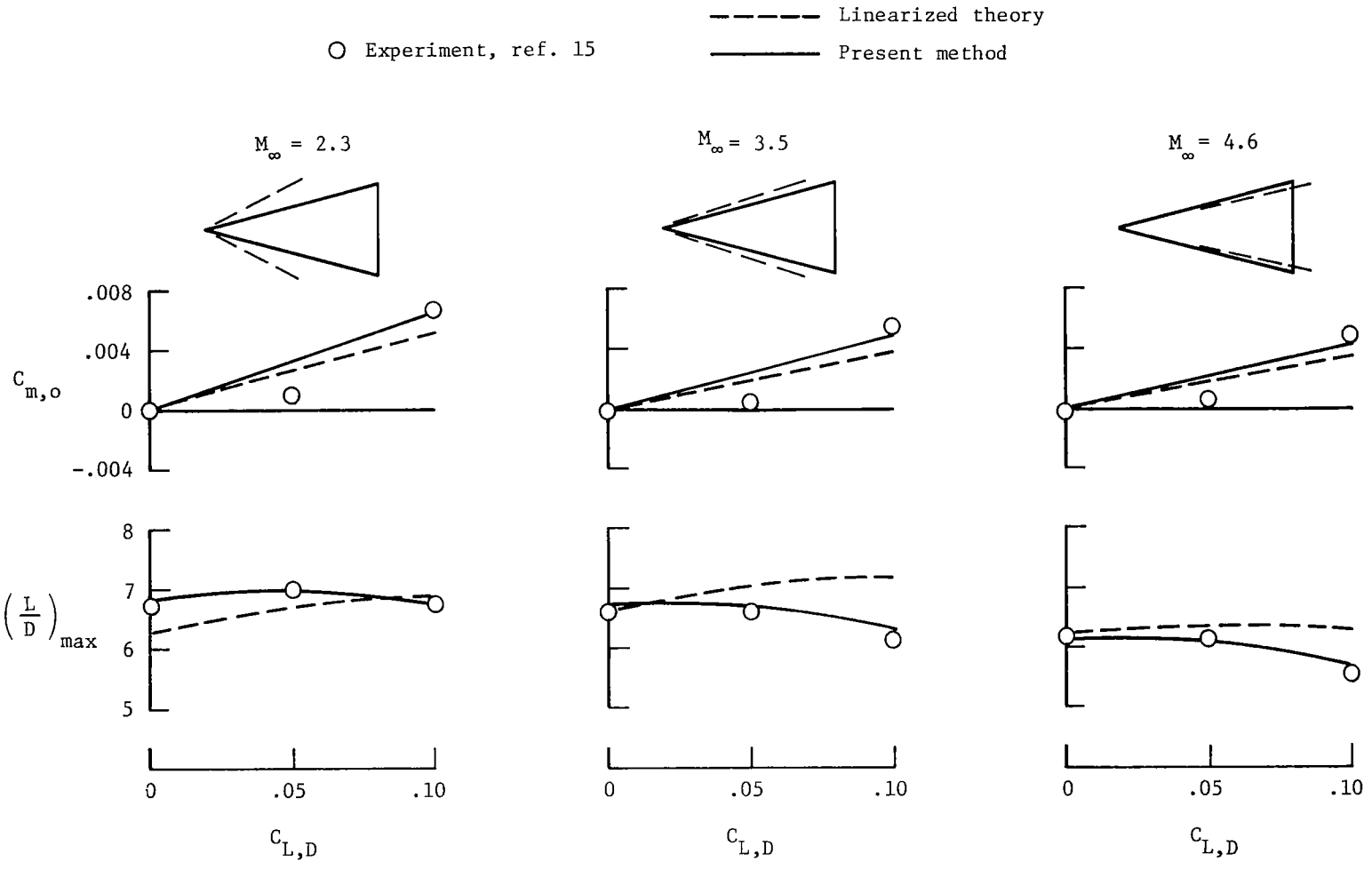

Figure 15.- Comparison of predicted and measured variation of key aerodynamic parameters with camber surface severity for 76° swept leading-edge arrow wing.

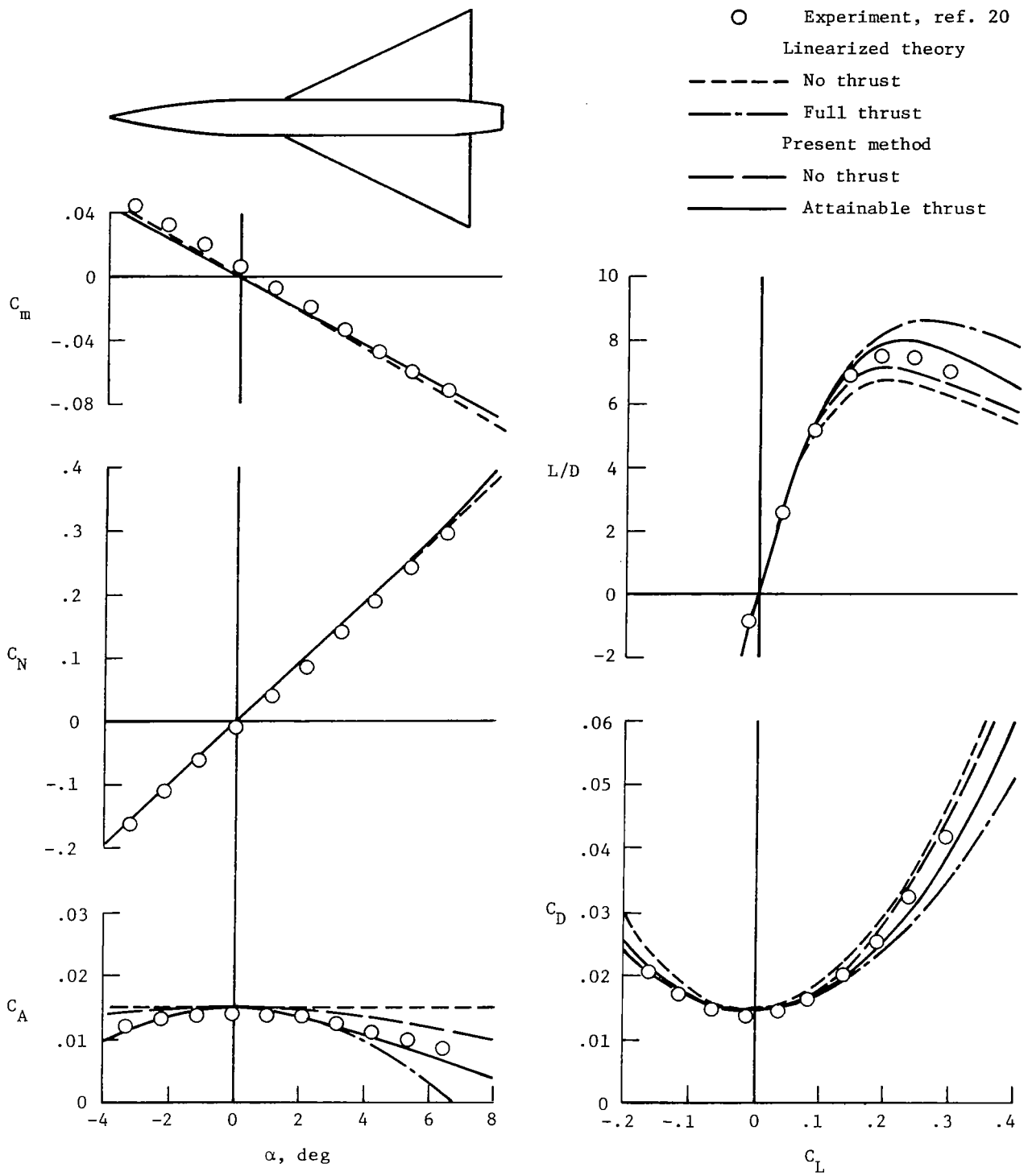

(a) $M_\infty = 1.3$.

Figure 16.- Comparison of predicted and measured forces and moments for aspect-ratio-2 delta wing with rounded leading edge.

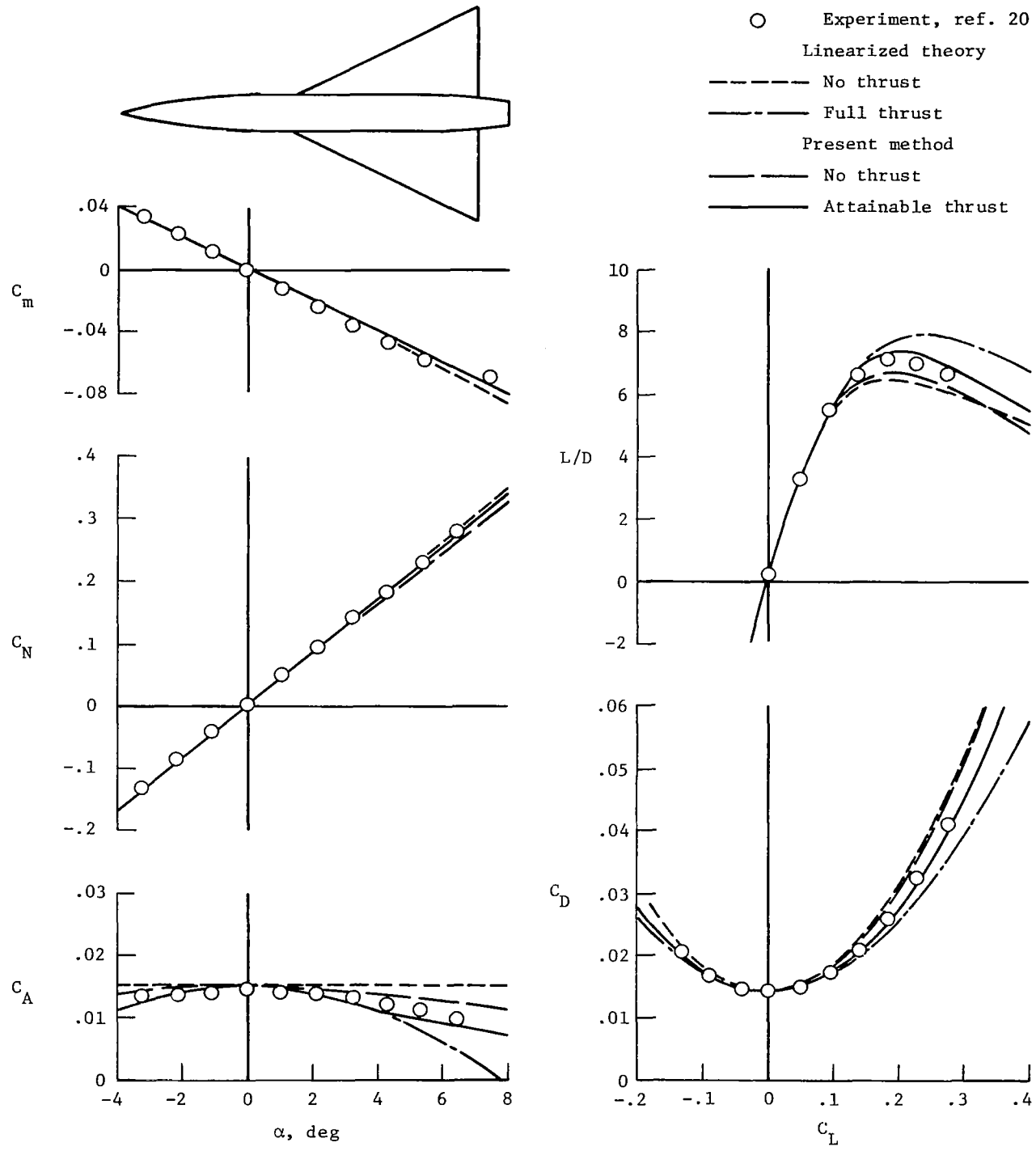

(b) $M_\infty = 1.53$.

Figure 16.- Continued.

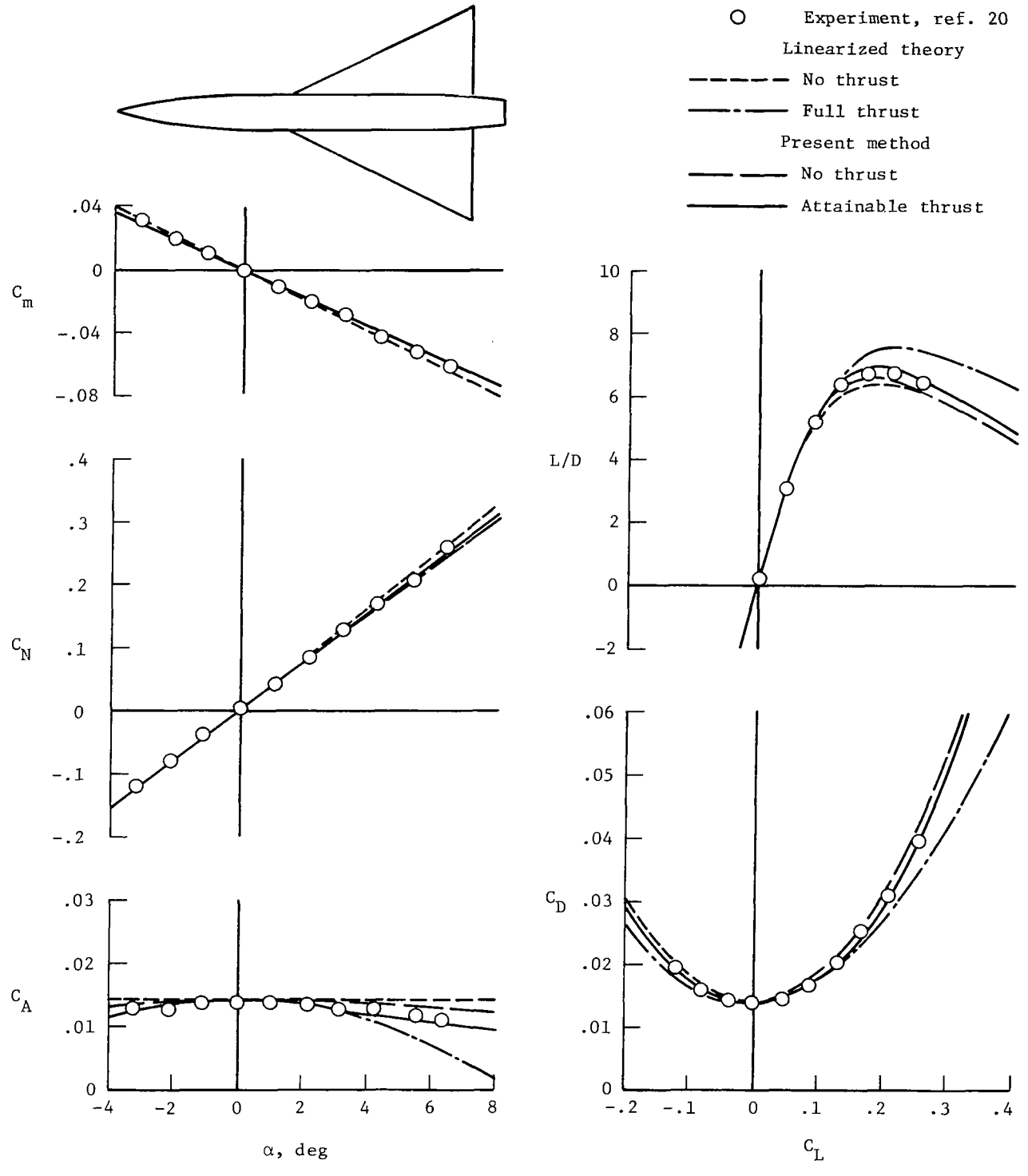

(c) $M_\infty = 1.7$.

Figure 16.- Concluded.

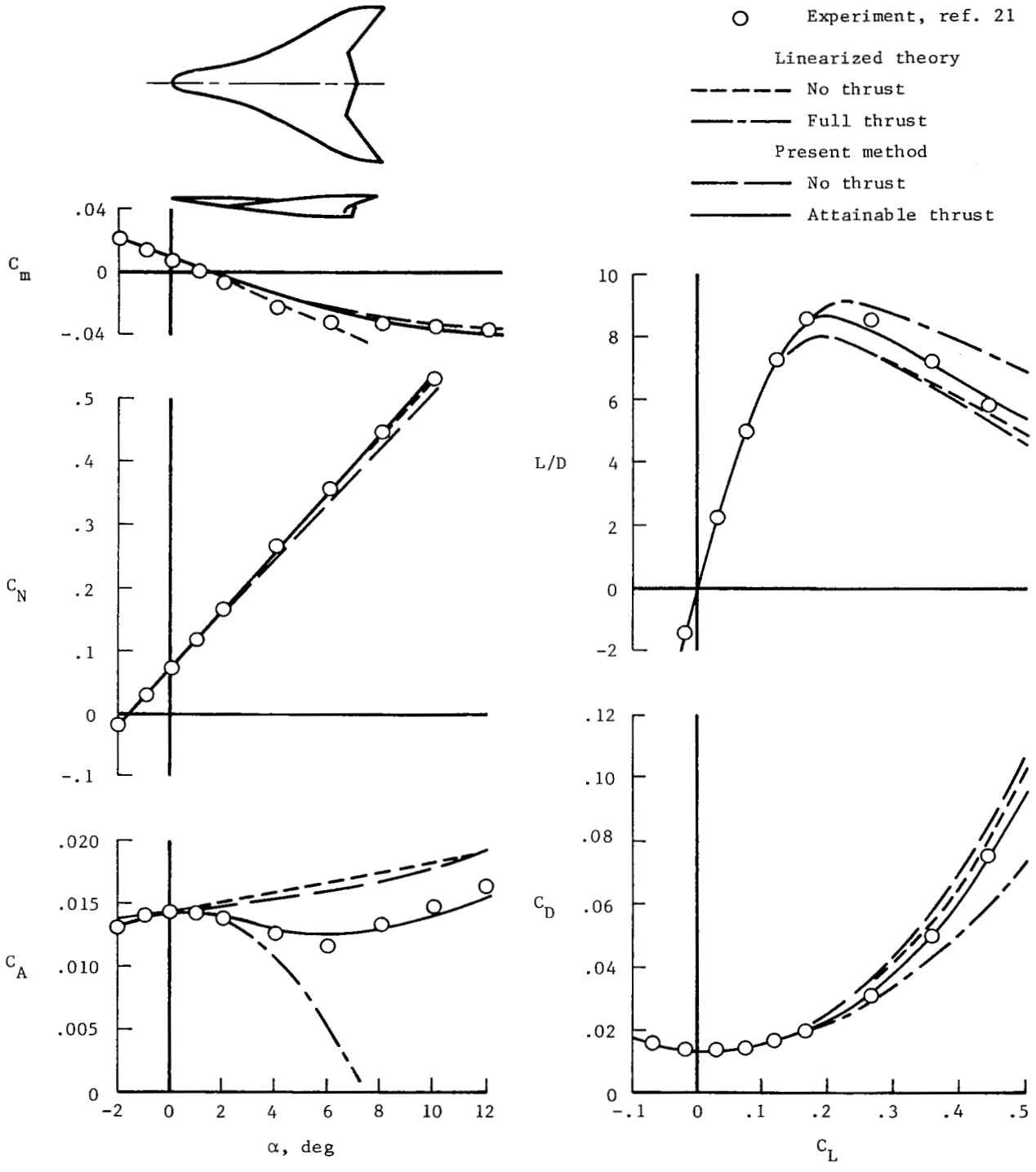

(a) $M_\infty = 1.5$.

Figure 17.- Comparison of predicted and measured forces and moments for twisted and cambered wing of arbitrary planform.

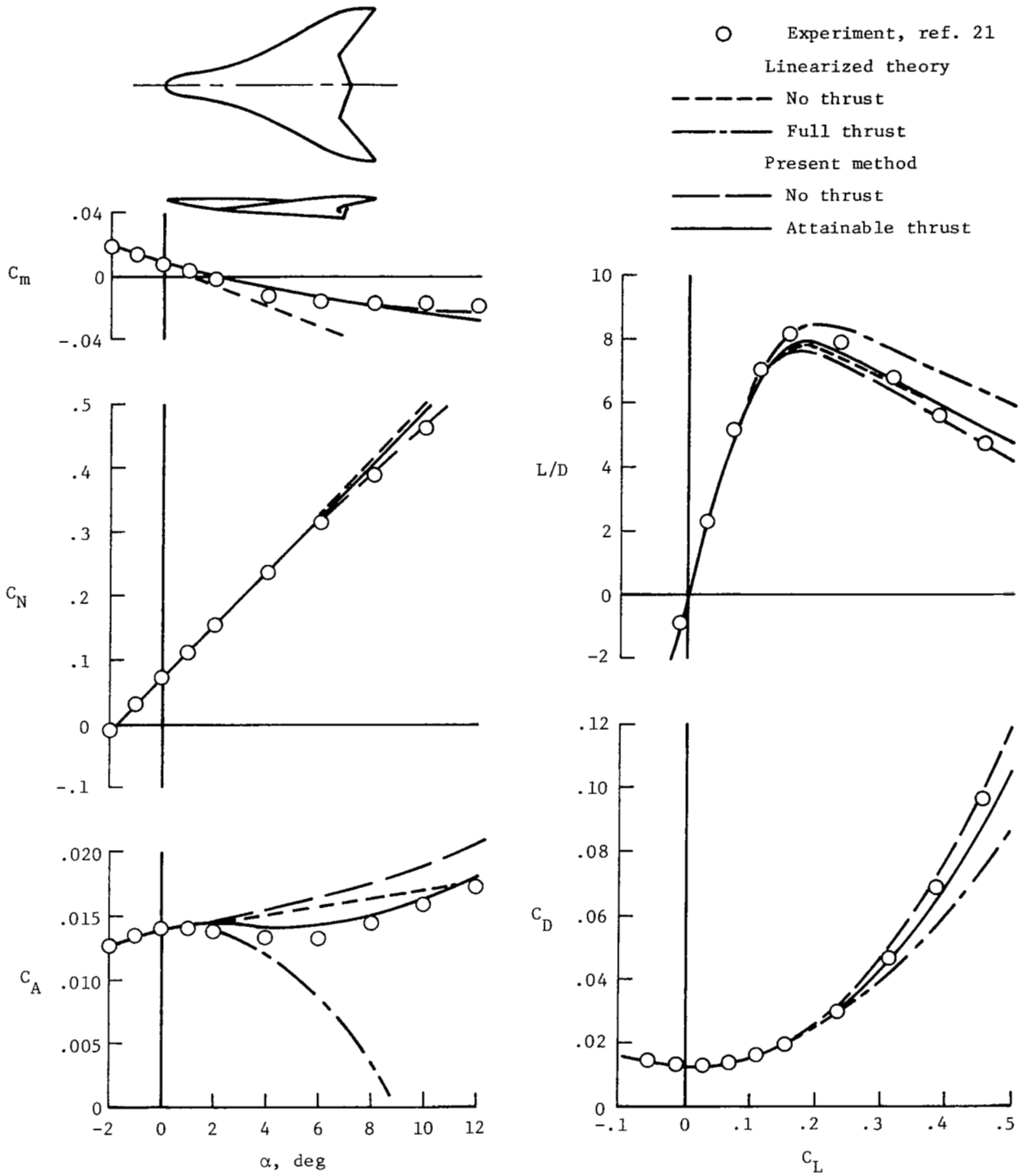

(b) $M_\infty = 1.8$.

Figure 17.- Continued.

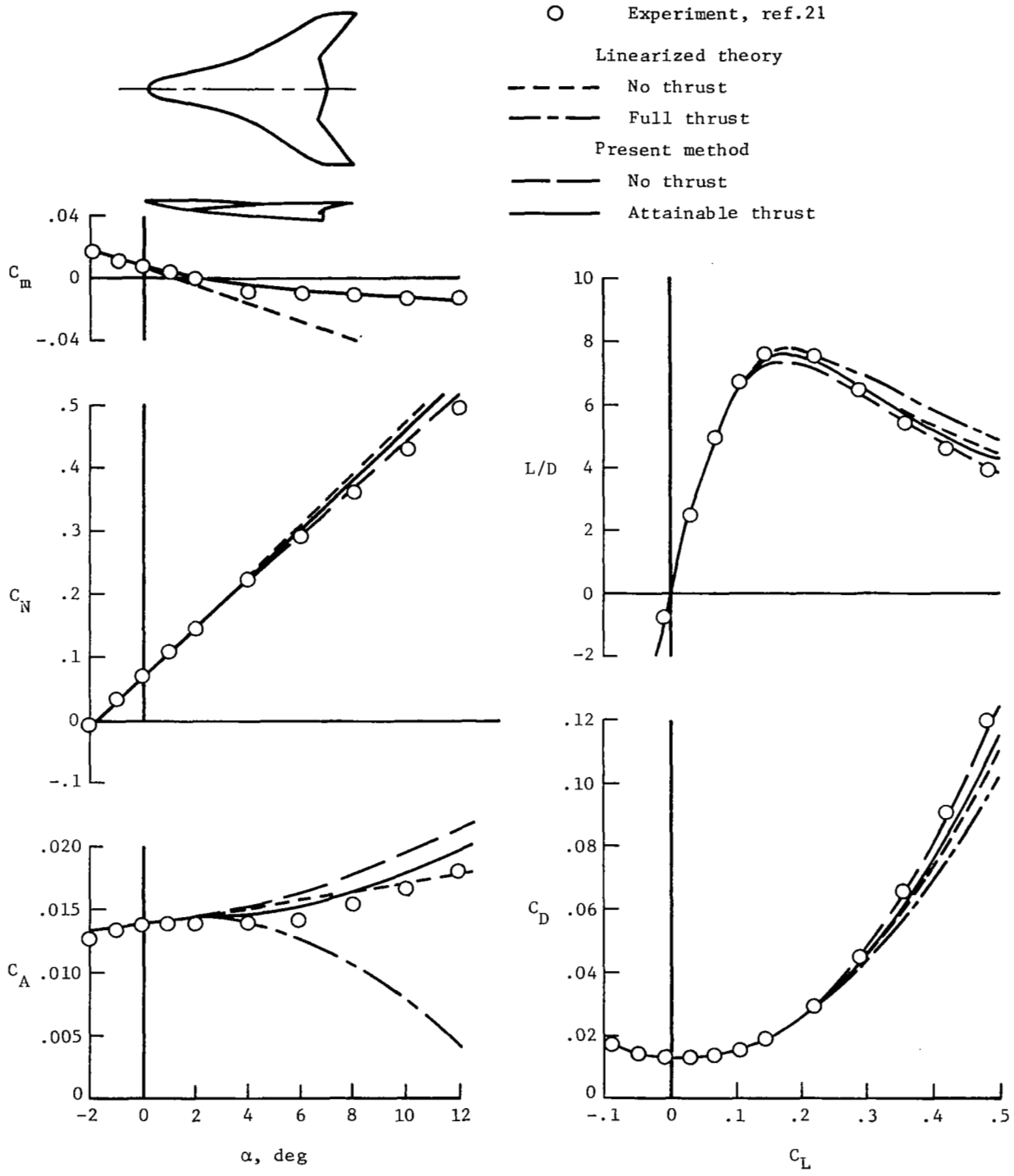

(c) $M_\infty = 2.0$.

Figure 17.- Concluded.

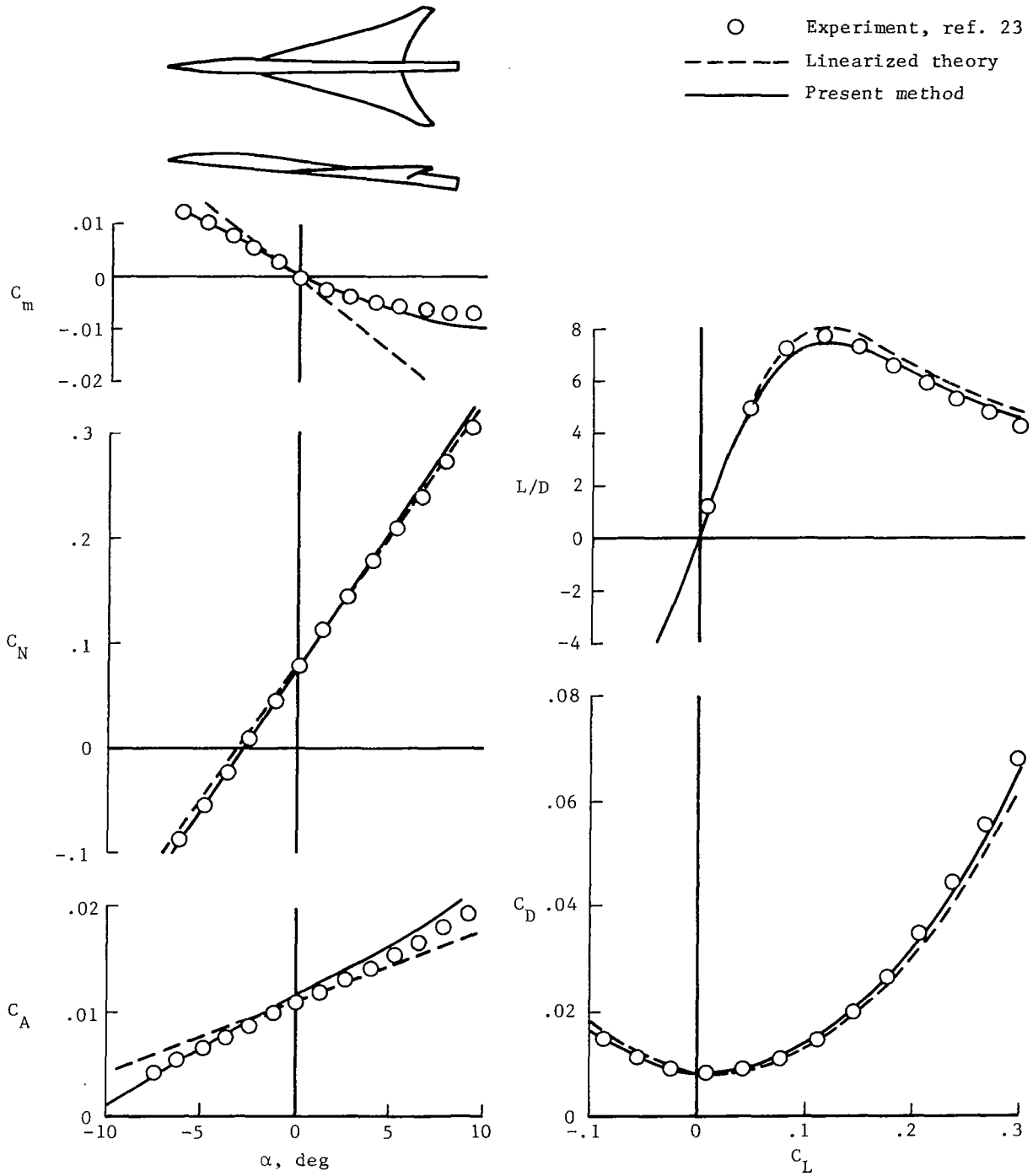

Figure 18.- Comparison of predicted and measured forces and moments for supersonic cruise configuration of high aerodynamic efficiency. $M_\infty = 2.7$.

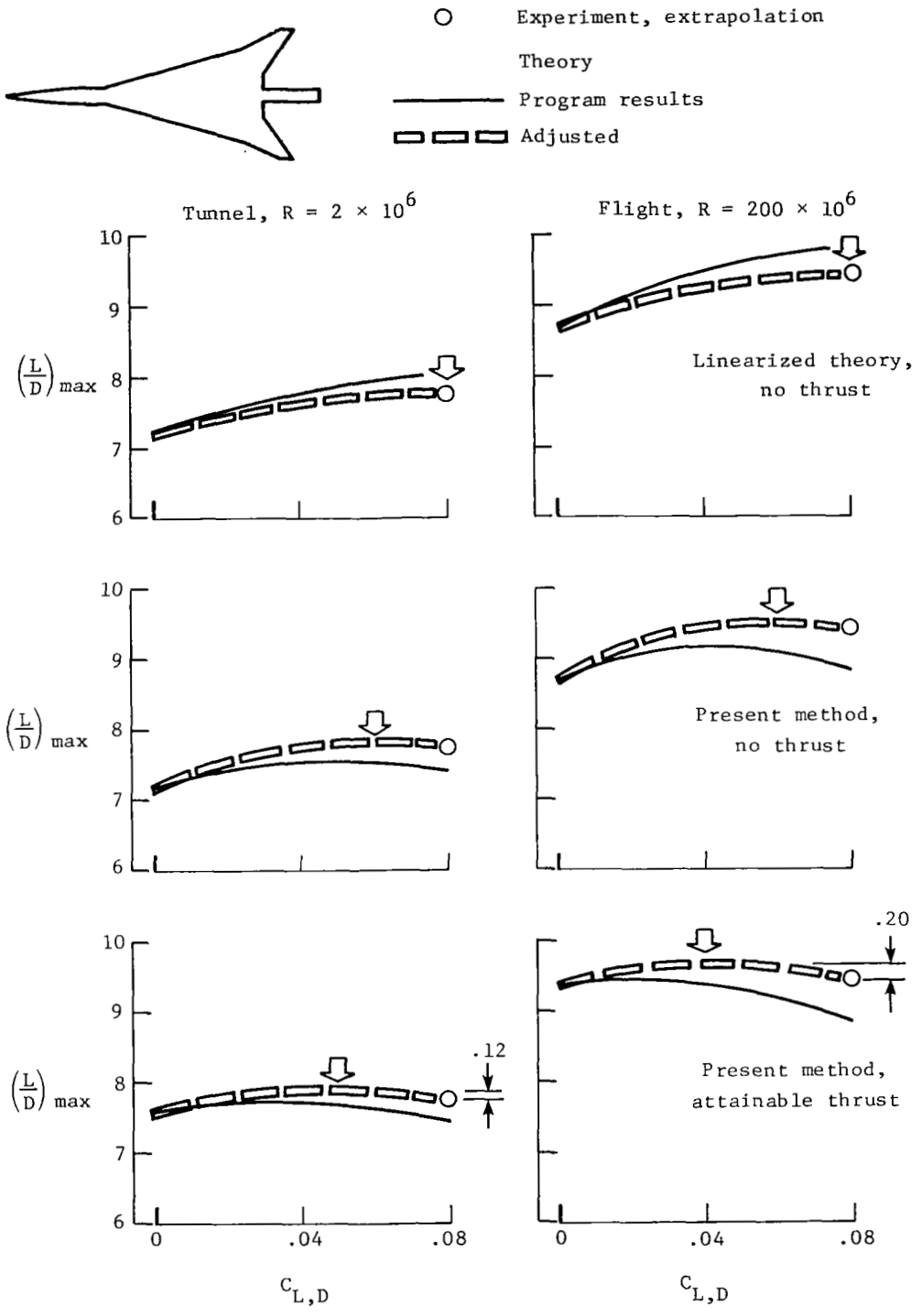

Figure 19.- Estimation of effect of design lift coefficient on performance of a supersonic cruise configuration of high aerodynamic efficiency. $M_\infty = 2.7$.

1. Report No. NASA TP-1718	2. Government Accession No.	3. Recipient's Catalog No.
4. Title and Subtitle ESTIMATION OF WING NONLINEAR AERODYNAMIC CHARACTERISTICS AT SUPERSONIC SPEEDS		5. Report Date November 1980 6. Performing Organization Code
7. Author(s) Harry W. Carlson and Robert J. Mack		8. Performing Organization Report No. L-13589
9. Performing Organization Name and Address NASA Langley Research Center Hampton, VA 23665		10. Work Unit No. 505-31-43-01 11. Contract or Grant No.
12. Sponsoring Agency Name and Address National Aeronautics and Space Administration Washington, DC 20546		13. Type of Report and Period Covered Technical Paper 14. Sponsoring Agency Code

15. Supplementary Notes

16. Abstract

A computational system for estimation of nonlinear aerodynamic characteristics of wings at supersonic speeds has been developed and has been incorporated in a computer program. This corrected linearized-theory method accounts for nonlinearities in the variation of basic pressure loadings with local surface slopes, predicts the degree of attainment of theoretical leading-edge thrust, and provides an estimate of detached leading-edge vortex loadings that result when the theoretical thrust forces are not fully realized.

17. Key Words (Suggested by Author(s))	18. Distribution Statement
Supersonic aerodynamics Aerodynamic nonlinearities Aerodynamic performance prediction Wing pressure distributions Wing forces and moments	Unclassified - Unlimited Subject Category 02

19. Security Classif. (of this report)	20. Security Classif. (of this page)	21. No. of Pages	22. Price
Unclassified	Unclassified	81	A05

For sale by the National Technical Information Service, Springfield, Virginia 22161

NASA-Langley, 1980